Origin of pulsar timing noise: Possible correlations between pulsar spin-down rates and magnetospheric processes.

Jacques Maritz

Submitted in fulfilment of the requirements for the degree

PhD

in the Faculty of Natural and Agricultural Sciences,

Department of Physics,

University of the Free State,

South Africa

Date of submission: March 2017

Supervised by: Prof P.J. Meintjes, Department of Physics

The financial assistance of the South African Square Kilometre Array Project towards this research is hereby acknowledged. Opinions expressed and conclusions arrived at, are those of the author and are not necessarily to be attributed to the NRF.

Abstract

Pulsars are extremely accurate clocks that allow us to explore certain unanswered questions in the fields of exotic compact forms of matter and gravitational wave astrophysics. Pulsars that form part of a timing array can be used to detect stochastic gravitational wave (GWs) backgrounds produced by merging super-massive black holes by searching for systematic correlated delays in the arrival times of the pulses over decades. However, these GW backgrounds produce a small amplitude variation in the timing residuals of a pulsar over decades. Similar to the residual signature produced by GW, timing noise also exhibits a quasi-periodic timing residual signature due to some unidentified variations in the pulsar's spin parameters. This study focused on the analysis of the timing noise phenomena observed in PSR J1326-5859. Several decades of timing and polarization data were analyzed and correlated in an attempt to model the observed timing noise signature. We propose that PSR J1326-5859 is coupled to a fossil disk that torques the star in a quasi stable manner and produces the observed spin-down evolution and polarization state changes.

Keywords: Pulsars, Timing noise, polarization and disks

Opsomming

Pulsare kan aanskou word as baie akkurate kosmiese tydhouers wat fundamentele bydraes lewer in die veld van eksotiese kern materiaal en gravitasie golwe. Pulsare kan as deel van 'n tydhouer-netwerk gebruik word om gravitasie golwe te bestudeer, maar hierdie betrokke sein is baie klein en kan slegs oor dekades waargeneem word. Hierdie bevestiging van gravitasie golwe deur die gebruik van 'n netwerk van pulsare kan beinvloed word deur tydfoute wat nie ingesluit word deur die pulsar-model nie. Die studie het gefokus op meer as twee dekades se chronografie van die reëlmatige pulserende stralingsbron PSR J1326-5859. 'n Korrelasie-studie tussen die chronografie en polarisasie data was uitgevoer in die hoop om die tydfout profiel van PSR J1326-5859 te verduidelik. Ons stel voor dat PSR J1326-5859 'n fossiel-skyf bevat wat op 'n stabiele wyse 'n wringkrag (draaimoment) op die pulsar uitoefen en sodoende die spin-evolusie en polarisasie toestand veranderinge veroorsaak.

Kernwoorde: Pulsare, tydfoute en fossiel skyf

Contents

Chapter 1

Introduction

Radio astronomy focuses on the study of natural objects at radio frequencies using radio telescopes in the form of single dishes or interferometers. Different to optical telescopes, radio telescopes can observe a source during night or day in most weather conditions due to the longer wavelength of natural radio emission. Most of the emission-theory that is associated with radio astronomy is identical to that of optical or higher energy astrophysics, but radio astronomers use different instruments to measure the radio flux and polarization properties of the sources. Many exotic radio sources exist, of which the strongest are nebulae, quasars, radio galaxies and pulsars. The reader can refer to several complete radio astronomy texts, specifically guides written by Kraus [49], Lorimer & Kramer [54], Condon [20] and Camenzind [15] for extensive discussions related to radio astronomy in general and pulsar astronomy in particular, as well as the physical process related to the production of radio emission in astrophysical sources.

The focus of this study is mainly directed towards one of the brightest pulsating radio sources, namely pulsars. Pulsars are rapidly rotating and highly magnetized neutron stars (see Pacini [66]) that can be observed with a large number of telescopes across most of the electromagnetic spectrum (see e.g. Hewish et al. [38] and the references therein for the discovery of pulsars). Associated with rotating pulsars is a plasma-filled magnetosphere that accommodates the acceleration of charges along the magnetic fields to produce different wavelengths of pulsed emission, mostly through the synchrotron process (e.g. see Rybicki & Lightman [81] and Pacini [66]), that can be observed with space-based detectors or telescopes on earth. Pulsars remain mysterious objects due to their peculiar large densities (with core densities of up to $\rho \approx 10^{14}$ g cm^{-3}), spin-periods (from milliseconds to seconds), extreme magnetic fields (up to 10^{15} G for magnetars) and a plethora of mysterious emission mechanisms, see Camenzind [15] and Condon [20].

The conventional picture of pulsars is that they can be considered to be stable clocks

when observed over many rotations, however in the domain of short-term (pulsar rotation time scales) and long-term (several decades) observations, the perfect clock hypothesis breaks down due to dynamical features governing the single pulse evolution both in amplitude, phase and polarization. Also, external mechanisms can gently perturb the pulsar's spin-down process and produce a phenomena called timing noise that could be explained by spin variations induced by the pulsar itself (perhaps dynamics in the interior of the star) or some external mechanism coupled to the star. The reader can refer to Hobbs, Lyne & Kramer [40] for an in-depth study of timing noise observed for several different pulsars.

These timing inaccuracies (or timing noise) in the pulsar timing model automatically generate the most current research fields in pulsar astronomy that are centered around the observation campaigns and modelling of the highly dynamical features seen in many different pulsars. These fields open up the opportunity for new data analysis pipelines and theories that could be attributed to the pulsar itself or due to some influence from external mechanisms. The reader can refer to Cordes & Helfand [21] for the first timing noise observations of pulsars and Dolch et al. [27] for an illustration of an example of latest observational campaigns undertaken in the field of pulsar timing dynamics.

Since the origin of the observed radio emission from the pulsar's magnetosphere and the phenomena of timing noise are not well understood, the analysis of timing data needs to be performed in a model-independent manner to ultimately extract an astrophysical model from the results. The analysis methodology presented in this study was based on the field of machine learning, particularly the probabilistic regression method called the Gaussian process. The Gaussian process regression method is widely used in the pulsar timing community, particularly towards problems of regression and the classification of new data (see Brook et al. [10] and Brook et al. [11] for unique applications of this method in the field of pulsar astronomy). Gaussian process regression is widely used in the regression of time series data with the specific requirement of inferring a continuous theoretical description of the time-series data that can be differentiated (see Seikel, Clarkson & Smith [83]). The Gaussian process regression methodology ensures the best unbiased supervised regression learning for time series data and can be used for data of uneven cadence.

We aim to test the theory based upon the fact that pulsar may be associated with a low mass disk which may explain the main spin variations observed in the pulsar candidate PSR J1326-5859, since now other current models aimed to explain the observed variations (such as the binary companion or GW backgrounds). Using machine learning techniques to investigate the spin-down evolution and correlation

thereof with magnetospheric processes of the prominent timing noise candidate PSR J1326-5859, a disk model was inferred of which the inner disk radius oscillates between modes and ultimately produces the spin-down evolution of PSR J1326-5859 and inherently the timing noise signature. An unique polarization study for the search of any changes in the polarization state (or polarization vector) of the pulsed radio emission due to the presence of a disk was developed and the results were investigated for consequences of such changes in the context of pulsar magnetospheric models and spin-down behavior, this is similar to the orthogonal polarization searches conducted by Osłowski et al. [63], but this study focused on the other mechanisms that induce polarization swings such as reflected emission. The polarization swing searches and inferred disk models presented in this work can serve as novelties that can be of importance for the future meerKAT pulsar observational campaigns, that could attempt to find fossil disks associated with pulsars through the process of high accuracy timing and timing noise identification of pulsars, combined with multi-wavelength searches for signatures (e.g. IR excess) of fossil disks around isolated pulsars.

In this study I propose that the origin of timing noise could possibly be connected to the existence of stable pulsar-disk systems that through the dynamics of the pulsar magnetosphere-disc coupling could induce the observed variations in the timing residuals of certain pulsars over extended time periods. It will be difficult to observe these pulsar-disk systems directly at large distances, however through the process of long-term timing and the recording of calibrated polarization data, these systems could offer an unique window into the spin-evolution of pulsars and the magnetospheric astrophysics that accompanies the pulsed emission of a pulsar or, possibly, a population of pulsars. Due to the difficulties of observing these systems directly and the implications of finding more such systems to test the evolutionary theory of pulsars, I ultimately propose an indirect observational method that is based on a combination of high precision timing of pulsars, machine learning (specifically regression methods) and the analysis of carefully calibrated polarization data. The long-term list of high-precision timing residuals can be used to infer the most-probable spin-down evolution of the particular pulsar using machine learning techniques (see e.g. Brook et al. [11] and Brook et al. [10] for applications of regression in pulsar astronomy) given that the residuals indicate some form of timing noise (typically quasi-periodic). The pulse profiles can be used to search for extreme signs of radio emission quenching that could possibly indicate the interaction of a disk with the pulsar's magnetosphere via the process of accretion and will also reflect changes in the pulse shape.

The calibrated polarization data can be used to search for swings in the polar-

ization vector (using the Poincare sphere), different to the phenomena of possible orthogonal polarization modes (OPM, see Osłowski et al. [63]) (which is a shift of 90 degrees in the polarization vector due to overpowering effect of one of the competing polarization modes as the emission propagates through a denser medium) in the pulsar's magnetosphere, one can specifically search for swings in the polarization vector of 180 degrees, which if the pulsar does not exhibit an inter-pulse, may indicate reflected emission of the obscured pulse from a denser plasma, possibly a disk. To overcome the difficulty of observing known pulsars long enough to form the needed timing noise signature (which is needed for the optimized machine learning processes), one can use archival timing data from several telescopes to form the overall timing noise signature, this could then be supplemented with high precision-calibrated polarization data of which the polarization state (checked by evaluating the polarization vector of the particular observation) can be tracked for the entire phase-resolved pulse profile to search for indications of abrupt polarization swings which may indicate reflected emission. The proposed method is of particular interest for modern pulsar astronomy programs (such as MeerKAT and its pulsar program MeerTIME) since it can benefit from the increased data rate (e.g. ability to obtain more high accuracy times of arrival (TOA), residuals, profiles, polarization data and multi-frequency observations) and the capability of extreme real-time processing of the data by using machine learning techniques. The main candidate of interest in this study is the normal isolated pulsar PSR J1326-5859 that could be used as a primary candidate for future meerKAT campaigns due to its interesting spin-down evolution and polarization properties. After the investigating PSR J1326-5859 as the primary candidate in this study, I propose PSR J1326-5859 to be a pulsar that is possibly associated with a fossil disk.

This thesis is structured as follows: Chapter 2 introduces the reader to some basic principles in the fields of radio and pulsar astronomy including some terminology and emission principles that are often used in the field of radio astronomy, Chapter 3 focuses on the process of pulsar timing in the radio and gamma-ray regime (since pulsars emit over the entire EM spectra, see Condon [20]) that also include a synergy study between radio and gamma-ray emission, Chapter 4 introduces the reader to the phenomena of timing noise and the analysis thereof, with particular emphasis on machine learning techniques that are used for the regression of timing noise signatures, Chapter 5 discusses the analysis of the timing noise phenomena observed in PSR J1326-5859 with particular focus on the mining process of the timing and polarization data over long time spans, Chapter 6 investigates a possible pulsar-disk model that could explain the structure and amplitude of the timing noise observed in PSR J1326-5859 and Chapter 7 concludes the study. A series of published conference proceedings (see the Proceedings of Science, www.pos.sissa.it with ISSN 1824-8039

and The Proceedings of the Annual Conference of the South African Institute of Physics with ISBN: 978-0-620-70714-5) that were accepted during my PhD, was included as an appendix that informally follows the outline of the thesis.

Chapter 2

Introduction to radio and pulsar astronomy

2.1 Basic principles of radio astronomy

2.1.1 Modern day radio astronomy

Karl Jansky first observed radio noise from our Milky Way in 1933 (Jansky [44]). As an engineer of Bell Telephone Laboratories, Jansky tried to understand the interference generated on the transatlantic voice transmissions and quickly realized that the radio noise came from outside our own planet. This strange signal was recorded and he noted that the signal peaked roughly every 24 hours. He concluded that this occurred when his antenna (see Fig.2.1) was pointing towards the galactic center of the Milky Way. This detection was not due to the Sun, but due to emission produced by electrons moving in strong magnetic fields associated with a vast collection of objects in the area of Sagittarius A (the center of our Milky Way galaxy). In 1937 Grote Reber constructed a parabolic radio telescope in his backyard and performed one of the first radio surveys of the sky (carefully mapping out radio intensity contours of the radio sky). This marked the beginning of a new era in astronomy and engineering with vast possibilities and new observational opportunities.

Following Reber's homemade telescope nearly 75 years ago, our need for higher frequency observations and more sensitive radio telescopes led to modern day radio telescopes, including single radio dishes such as: the 1000-ft Arecibo telescope in Puerto Rico ($\lambda = 4$cm), the Green Bank Telescope (GBT) of the National Radio Astronomy Observatory ($\nu = 2$cm), the 64m Parkes radio telescope in Australia ($\lambda = 1 - 50$cm), the Low Frequency Array for Radio astronomy (LOFAR, $\lambda = 30 - 1.3$m), see Fig. 2.2 (a-e).

We are now living in the era of large radio telescope arrays that allow the observer to

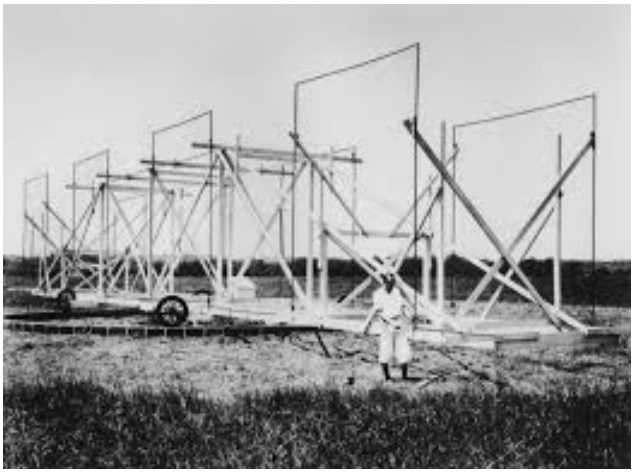

Fig. 2.1: Karl Jansky's mounted radio antenna, designed to observe radio waves with a frequency of 20.5 MHz. Adopted from www.nrao.edu).

effectively increase the effective collecting area and the sensitivity of the instrument specifically benefiting the radio imaging field, enabling large surveys and wide band point source observations. One such array is the Square Kilometer Array (SKA), which will be the state of the art of radio astronomy, see Fig. 2.2 for an artist impression. This telescope, with sensitivity more than 100 times that of Parkes (see Fig.2.3), will have an angular resolution of less than 0.1 arcseconds and a wide-band observational frequency range of 70 MHz to 10 GHz (see e.g. Lorimer & Kramer [54]). The telescope is expected to detect all of the more than 20 000 active radio pulsars in our Galaxy and possibly monitor them regularly using highly accurate timing procedures. The ultimate design of this telescope is based on several key science projects that form the core objectives of the SKA and the radio community (see www.ska.ac.za).

2.1.2 Jansky: the unit of radio astronomy

To introduce the reader to the basic parameters that can be measured in radio astronomy (which also serves as an introduction to the next chapter on radiometer principles), we refer the reader to Fig.2.4 that illustrates the basic concept of measurement through the utilization of the main radiation pattern that is formed when observing a source with a radio dish at a distance R. When observing a part in the sky that spans a fraction of the beam solid angle, $d\Omega$, which causes a current to flow in the receiver (illustrated as a simple resistor-receiver in this case) and ultimately generates a fictitious antenna temperature (T_R) that can be used to calculate the real radio flux that had been received from the source. Here follows some basic concepts related to the detection of cosmic radiation (see e.g. Kraus [49] and Rybicki & Lightman [81])

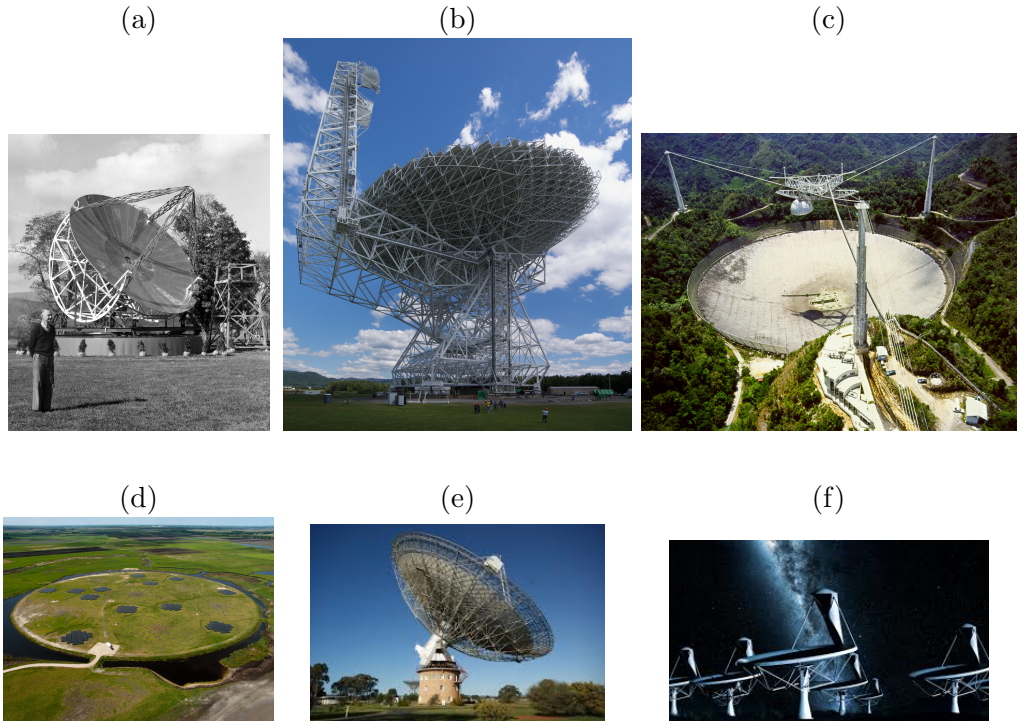

Fig. 2.2: Collection of primitive and modern radio telescopes: (a) First Reber parabolic dish, (b) GBT of NRAO (National Radio Astronomy Observatory), (c) Arecibo in Puerto Rico, (d) LOFAR in the Netherlands, (e) Parkes in Australia and (f) is the SKA of which the core will be built in South Africa.

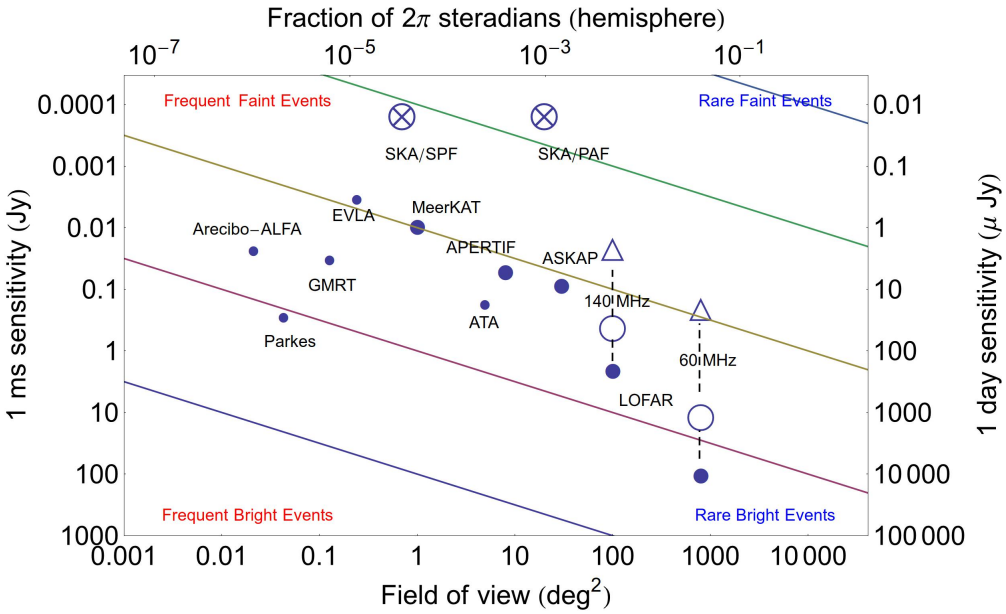

Fig. 2.3: Sensitivity curves of modern radio telescopes and interferometers clearly showing the advancement of the SKA project. Adopted from Fender [28].

Antenna beam solid angle is the most basic system parameter that needs to be known for several different radio experiments from single dish observations to complex antenna synthesis campaigns. If we assume that our antenna has a single main lobe then the antenna beam solid angle (Ω_{beam}) will theoretically be where all the radiated power would flow with maximum radiation intensity (focusing effect of the radiation). Pictorially this can be illustrated in Fig.2.4, but we can also visualize the beam solid angle mathematically,

$$\Omega_{\text{beam}} = \int_0^{2\pi} \int_0^{\pi} P(\theta, \phi) \sin\theta d\theta d\phi, \tag{2.1}$$

where (θ, ϕ) are spherical coordinates and $P(\theta, \phi)$ represents the antenna power pattern which varies in different directions. In theory we approximate the pattern to a single main lobe in the direction of maximum detection (typically orthogonal to the reflector). The solid angle for a sphere is

$$\Omega_{\text{sphere}} = 4\pi(\text{sr}) \tag{2.2}$$

For practical purposes we can also relate the main beam solid angle to the antenna half-power beam-width, which is

$$\Omega_{\text{beam}} \approx \theta_{HP}\phi_{HP}, \tag{2.3}$$

where θ_{HP} is the half-power beam-width and ϕ_{HP} is the half-power beam-width in the ϕ-direction. The beam solid angle is used to compare beam-widths between several telescopes and the reader is notified that radio astronomers approximate the real antenna patterns with fictitious beam patterns when determining the beam solid angle and it is assumed that the antenna receives radiation in a certain direction (e.g. observing a point source).

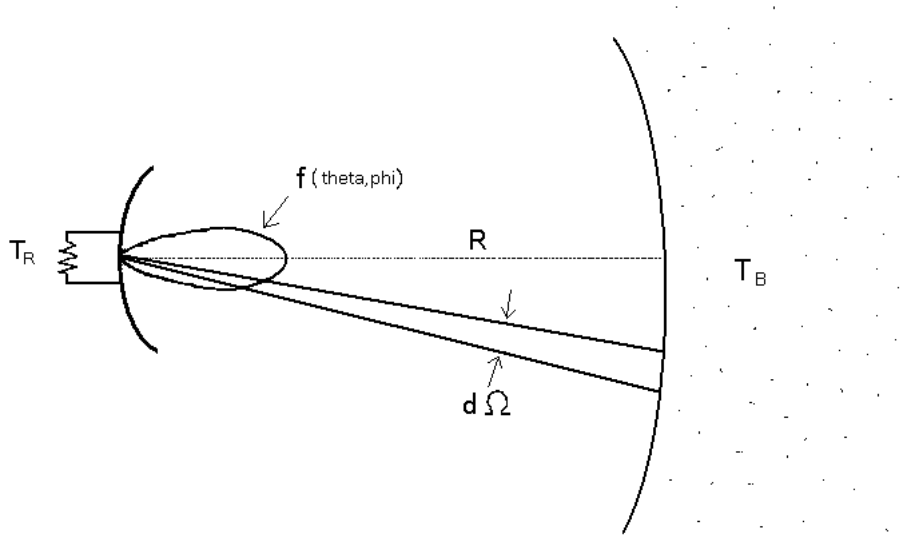

Fig. 2.4: Basic observing geometry and angles associated with radio observations. Here $d\Omega$, R, T_B, T_R are the solid angle of the sources, distance to source, temperature of the source in Kelvin and the temperature of the receiver (resistor in this case) in Kelvin, respectively. Adopted from the tutorial manuals of the Rockwell International's Collins Air Transport Division.

In radio astronomy the unit of Jansky is used ($10^{-26}\text{Wm}^{-2}\text{Hz}^{-1}$) for the flux density observed from a particular radio source. It is assumed that the source emits radiation with wavelength λ and corresponding frequency ν. For a detector with an area

A, the radio flux measured with this detector will be the rate at which the energy crosses the effective area $A_{\rm eff}$. The power collected by the dish is proportional to the effective area of the dish ($A_{\rm eff}$) and the flux density of the electromagnetic waves falling perpendicular on the antenna

The above mentioned power can be scaled according to the directive gain (due to presence of side lobes), which is given by the ratio of the maximum power and the average power, i.e. the directive gain along the main lobe is unity and from there scales accordingly to whether the source presides in the main lobe or in one the side lobes. Concepts of the radiation field associated with the source will now be presented following discussions covered in Kraus [49] and Rybicki & Lightman [81].

If the collecting surface of the antenna is perpendicular to the direction of propagation of the electromagnetic field, the flux will be:

$$S = \frac{dE}{dtA}, \tag{2.4}$$

or integrated over the total bandwidth of the observation (summation of all the frequency bins),

$$S = \int S_\nu d\nu. \tag{2.5}$$

The effective aperture area $A_{\rm eff}$ is related to the wavelength and beam solid angle

$$\lambda^2 = A_{\rm eff}\Omega_{\rm beam}. \tag{2.6}$$

The radio telescope focuses the incoming radiation onto a primary beam with an effective solid angle of $\Omega_{\rm beam}$. The gain in the primary beam (assuming that all side lobes are ignored) can then be expressed as:

$$G = \frac{4\pi}{\Omega_{\text{beam}}}. \tag{2.7}$$

The gain of the telescope can also be defined as the ratio between solid angle subtended by a sphere and the solid angle of the antenna beam. Assuming a symmetrical reflector having an area of d^2 then the primary beam has width $W_{\text{beam}} \approx \frac{\lambda}{d}$ and solid angle $\frac{\lambda^2}{d^2}$. By using these relations the telescope gain becomes:

$$G = \frac{4\pi A_{\text{eff}}}{\lambda^2}. \tag{2.8}$$

Realistically, radiating sources have finite angular extent (e.g. the Sun) and the observed flux is characterized per solid angle and frequency, this is known as specific intensity:

$$I_\nu = \frac{dP}{dA d\nu d\Omega}, \tag{2.9}$$

where dP is the power received by a telescope with projected area along the angle θ in the solid angle $d\Omega$ within some frequency interval dν, see Fig.2.5. The brightness is independent of distance and the same at both source and detector. If the source is resolved or unresolved then the flux density is measured and not spectral brightness, which is an inherent attribute of the source (see Condon [20] for an complete analysis of these properties).

Assuming a radio source that is emitting radiation with a specific frequency, the observed total flux becomes ($I_\nu = B_\nu$):

$$S = \int\int B_\nu(\theta, \phi) \cos\theta d\Omega d\nu. \tag{2.10}$$

The observed flux per frequency bin (S_ν) is called the flux density and has units of

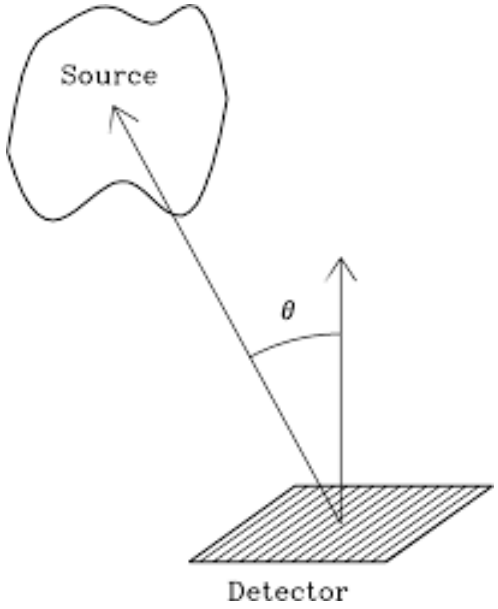

Fig. 2.5: Source that is observed at an angle θ. Adopted from Condon [20].

Jansky's:

$$1\text{Jy} = 10^{-26}\text{Wm}^{-2}\text{Hz}^{-1}. \tag{2.11}$$

The antenna beam-efficiency (or stray factor) is simply the ratio between the solid angle that is subtended by the main beam and that of the side lobes (which varies for different types of reflectors). The spectral luminosity (L_ν) is the total power received within a narrow frequency bin,

$$L_\nu = 4\pi d^2 S_\nu, \tag{2.12}$$

where S_ν represents the measured flux density of an isotropic emitter at a distance d from the observer.

We conclude this subsection with a well-known illustrative example (see page 11 of Condon [20]), consider a radio observation of a black body with a temperature of $T \approx 5800$ K, at a frequency of $\nu \approx 1$ GHz, size of the Sun and at a distance of 1 parsec. Thus, for the Sun, assuming a black body spectrum, the brightness will be

(e.g. Rybicki & Lightman [81])

$$B_\nu = \frac{2kT\nu^2}{c^2} \approx 1.78 \times 10^{-15} \mathrm{erg\,cm^{-2}}, \tag{2.13}$$

for which the solid angle of the sun depends on the distance, i.e. $\Omega \approx 1.71 \times 10^{-15}$ sr for d = 1 pc. Finally using the above stated relations the flux density of the sun can be inferred when observed at a frequency of 1 GHz as,

$$S_\nu = B_\nu \Omega \approx 3 \times 10^{-30} \mathrm{erg\,s^{-1} cm^{-2} Hz^{-1}} \approx 0.3 \mu \mathrm{Jy}. \tag{2.14}$$

The brightness temperature is the temperature of a Blackbody (bb) emitter which emits the same flux at frequency ν as an astrophysical source in the Rayleigh-Jeans limit, i.e. (see Rybicki & Lightman [81]), and is of particular use to radio astronomers as will be illustrated in the following sections.

$$T_b = \frac{c^2 B_\nu}{2k\nu^2} \tag{2.15}$$

This is a very handy tool to determine whether the measured flux of an astronomical source is emitted via thermal processes, or in the case where the brightness temperature is very high, by non-thermal processes like synchrotron radiation (emission from gyrating electrons) associated with highly energetic sources.

2.1.3 Radiometer principles

Radio frequencies range from 3 kHz to 300 GHz (see e.g. Burke [14]). A telescope samples the signal at a specific frequency (or radio frequency, RF) depending on the necessary scientific outcomes of the observations and the particular receiver used. Associated with the radio telescope is a finite bandwidth (or a band containing several frequencies, B) which is centered around a frequency f_{RF}.

The incoming signal is gathered by the parabolic dish and focused into the primary beam that is detected/gathered by the feed horn (conveyor mechanism of radio

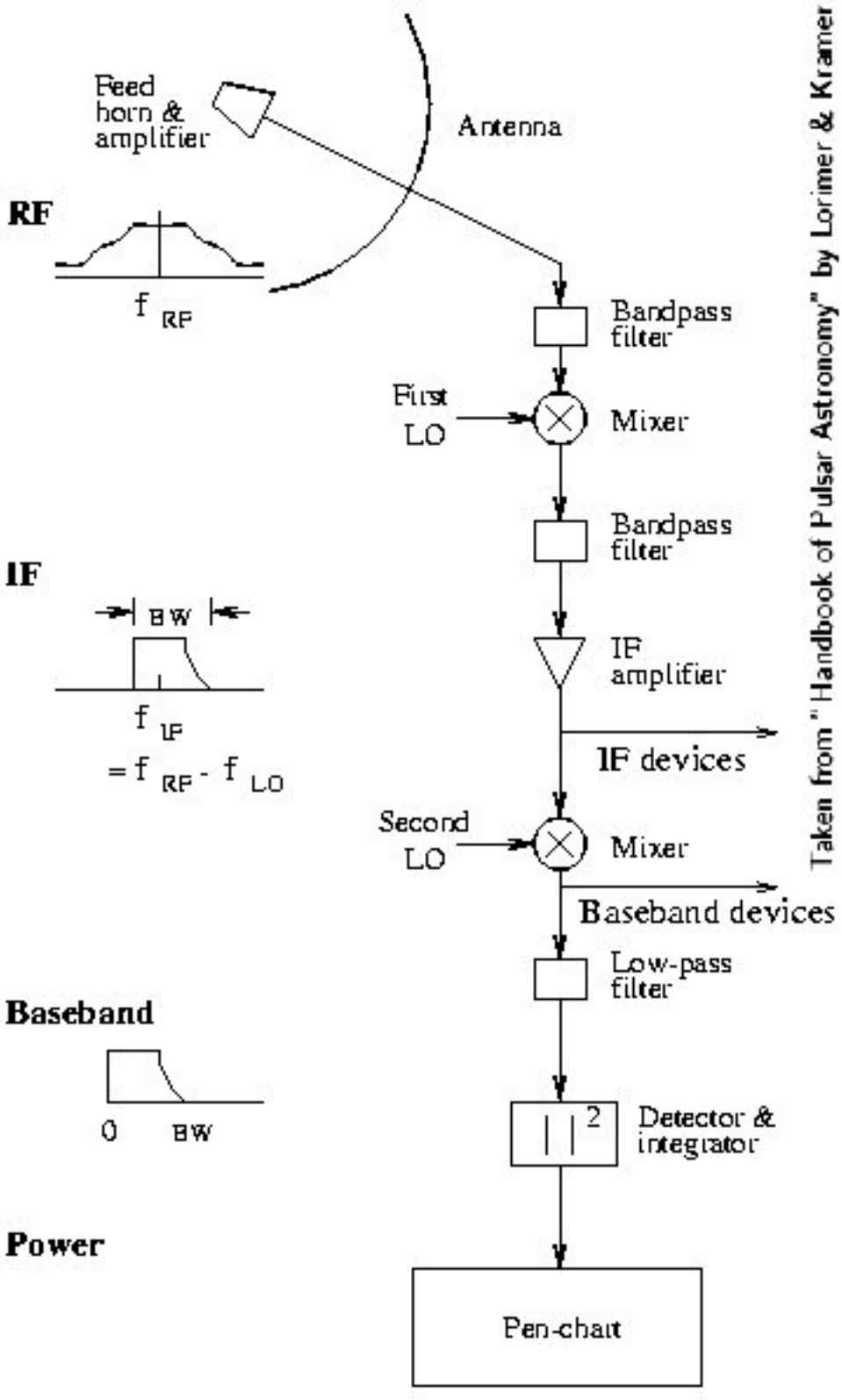

Fig. 2.6: Basic components of a idealistic radiometer and a representation of signal path , adopted from Lorimer & Kramer [54].

waves between the source and the receiver), see Fig. 2.6. Radio waves observed from emitting sources are generally weak and the front-end (receiver part of the radio telescope) also amplifies the signal. When amplifying the weak signal, it becomes crucial not to add extra noise to the signal. This simple requirement became the pivot point of state of the art radio telescope design.

The amplified signal is passed through a band-pass filter that eliminates any harmonics that are not associated with the band of frequencies. The RF signal is converted to a lower intermediate frequency (IF) that can be transmitted to the processing part of the signal path (which is generally not on the telescope itself) efficiently and without cable losses. This operation is performed by mixing the RF signal with a local oscillator (LO) that produces a signal (IF) with a frequency equal to the difference of the frequencies of the two original signals ($f_{IF} = f_{RF} - f_{LO}$). From this point the RF and IF signals can be sourced to certain devices if needed, otherwise, the signal is send to the detector where it is integrated and stored as observed signal power that can utilized by the radio astronomer.

It is true that in radio astronomy the observed signal can be mathematically manipulated as desired (part of signal processing). This is either done by hardware or digital filters (Jansky [44]). In the absence of a strong radio source the antenna still picks up a superposition of white noise (Gaussian random noise), caused by thermal noise and other electronic noise generated by the receiver of the telescope itself. This noise can be described in terms of temperature by using the following thought experiment: assume that the antenna primary beam is filled by emission produced by a black body with temperature T. After reception the signal passes through a bandpass filter with bandwidth (B). Let the signal terminate into a load resistor (i.e. a resistor that becomes the same temperature as the antenna receiver, see Fig.2.4) with matching impedance to insure the conservation of signal power. Since the beam is completely filled the match load needs to reach the same temperature T and the thermal noise power generated in the resistor (or antenna receiver) becomes:

$$P = P_\nu d\nu = kT_A \Delta\nu, \tag{2.16}$$

where the P_ν represents the power density (erg s^{-1} Hz^{-1}). This power is also known as Johnson Noise and represents the power in the resistor due to the electrons in the resistor that undergo thermal motion and operates in the Raleigh-Jeans limit. The power density that is delivered to an output of an antenna that is observing a

source of temperature T is (see e.g. Burke [14]):

$$P_\nu d\nu = 0.5 \int B_\nu A_{\rm eff} d\Omega d\nu, \tag{2.17}$$

where the factor 0.5 is for one polarization channel only. Finally, the antenna temperature becomes

$$T_A = \frac{P}{k\Delta\nu}, \tag{2.18}$$

or as a function of the observed flux of the source,

$$T_A = \frac{A_{\rm eff} S}{2k}, \tag{2.19}$$

where the factor two takes into account the factor of one-half lost in the total incident power, since the antenna can only respond to one polarization. Also, $A_{\rm eff}$ defines the effective area of the telescope (which can be a parabolic reflector). Effectively we have constructed a fictitious quantity called brightness temperature with units of Kelvins. Radio astronomers conveniently use this unit since 1K of antenna temperature corresponds to a power density of

$$P_\nu = kT_A = 1.38 \times 10^{-23} \text{W Hz}^{-1}. \tag{2.20}$$

The system noise (generated by the receiver's electronics), the radio flux from an astronomical source and any noise calibration source can now be represented by an fictitious temperature, these temperatures are $T_{\rm system}$, $T_{\rm source}$ and $T_{\rm cal}$. If the antenna is pointing to a empty part of the sky (with the average$T_{\rm sky} \approx 3K$), then the antenna temperature will be:

$$T_{\mathrm{A}} \approx T_{\mathrm{system}} + T_{\mathrm{sky}}. \tag{2.21}$$

There exist an obvious problem; when the telescope is pointing towards a source with temperature T_{source}, the antenna temperature will never be $T_{\mathrm{A}} = T_{\mathrm{source}}$. Luckily, there exist several methods of calibration to address this problem. By injecting the system with a known noise (T_{cal}) the antenna temperature (T_{A}) can be decomposed and the brightness temperature of the source can be determined by switching on the calibration noise source.

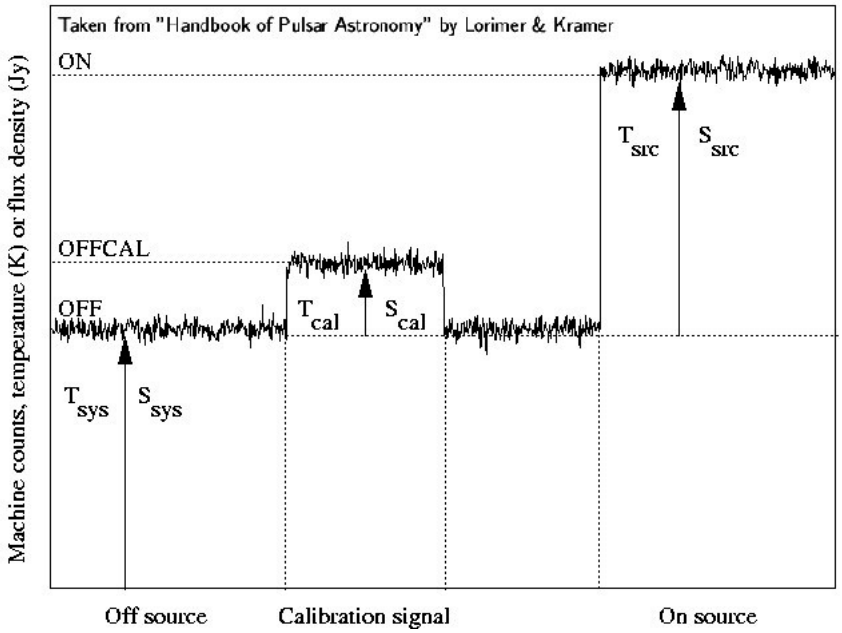

Fig. 2.7: Calibration process of a radiometer using a known calibration source. The calibration source can be a hot/cold load or a noise resistor (see e.g. Lorimer & Kramer [54]).

As an example, an amateur radio telescope that composes of a Low Noise Block amplifier (LNB) (front-end, $T_{\mathrm{LNB}} \approx 50K$) and a receiver (back-end). If this telescope is pointing to the ground or the wall ($T_{\mathrm{ground}} \approx 300K$) the antenna temperature becomes:

$$T_{\mathrm{A}} \approx T_{\mathrm{system}} + T_{\mathrm{ground}} \approx 50K + 300K. \tag{2.22}$$

This ever-present telescope system noise ($T_{\rm system}$) produces an uncertainty in the measurement of the antenna temperature. If the radiometer has a bandwidth (B) and the signal is sampled for a total time τ, the fluctuations in the receiver system scales with the square root of the number of samples and follows Gaussian Probability:

$$\Delta T_{system} = \frac{T_{system}}{\sqrt{n_p B \tau}}, \tag{2.23}$$

where n_p represents the number of observed polarizations. This generates an uncertainty in the observed flux, also known as the flux sensitivity, which is important when deciding what type of radio sources to observe with the telescope:

$$\Delta S = \frac{2k\Delta T_{sys}}{A_{\rm eff}\sqrt{n_p B \tau}}. \tag{2.24}$$

The latter form is part of the fundamental radiometer equation and is used in limit calculations of the radio telescope (see e.g. Burke [14] and Lorimer & Kramer [54]). The radio astronomer engages the above mentioned calculations before attempting to observe a radio source (observational feasibility study).

2.1.4 Radio wave polarization

Polarization is an inherent property of radiation fields that can be introduced by scattering (e.g. Thompson scattering), reflection of a surface or radiation produced by electrons radiating in a magnetic field, i.e. synchrotron radiation. The polarization is determined by the orientation of the electric field vector of the radiation (e.g. Rybicki & Lightman [81]). For synchrotron radiation the electric field vector will always be orientated perpendicular (e.g. Longair [53]) with respect to large scale magnetic fields where the radiation is produced (see Fig.2.8), therefore it can be used as a diagnostic tool to constrain the properties of the synchrotron emitting astrophysical source. However polarization can be influenced by the interstellar medium (ISM) by introducing polarization vector swings or by inducing de-polarization. An introduction will now follow regarding polarization studies and the mechanisms that can influence the polarization state of the observed radio emission from a source.

A radio wave (or electromagnetic wave) has both amplitude and phase and can be

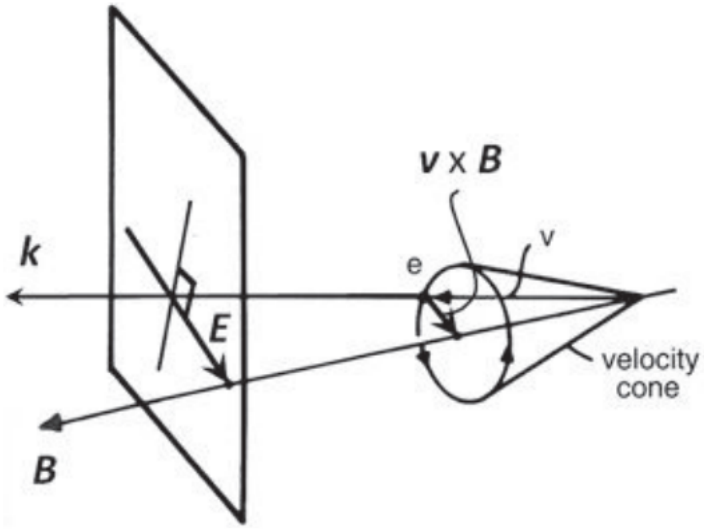

Fig. 2.8: The velocity cone of an ultra-relativistic electron and the polarization associated with it. Adopted from Longair [53].

measured with radio receivers. This wave is governed by the wave equation in free space. For the electric field this is:

$$\nabla^2 \boldsymbol{\mathcal{E}} = \frac{1}{c^2} \frac{\partial^2 \boldsymbol{\mathcal{E}}}{\partial t^2}. \tag{2.25}$$

The magnetic field ($\boldsymbol{\mathcal{B}}$) equation is governed by a similar equation, together with the condition that the cross product ($\boldsymbol{\mathcal{E}} \times \boldsymbol{\mathcal{B}}$) determines the propagation direction of the wave. These equations have unique solutions when we use the assumption that the observer is sufficiently far from the source (we assume that plane wave scenario is valid), see Fig.2.9. This assumption leads to an expression of the electric field ($\boldsymbol{\mathcal{E}}$) that is elegant and manageable. Following along the lines of van Straten et al. [91], consider a monochromatic electromagnetic wave with frequency ω, propagating towards the observer and represented by the electric field that is orthogonal to the direction of propagation (Hecht & Zaj [37]):

$$\boldsymbol{\mathcal{E}}(t) = \begin{pmatrix} \mathcal{E}_0 \\ \mathcal{E}_1 \end{pmatrix} = \begin{pmatrix} a_0(t) \exp i[\phi_0(t) + \omega t] \\ a_1(t) \exp i[\phi_1(t) + \omega t] \end{pmatrix} \tag{2.26}$$

In vector notation the polarization of the radio wave can be described as a 2×2

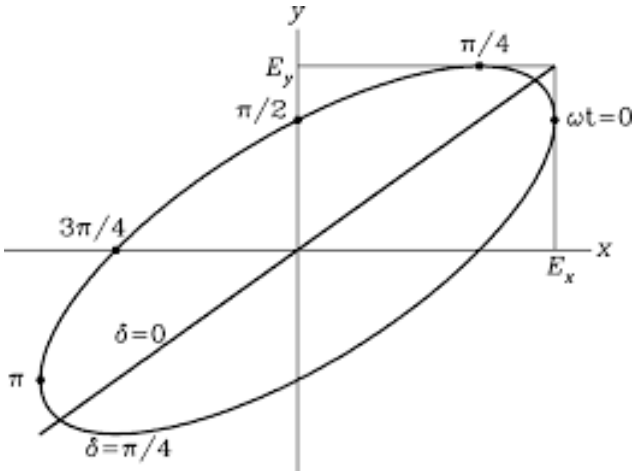

Fig. 2.9: Illustration of the electric field vector of a monochromatic EM wave traveling in the z-direction (out of the page) described by the vector notation formulated in the beginning of this subsection. Adopted from Condon [20].

coherency (polarization) matrix that contains all the measurable information about the state of polarization. It may be expressed as a linear combination of the Hermitian basis matrices (a matrix is Hermitian if the matrix is self-adjoint), this is:

$$\boldsymbol{\rho} = 0.5 \sum_{i=0}^{i=3} S_i \boldsymbol{\sigma}_i = \frac{S_0 \boldsymbol{\sigma_0} + \mathbf{S}.\boldsymbol{\sigma}}{2}, \tag{2.27}$$

where S_0 is the total intensity, $\mathbf{S} = (S_1, S_2, S_3)$ is the Stokes polarization vector containing the Stokes parameters, $\boldsymbol{\sigma} = (\sigma_1, \sigma_2, \sigma_3)$ is the three Pauli matrices (derived from Quantum mechanics) and $\boldsymbol{\sigma}_0$ is the 2×2 identity matrix. Expanding and averaging $\boldsymbol{\rho}$ produces:

$$\boldsymbol{\rho} = \begin{pmatrix} \langle \mathcal{E}_0 \mathcal{E}_0^* \rangle & \langle \mathcal{E}_0 \mathcal{E}_1^* \rangle \\ \langle \mathcal{E}_1 \mathcal{E}_0^* \rangle & \langle \mathcal{E}_1 \mathcal{E}_1^* \rangle \end{pmatrix}. \tag{2.28}$$

Along the lines of Condon [20], when the radiation is linearly polarized, the orthogonal components of wave are in phase with constant ratio of amplitudes producing a constant direction of the electric vector. When the wave is circularly polarized, the orthogonal components of the wave is 90 degrees out of phase and the electric vector traces a circle. Linearly polarized waves can be decomposed into two opposite circular waves. A key tool for this study is the use of the Poincare sphere of which

the spherical surface is occupied by the polarized states. The poles of the sphere represent left and right hand circular polarized states. The equator represents the linearly polarized states, see Wang et al. [94].

The Stokes parameters can now be calculated by expanding the series (see van Straten et al. [91]):

$$S_k = \mathrm{tr}(\boldsymbol{\sigma}_k \boldsymbol{\rho}). \tag{2.29}$$

Which leads to the Stokes parameters:

$$\begin{aligned} I &= \langle \mathcal{E}_0^2 \rangle + \langle \mathcal{E}_1^2 \rangle && (2.30)\\ Q &= \langle \mathcal{E}_0^2 \rangle - \langle \mathcal{E}_1^2 \rangle && (2.31)\\ U &= \langle 2\mathrm{Re}(\mathcal{E}_0 \mathcal{E}_1^*) \rangle && (2.32)\\ V &= \langle 2\mathrm{Im}(\mathcal{E}_0 \mathcal{E}_1^*) \rangle. && (2.33) \end{aligned}$$

These parameters can be expressed in a compact way, namely the Stokes vector:

$$\boldsymbol{S} = \begin{pmatrix} I \\ Q \\ U \\ V \end{pmatrix}. \tag{2.34}$$

This vector can have several forms for different states of polarization of light, some of which are:

Linearly polarized (horizontal):

$$\boldsymbol{S} = \begin{pmatrix} 1 \\ 1 \\ 0 \\ 0 \end{pmatrix}. \tag{2.35}$$

Linearly polarized (45 degrees):

$$\boldsymbol{S} = \begin{pmatrix} 1 \\ 0 \\ 1 \\ 0 \end{pmatrix}. \tag{2.36}$$

Right-hand circularly polarized:

$$\boldsymbol{S} = \begin{pmatrix} 1 \\ 0 \\ 0 \\ 1 \end{pmatrix}. \tag{2.37}$$

Left-hand circular polarized :

$$\boldsymbol{S} = \begin{pmatrix} 1 \\ 0 \\ 0 \\ -1 \end{pmatrix}. \tag{2.38}$$

Unpolarized:

$$\boldsymbol{S} = \begin{pmatrix} 1 \\ 0 \\ 0 \\ 0 \end{pmatrix}. \tag{2.39}$$

For a linear feed the total polarized intensity is defined as:

$$P = \sqrt{U^2 + Q^2}, \tag{2.40}$$

with an intrinsic position angle in the sky

$$\Phi = 0.5 \arctan \frac{U}{Q}. \tag{2.41}$$

The feeds are non-ideal and polarization leakages do occur, hence, calibration is typically needed since the amplification process alters the recorded parameters. Practically, the output of the feeds produce the $\mathcal{E}_x$ and $\mathcal{E}_y$ and the total intensity including the fraction of linear/circular polarization can be measured. The reader is notified about the importance of polarization calibration of the data, since the feed can have polarization leakages that produce impurities in the true values of the Stokes parameters. The full polarization calibration process will be discussed in the upcoming sections.

As mentioned earlier, the propagating radio wave or pulse can be altered by the ISM, for example by the presence of ambient magnetic fields between the observer and the source. It is known (e.g. Kraus [49]) that the presence of large scale magnetic fields along the direction of propagation of the radio wave introduces a different index of refraction for the left and right circular polarization states, resulting in a phase rotation of the net electric field vector of traveling wave (e.g. Condon [20]). The phase lag induced by this effect scales as $\Delta\Phi = -kd$ where d is the distance to the source and $k = \frac{2\pi}{\lambda}$ is the wave number. The total rotation of the wave-front in the sky due to this difference in the propagation velocities of the left and right circular propagating waves, is

$$\Phi = \frac{1}{2} \int_0^d (k_R - k_L) dl. \tag{2.42}$$

Assuming a plasma and cyclotron frequency of ω_p and ω_c, the difference in the wave numbers for right and left polarization is given by,

$$\Delta k = k_R - k_L \approx \frac{\omega_p^2 \omega_c}{\omega^2 c}, \tag{2.43}$$

thus the total rotation of the wave front will be

$$\Delta\Phi \approx \frac{1}{2}(k_R - k_L)\delta z. \tag{2.44}$$

The corresponding phase shift in the polarization position angle swing is:

$$\Delta\Phi_{\mathrm{PPA}} = \lambda^2 \mathrm{RM}, \tag{2.45}$$

where RM represents the rotation measure that is a function of the electron density and the parallel component of magnetic field between the telescope and the source,

$$\mathrm{RM} = \frac{e^3}{2\pi m_e c^4} \int_0^d n_e B_{||} dl. \tag{2.46}$$

Thus, knowing both the rotation measure (measure of polarization swing induced by ISM) and the dispersion measure (measure of electron density between telescope and the observer) one can calculate the average magnetic field strength along the line of sight of the observer (Lorimer & Kramer [54]):

$$B_{||} = 1.23\mu\mathrm{G} \left(\frac{\mathrm{RM}}{\mathrm{radm}^{-2}}\right) \left(\frac{\mathrm{DM}}{\mathrm{cm}^{-3}\mathrm{pc}}\right)^{-1}. \tag{2.47}$$

Some examples of polarization states of known sources include masers that are linearly polarized (due to synchrotron mechanisms) and pulsars (that will be a topic of discussing in the next sub-section) that can be almost completely linearly polarized with an added degree of circular polarization. Changes to the polarization state can only be due to ISM effects or inherent to mechanisms associated with the source.

Solar radio polarization was discovered in 1946, polarization of Jupiter followed in the 1950s, shortly after that the radio polarization of the Crab nebula was determined in 1957, polarization studies of radio galaxies and the Milky-way followed in

1962 (see Kraus [49]). This subsection is concluded by introducing the reader to a polarization study that were executed on a large scale galaxies, specifically IC342, see the study of Beck [7], that is a nearby spiral galaxy that reveals several polarized arms, see Fig.2.10.

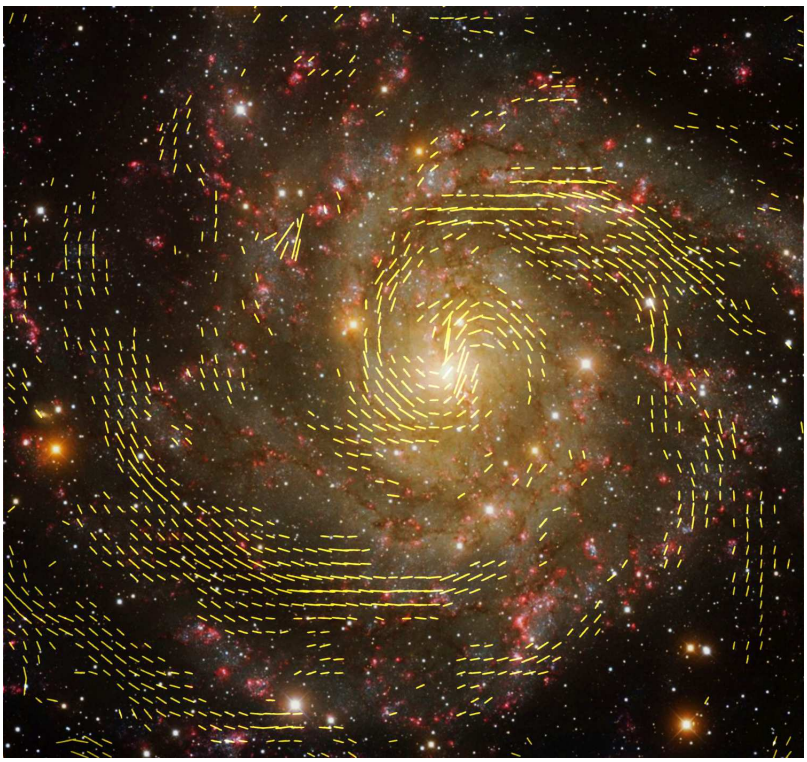

Fig. 2.10: Spiral galaxy IC324. Polarization vectors that were observed at 4.86 GHz and combined from interferometer data of the VLA and Effelsberg radio telescopes. Adopted from Beck [7].

2.1.5 Radiation of radio waves

The radio sky can be divided into several classes. See Fig. 2.11 for this classification of the classes (also see e.g. Burke [14] and Lorimer & Kramer [54]). These spectra are characterized by an quantity called the spectral index (α), related as:

$$S_\nu \propto \nu^\alpha, \tag{2.48}$$

with

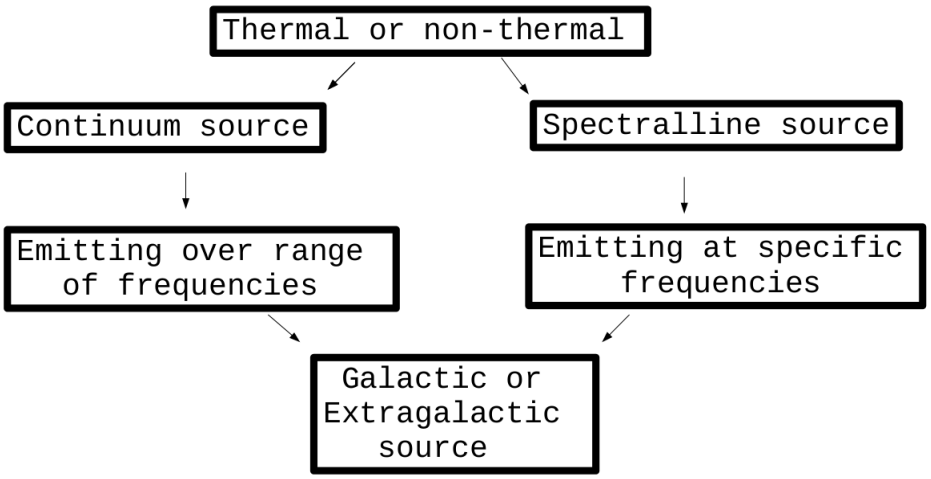

Fig. 2.11: Classification of the radio sky.

$$\alpha = 2, \text{for thermal sources,} \tag{2.49}$$

and

$$\alpha < 0, \text{for non-thermal sources.} \tag{2.50}$$

To prove these different spectral parameters for both thermal and non-thermal sources different emission mechanisms are investigated. For thermal radiation we turn to the theory of black body radiation following along the lines of Burke [14] (page 124). Black body radiation is produced by any optically object with temperatures larger than absolute zero. The power density of the black body can be described by the Planck distribution:

$$u_\nu \mathrm{d}\nu = \frac{8\pi h\nu^3}{c^3} \frac{1}{\exp(\frac{h\nu}{kT}) - 1} \mathrm{d}\nu, \tag{2.51}$$

or in terms of specific intensity it becomes

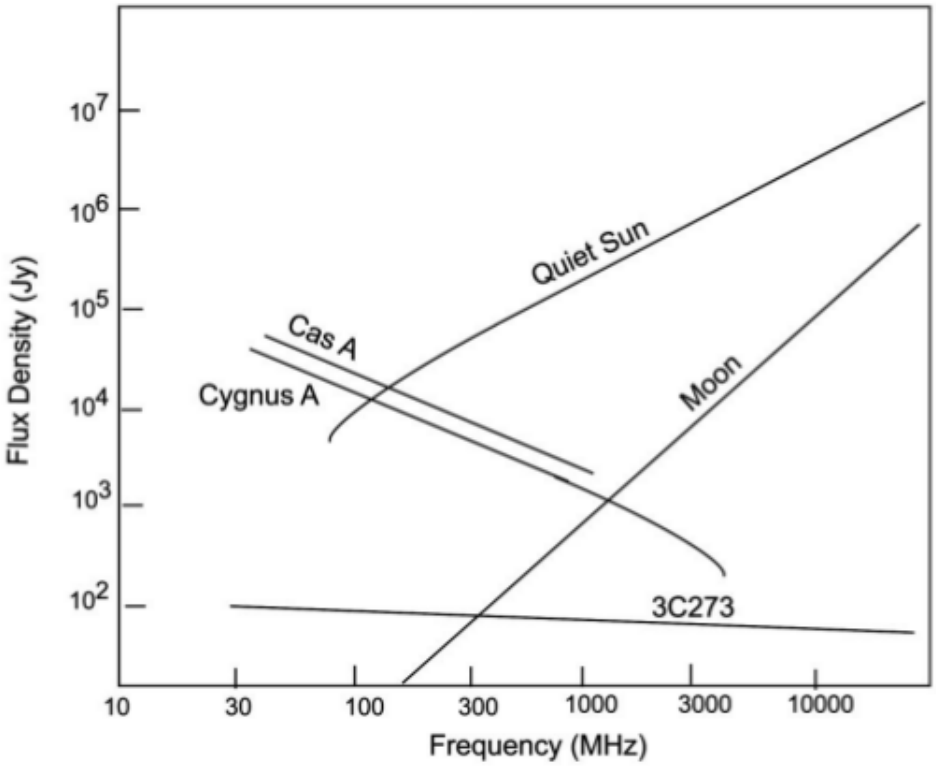

Fig. 2.12: Spectra of synchrotron sources (Cygnus A, Cas A etc.) and thermal sources (Moon and Sun) . Adopted from Pratap & McIntosh [72].

$$I_\nu \mathrm{d}\nu = \frac{2h\nu^3}{c^2} \frac{1}{\exp(\frac{h\nu}{kT}) - 1} \mathrm{d}\nu, \tag{2.52}$$

in the Raleigh-Jeans limit ($h\nu < kT$) (for radio observations the frequencies are well below the limit $\frac{kT}{h}$) this is

$$I_\nu \mathrm{d}\nu = \frac{2kT\nu^2}{c^2} \mathrm{d}\nu. \tag{2.53}$$

The latter equation is evidence for the black body spectral index given by $\alpha = 2$. In this limit the thermal spectra for the Sun (quite and/or active) can be correlated with Fig. 2.12. The total intensity of the black body is (Burke [14]):

$$I = \sigma T^4, \tag{2.54}$$

Non-thermal emission sources are dominated by synchrotron radiation of electrons due to their helical paths in the presence of strong magnetic fields. The important factor will be the speed v_e of the accelerated electron. The radiation produced by the electron is beamed in a narrow cone along the direction in which the particle is moving and is strongly polarized. The radiation will be mainly linearly polarized for a power-law electron distribution radiating in a large-scale homogeneous magnetic field, the degree of polarization can be inferred from the measured power-law of the radiation (see e.g. Rybicki & Lightman [81]). When the energy of the electron is relativistic (the electron is moving at relativistic speeds and $\gamma >> 1$) the standard cyclotron frequency of the electron in its helical path needs to be corrected, this is:

$$\nu_{\rm gyro} = \frac{\nu_{\rm cyclo}}{\gamma}, \tag{2.55}$$

here γ and $\nu_{\rm cyclo}$ are the Lorentz factor and the frequency of the cyclotron motion associated with the moving electron in its helical path, respectively. This relativistic motion produces a continuum spectrum with a peak frequency of (see e.g. Rybicki & Lightman [81]):

$$\nu_{\rm peak} = 0.29\gamma^2\nu_{\rm gyro}. \tag{2.56}$$

It is assumed that the energy distribution of relativistic electrons follow a power law distribution ($N(E) \propto E^{-p}$, where p is the power-law slope). Since the energy of the electron can be expressed as:

$$E = \gamma m_0 c^2, \tag{2.57}$$

it can be shown that $E \propto \nu_{peak}^{\frac{1}{2}}$. A collection of electrons yields a spectrum with energy density $u_\nu \propto \nu^{\frac{1-p}{2}}$. For cosmic rays the parameter γ in the energy spectrum has a value $p = 2.4$ (Rybicki & Lightman [81]), thus the spectrum of synchrotron

radiation will be:

$$u_\nu \propto \nu^{-0.7}. \tag{2.58}$$

This shows that $\alpha < 0$ for synchrotron type radiation. The following section will discuss two examples of radio thermal and non-thermal sources.

2.1.6 Local radio Universe

Radio sources found in the local universe can either be classified as thermal or non-thermal, i.e. the observed radiation is produced by thermal processes or through the process of magnetobremsstrahlung (synchrotron) emission. This section will be investigating supernova remnants (SNR) as possible synchrotron sources and the sun as a thermal emission source. The first source was chosen due to that fact that this introduction will be leading to the study of compact objects (neutron stars and pulsars).

It is inevitable that all stars will die and leave small condensed remnants in the wake of their spectacular death. If the star has a mass of $M > 8M_\odot$, the scene of death will be accompanied by a spectacular explosion leaving behind compact object, usually a neutron star or black hole in extreme cases where $M >> 8M_\odot$. See Fig.2.13 and Fig.2.14 for illustrations of the evolution of stars to the corresponding remnants, white dwarfs, neutron stars and black holes. It can be seen that the evolutionary path is dependend on the mass of the progenitor. van Dyk et al. [89] observed the supernova 1993J (in the galaxy M81) over several days. They observed an evolving radio profile over 200 days, see Fig.2.15.

As seen in Fig.2.15 the radio emission component is dominated by synchrotron radiation with two spectra, $S_\nu \propto \nu^{\frac{5}{2}}$ and $S_\nu \propto \nu^{\frac{1-p}{2}}$. To understand the radio synchrotron spectrum of 1993J, the theory of synchrotron absorption needs to be investigated. For the optically thick expanding shell, the brightness emission in the Rayleigh-Jeans limit ($h\nu << KT$) resembles

$$B_\nu \propto \nu^2 T. \tag{2.59}$$

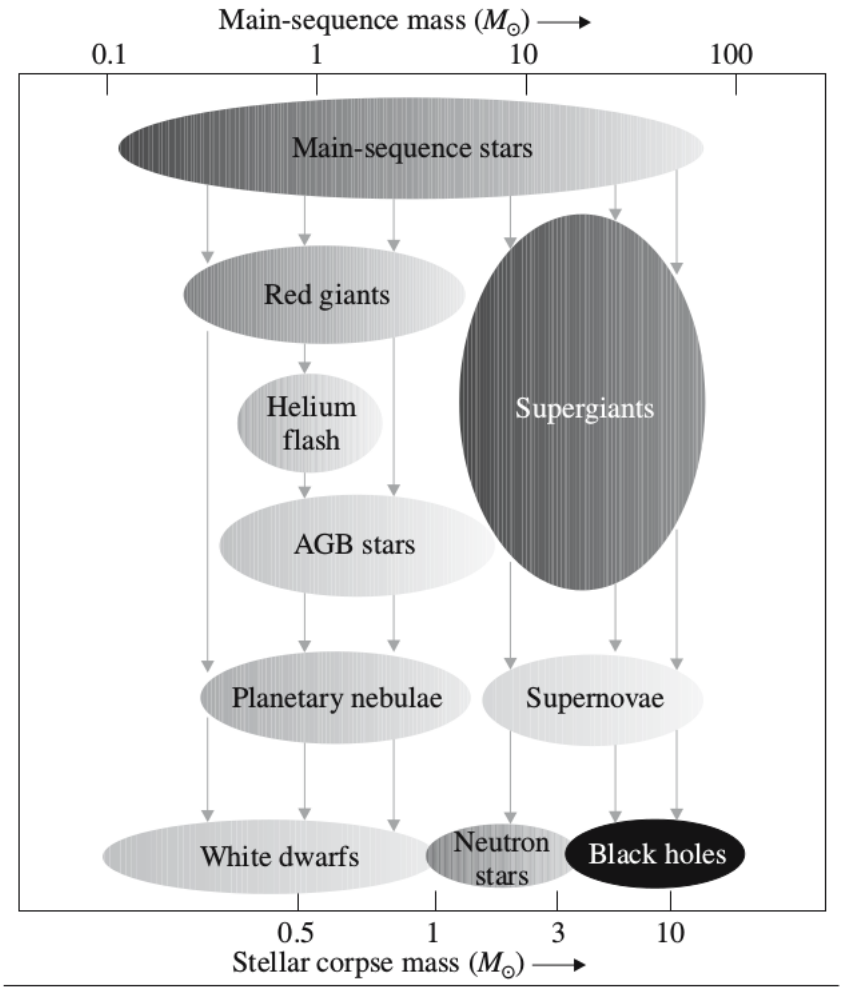

Fig. 2.13: Progenitors with different masses evolve to different remnants. Pulsars evolve from progenitors with masses of $> 8M_\odot$. Adopted from Camenzind [15].

However, a slight modification is introduced due to the fact that the expanding plasma contains a relativistic electron population which is in equilibrium with a population of thermal electrons, i.e. $kT \approx \gamma m_e KT$. Inside the plasma it is expected that the relativistic electrons are in thermal equilibrium with the thermal particles, ($kT \approx \gamma m_e c^2$), which leads to using the Rayleigh-Jeans approximation in the limit where $h\nu << kT$:

$$B_\nu \propto \nu^{\frac{5}{2}}. \tag{2.60}$$

Observing at radio frequencies where the limit is $h\nu >> kT$ it produces the characteristic spectrum of:

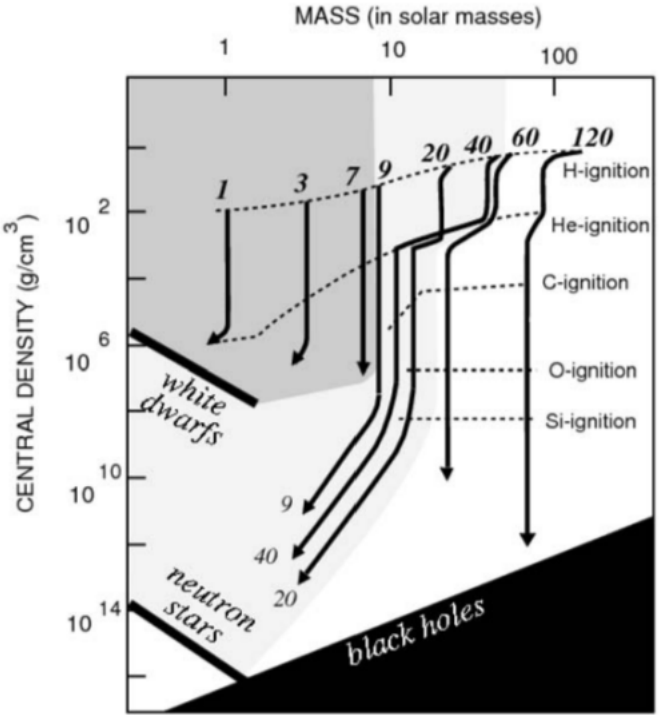

Fig. 2.14: Detailed evolution path different progenitors with different core densities. Adopted from Camenzind [15].

$$I_\nu \propto \nu^{\frac{1-p}{2}}. \tag{2.61}$$

It can be seen from Fig.2.15 that observations at different frequencies produce spectra with different turn-over frequencies. The self–absorption (turn-over) frequency is a crucial quantity for studying synchrotron sources: part of the reason is that it can be thought to belong to both regimes (thin and thick), this quantity is sensitive to the observation frequency.

Since synchrotron radio sources rely on magnetic fields as their central powering engine, it automatically implies that the observed synchrotron source's brightness can be used to estimate the magnetic field strength. This method can be of particular interest when observing sources like pulsars. From Fig.2.15 the turning point (from optically thick to optically thin) can be seen and can be used to estimate the magnetic field strength, this will be done along the lines of Ghisellini [32]. The turning point in the specific intensity spectrum is where $I_\nu \propto B^{\frac{-1}{2}}\nu^{\frac{5}{2}}$ (in the $h\nu << kT$ limit) is equal to ($I_\nu \propto B^{\frac{p+1}{2}}\nu^{\frac{-(p-1)}{2}}$ (in the $h\nu >> kT$ limit), which leads to

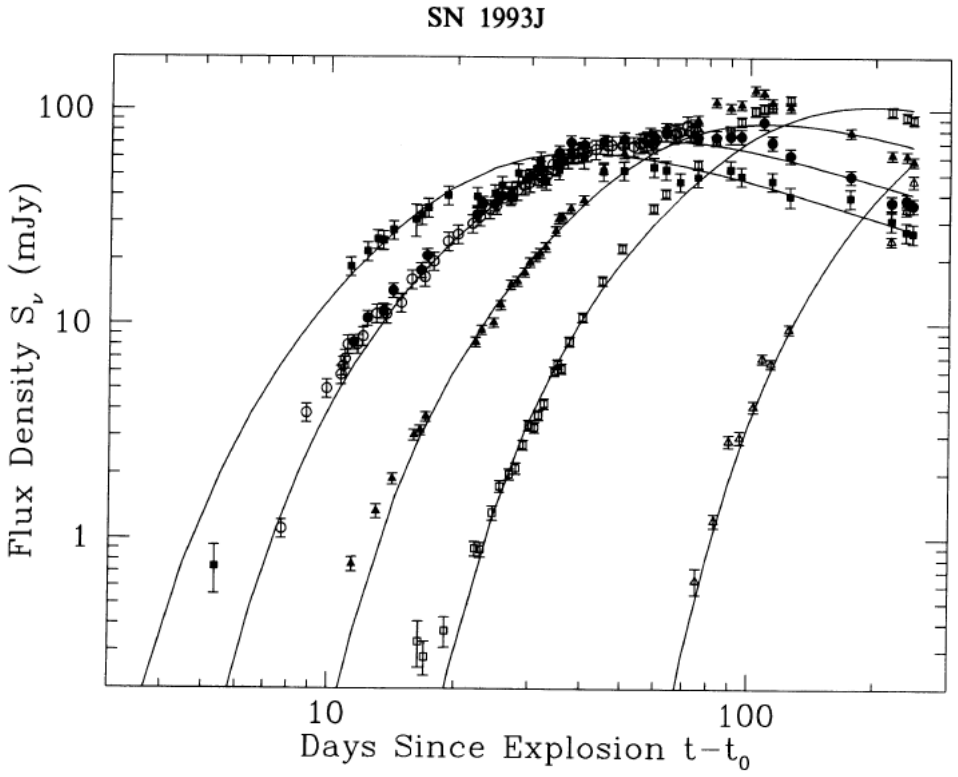

Fig. 2.15: Radio evolution of SN 1993J over 200 days. Adopted from van Dyk et al. [89]). From left to right we have observations at 1.3, 2, 3.6, 6 cm and 21 cm.

$$B \propto \frac{\nu^5}{I_\nu^2}. \tag{2.62}$$

An alternative method can also be followed along the lines of Pacholczyk [65]. The method of estimating the magnetic field strength from radio sources rely on the process of minimizing the total energy content associated with the relativistic particle population, i.e.

$$U_{\rm tot} = U_{\rm electron} + U_{\rm photon} + U_{\rm B}, \tag{2.63}$$

where $U_{\rm B}$ is the magnetic field energy content in a source with volume V, which is

$$U_{\rm B} = \frac{B^2}{8\pi}\Phi V, \tag{2.64}$$

where Φ represents the filling factor associated with the magnetic field. The energy content of electrons can be written as

$$U_{\rm elec} = c(\alpha, \nu_1, \nu_2) L_{\rm syn} B^{\frac{-3}{2}}, \tag{2.65}$$

with

$$c(\alpha, \nu_1, \nu_2) = \left(\frac{2\alpha - 2}{2\alpha - 1}\right)\left(\frac{\nu_1^{\frac{1-2\alpha}{2}} - \nu_2^{\frac{1-2\alpha}{2}}}{\nu_1^{1-\alpha} - \nu_2^{1-\alpha}}\right). \tag{2.66}$$

We assume that radiation is a peaked continuum concentrated at an critical frequency

$$\nu_{\rm c} = c_1 B \sin\theta \epsilon^2, \tag{2.67}$$

where ϵ represents the the energy of the electron. It can be assumed that the energy of the protons is some multiple of the electron energy. Thus,

$$U_{\rm tot} = (1 + k) c_{12} L_{\rm syn} B^{\frac{-3}{2}} + \frac{B^2}{8\pi}\Phi V. \tag{2.68}$$

If the contribution of the magnetic fields and the particles are approximately equal, the minimum energy condition can be derived, which is satisfied at $U_{\rm tot}(\min) = \frac{7}{3}U_B$. The magnetic field that minimizes the energy content is

$$B_{\rm eq} = \left(6\pi(1+k)c_{12}L_{\rm syn}\Phi^{-1}V^{-1}\right)^{\frac{2}{7}}. \tag{2.69}$$

From here the magnetic field associated with the source can be estimated.

The next section will introduce pulsars and the technicalities of pulsar astronomy.

2.2 Basic principles of pulsar astronomy

2.2.1 Modern day pulsar astronomy

Pulsars are rapidly rotating, highly magnetized compact objects that are the remnants of supernovae explosions. These objects contribute greatly to the fields of astrophysics and nuclear physics due to their peculiar high core density and fast spin-periods that range from milliseconds to several seconds (see e.g. Lorimer & Kramer [54] and Condon [20]).

Since their discovery in 1967 by Jocelyn Bell (Hewish et al. [38]) over 2500 pulsars have been discovered of which a large sample is monitored daily. A combination between new telescope design and monumental pulsar surveys driven by the large radio telescopes and interferometers are the key drivers behind new pulsar discoveries and theories. The discovery time-line of the known pulsars also follows this fine balance between discovery and instrument development (for an extensive list of milestones in pulsar astronomy see page 2 of Lorimer & Kramer [54]). In 1975 the first binary pulsar system was discovered by Russel Hulse and Joseph Taylor (both of Princeton University) which they used to test the theory of relativity and indirectly observed the effects of GW emission on an in-spiraling binary system. In 1982 the first millisecond pulsar was discovered by Backer et al. [5] and this detection marked the era of high accuracy pulsar timing and raised questions about pulsar evolution and birth rates. In 1993 Thorsett, Arzoumanian & Taylor [87] discovered the first triple system B1620-26, which consists of a pulsar, white-dwarf and a planet; this particular system set the stage for interesting tests of General Relativity to follow. In 2003 Burgay et al. [13] discovered the first double pulsar system J0737-3039 which can be used for several strong gravity tests and requires highly accurate pulsar timing procedures.

Even after these discoveries, the list of open questions stills remain substantial (see page 3 of Lorimer & Kramer [54]). These are also the questions that large scale

radio telescopes like MeerKAT, SKA and ALMA will be hoping the answer within the next few decades: What is the birth-rate of pulsars in our Galaxy, specifically concerning the evolution of pulsar populations on the $\dot{P}$-P diagram? What are the mechanisms that produce single isolated millisecond pulsars, black widows and redbacks; are there multi-wavelength campaigns for such systems? Do the magnetic fields of pulsars decay over long time periods and how does this influence the pulsed emission and the environment of the magnetosphere? What influence does the progenitor have on the pulsar, possible pulsar-disk interactions and variations in the stability of the clock? What model and diagnostic tools can we use to describe the pulsar's magnetosphere and the emission produced? Can astronomers unify the observed radio, gamma-ray and X-ray emission signatures into one pulsar model? Lastly, how complete is the pulsar spin-down model?

The next sections will investigate the basic theory of compact objects (originating from SN explosions) and the type of astronomy that can be associated with these compact sources. These sections will follow closely the methodology, outlines, hardware design and summaries described in Lorimer & Kramer [54].

2.2.2 Neutron stars

Following the detection of pulsars almost 60 years ago, it still remains a solid statement that pulsars are not well understood and drives a rich interdisciplinary research field. There exists an continuous battle with the intrinsic pulsar properties that we do not understand. These properties limit our modern day timing accuracy and reveals the need for long-term, high accuracy and multi-frequency observations of pulsars.

Pulsars are highly magnetized, rotating neutron stars (see Fig.2.16). The combination of the inclined magnetic and rotation axis, together with the rapid rotation, produce beams of radiation that sweep across the observer's line of sight and is recorded as a pulse by radio telescopes, producing a lighthouse effect, from here the name pulsar. The internal structure of the neutron star is complex and governed by the equation of state of the interior (which is not precisely known). The equation of state is the fundamental relationship between the density of the star's core and the pressure. Different flavors of the equation of state produce neutron stars with different radii, see Fig.2.17.

Many nuclear theoretical models attempt to predict the possible neutron star mass range, but due to their high density cores, the predictions remain uncertain (see e.g. Vranesevic et al. [92]) and references therein). The models predict an upper

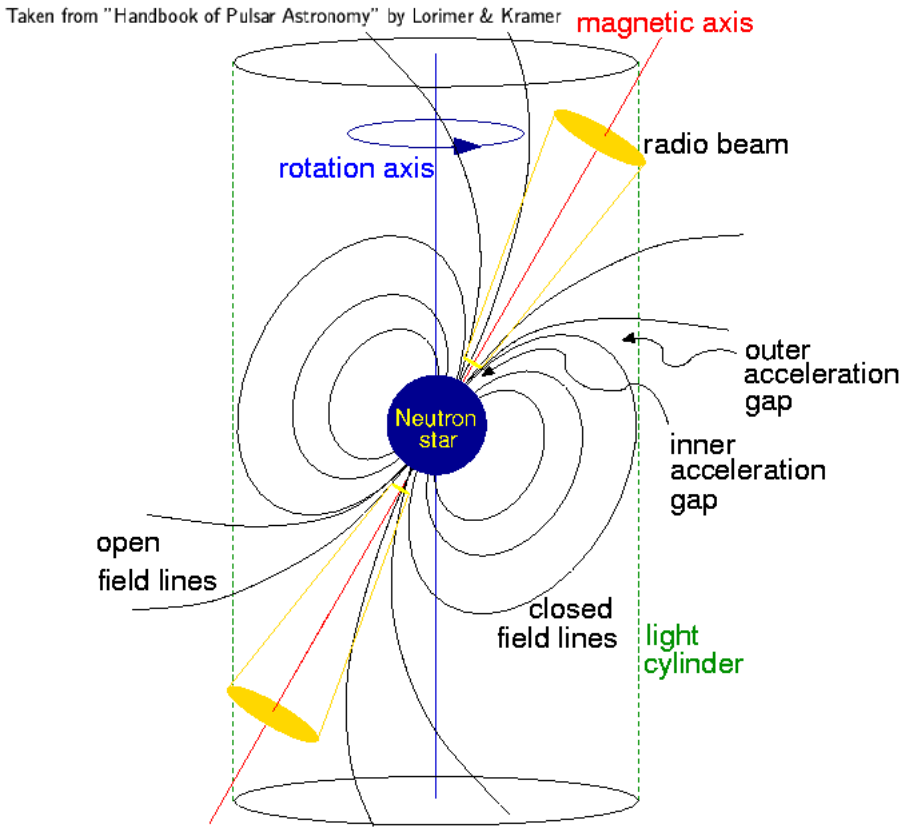

Fig. 2.16: Schematic model for a rotating neutron star. Adopted from Lorimer & Kramer [54].

limit of $2M_{\odot}$, but this limit can increase due to larger abnormal magnetic fields that support the neutron star from further collapse. See Condon [20] for a summary of how pulsar timing is used for constraining the equation of state neutron stars. These models also predict a lower radius for the neutron star of:

$$R_{\rm min} = 6.25{\rm km}\left(\frac{M}{1.4M_{\odot}}\right). \tag{2.70}$$

Most models predict that neutron stars could have a radius range of $R \approx 10-12$ km, but it can be seen from Fig.2.18 that there exist possible extreme cases. One such case is PSR B1937+24 that has a very short period of $P = 1.56$ ms and a radius of $R = 22.6$ km; these extreme characteristics will induce peculiar neutron star masses and sizes.

Moment of inertia can be attributed to the neutron star, if the neutron star is considered to be a solid rotating body. This moment of inertia can be written as:

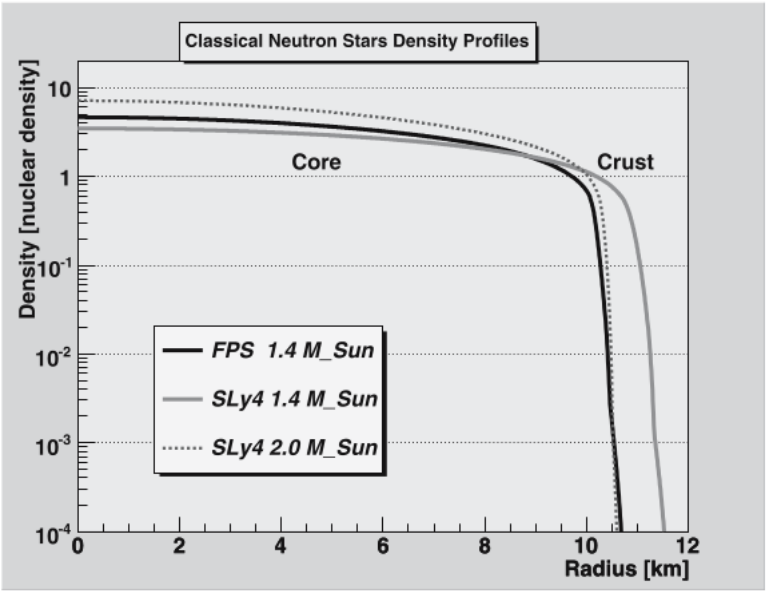

Fig. 2.17: Density profile of neutron stars as a function different combinations of interior particles. The FPS interior is a mix of Neutron,Protons, Electrons and Muons. The SLy interior is also a mix of Neutron, Protons, Electrons and Muons, but a different nuclear pressures as the FPS interior. Adopted from Camenzind [15].

$$I = kMR^2, \tag{2.71}$$

with $k = 0.4$ for a solid rotating sphere (by approximation). For practical applications and calculations the neutron star mass can be assumed to be $M = 1.4M_{\odot}$ and the radius to be $R = 10$ km, which lead to a moment of inertia of $I \approx 10^{38}\text{kg m}^2$. It remains true that this inertia value is highly uncertain due to the uncertainty in the neutron star's mass and radius.

In reality a neutron star is not a perfect sphere neither does it contain a constant density profile. Neutron stars contain layers of different material with a solid crust. It is believed that the neutron star contains a solid core with densities of $\rho \approx 10^{15}\text{g cm}^{-3}$. This core and the solid crust, wedges in a layer of neutron superfluid (Vranesevic et al. [92]). These unknowns in the neutron star structure largely contribute to their mysterious nature and importance in the nuclear field.

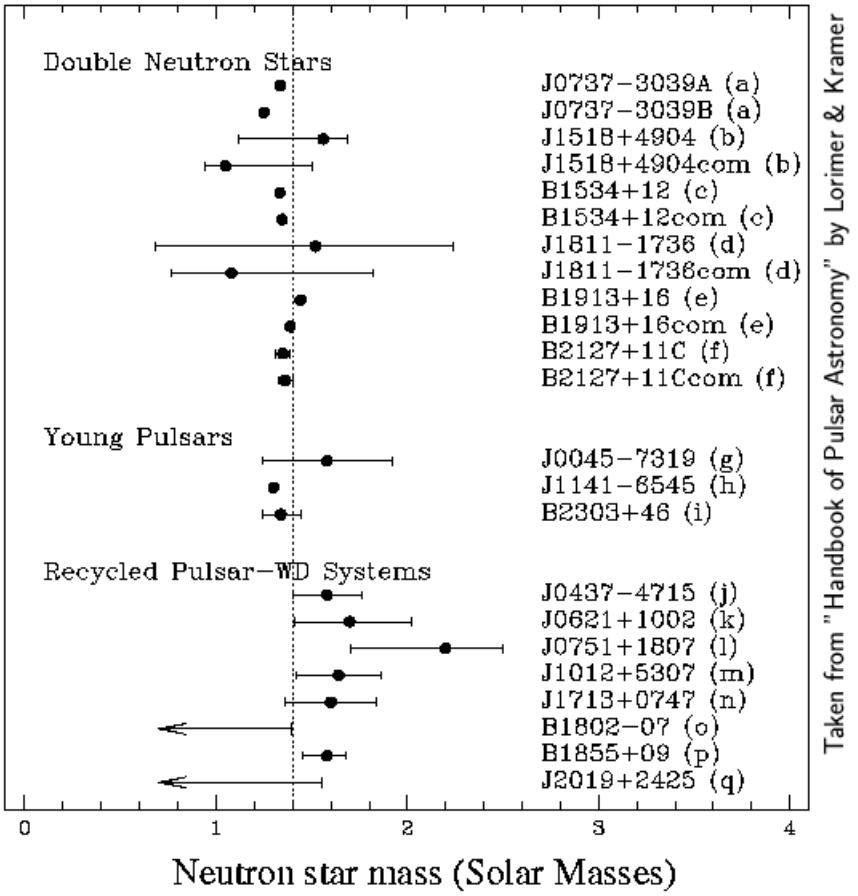

Fig. 2.18: The masses of several observed neutron stars. The mass of each neutron star was determined via timing analysis (Vranesevic et al. [92]). Adopted from Lorimer & Kramer [54]. See [15] and [20] for additional information and applications of the constraining of the neutron star EOS through pulsar timing.

2.2.3 Population of pulsars

More than 2500 pulsars are known and cataloged (see www.atnf.csiro.au). These catalogs contain several observed properties of the neutron stars including: spin-frequency (f), spin frequency evolution ($\dot{f}$), magnetic field intensity (B), age (τ), radio flux typically observed at 1400 MHz (S_{1400}), RA, DEC etc. One such catalog is the CSIRO ATNF pulsar catalog maintained by the Parkes radio pulsar group (www.csiro.au). One can download this catalog in a usable format and extract some information of the total observed pulsar population. This is known as the $\dot{P} - P$ diagram, see Fig.2.19.

The $\dot{P} - P$ diagram contains two separate classes of pulsars, namely normal pulsars (the larger cluster) and millisecond pulsars (the smaller cluster). This study will mainly focus on the latter mentioned pulsar groups. It is also evident from both Fig.2.19 and Fig.2.20 that there exist certain areas on the $\dot{P} - P$ diagram that con-

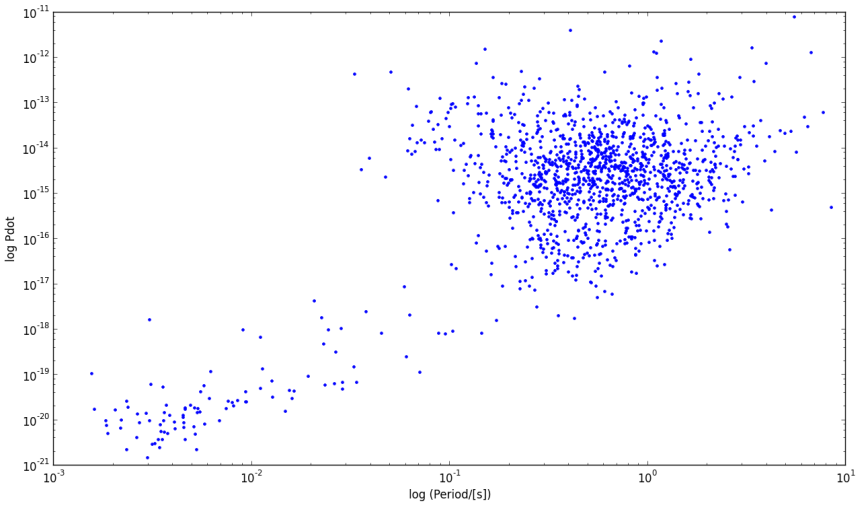

Fig. 2.19: The $\dot{P} - P$ diagram of the ATNF pulsar catalog (Lorimer & Kramer [54] and references therein)

tain no pulsars. It will be shown in the next section that one can use standard pulsar energetics to determine the age, spin-down and magnetic field size of each pulsar, this information can then be illustrated on the $\dot{P} - P$ diagram, to reveal a rather structured evolution pattern of the pulsars known today.

Following along the lines of Lorimer & Kramer [54], Fig.2.20 can be analyzed. Starting with the lines of constant age, magnetic field magnitude and luminosity ($\dot{E}$) that confine the population region on the $\dot{P} - P$ diagram. Pulsars under a certain $\dot{E}$ threshold switches off and end-up in the grave-yard region of the diagram. The millisecond pulsars (also called recycled pulsars) are generally old pulsars, they are recycled from accreting binary companions that spin them up to millisecond spin-periods. Different pulsar systems are indicated by different symbols: dotted circles illustrate millisecond pulsars in binaries, stars illustrate pulsars associated with supernova remnants, non-filled triangles are associated with soft gamma ray repeaters, filled triangles are the radio-quiet pulsars and dots represents the isolated pulsars. Associated with Crab and the Vela pulsars are areas for Crab-like and Vela-like pulsars, aged from 10-100 kyr and 10 kyr, respectively. The gray regions illustrate the areas where pulsars do not exist theoretically. It must be noted that the $\dot{P} - P$ diagram contains radio pulsars and radio-quiet pulsars, which pulsate mainly in X-rays and gamma-rays, e.g. Becker [8] (see Fig.2.21).

Using the $\dot{P} - P$ diagram one can already speculate about the evolutionary track of a normal young pulsar (like the Crab and Vela): pulsars are born with short spin-periods and large energetic spin-down, after 10^5 years the pulsar moves from

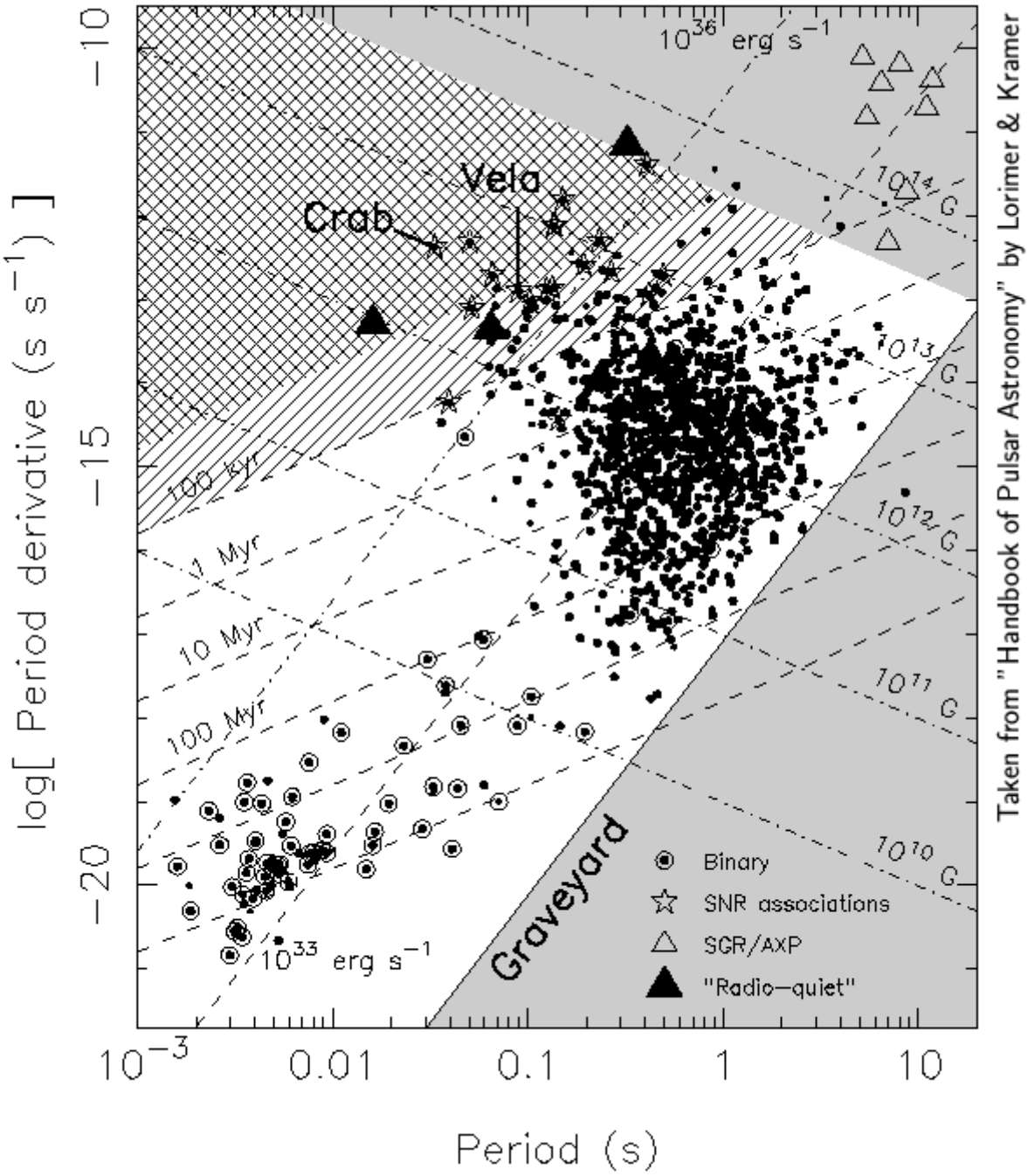

Fig. 2.20: The $\dot{P} - P$ diagram of the ATNF pulsar catalog (www.atnf.csiro.au). This particular $\dot{P} - P$ diagram contains age and magnetic field contours. See [20] for alternative representations of the $\dot{P} - P$ diagram. Adopted from Lorimer & Kramer [54].

the Crab/Vela regions into the main normal pulsar cluster, eventually becoming too faint to be detectable after 10^7 years.

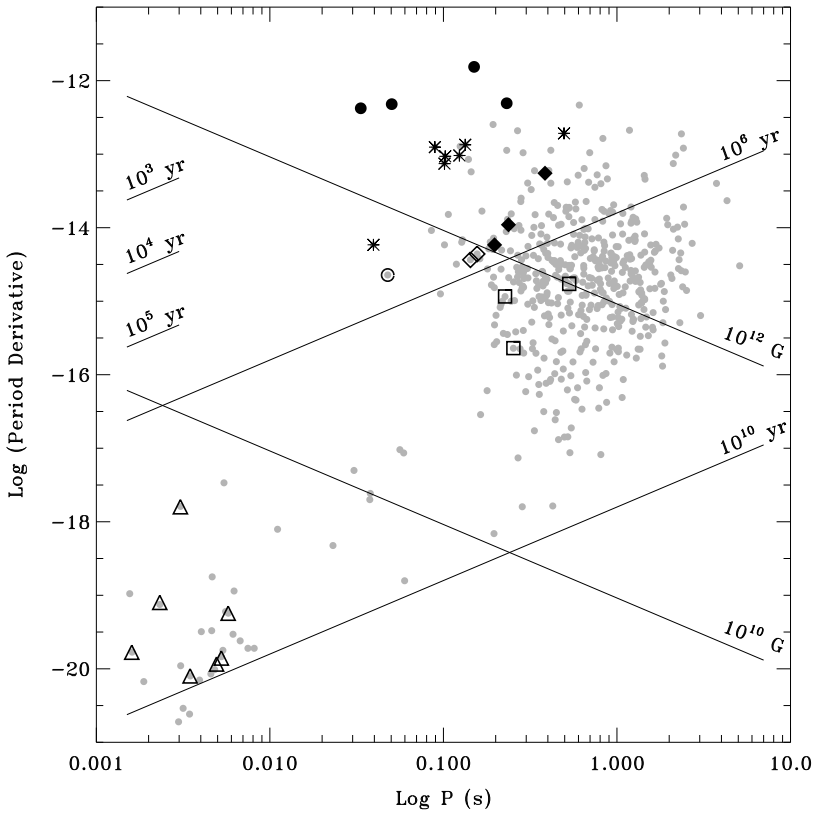

Fig. 2.21: Sample of rotation powered pulsars on the $\dot{P} - P$ diagram. X-ray detected pulsars are indicated by dots and stars which represent Vela and Crab like pulsars, squares represents the old and normal pulsars and the triangles represent the millisecond pulsars in the lower left corner. The gray dots represent the radio pulsars. Adopted from Becker & Truemper [9].

2.2.4 Spin evolution

The evolutionary track of a pulsar (as seen in Fig.2.20) suggests that the observed spin-periods associated with the pulsars, increase with time. Thus, pulsar's spin parameters evolve with time. The spin-down luminosity of a pulsar is:

$$\dot{E} = -4\pi^2 I \dot{P} P^{-3}, \tag{2.72}$$

which in combination with the standard assumed parameters of the pulsar ($M = 1.4 M_\odot$, $R = 10$ km and $I = 10^{38}\mathrm{kg\,m^2}$), leads to:

$$\dot{E} \approx -3.95 \times 10^{31} \mathrm{erg} s^{-1} \left(\frac{\dot{P}}{10^{-15}} \right) \left(\frac{P}{s} \right)^{-3}. \tag{2.73}$$

Different pulsars (from different pulsar populations) spin down at different rates depending on the total energy output and age of the pulsar. The pulsar can be considered as a rotating dipole (rotating magnet) that according to classical electrodynamics radiates energy at a rate of:

$$\dot{E}_{\mathrm{dipole}} = \frac{2}{3c^3} \mu^2 \Omega^4 sin^2 \alpha, \tag{2.74}$$

where μ is the magnetic moment, α is the separation angle between the spin-axis and the magnetic axis (see Fig.2.16) and Ω is the rotational velocity of the pulsar ($\Omega = 2\pi\nu$, where ν is the spin frequency of the pulsar). If we assume that $\dot{E} = \dot{E}_{\mathrm{dipole}}$, the power law relation can be derived (see e.g. Camenzind [15] or [20]):

$$\dot{\Omega} = -K\Omega^n, \tag{2.75}$$

where $n = 3$ is the braking index of the pulsar assumed to have a dipole magnetic field structure and K is some matching constant. This equation can be solved leading to spin-down age of the pulsar:

$$t = -\frac{\Omega}{(n-1)\Omega} \left(1 - \frac{\Omega^{n-1}}{\Omega_0^{n-1}} \right), \tag{2.76}$$

where Ω_0 is the initial rotational frequency of the pulsar at birth when formed in the supernova explosion. For the condition of $\Omega << \Omega_0$, the age of the pulsar becomes:

$$t_{\mathrm{sd}} = 0.5 \frac{P}{\dot{P}}, \tag{2.77}$$

specifically for $n = 3$ (Camenzind [15]). This age is known as the characteristic age of the pulsar and can be determined using pulsar timing techniques. The braking index of the pulsar can be measured by measuring the second spin frequency derivative ($\ddot{\nu}$), which leads to (e.g. Camenzind [15])

$$n = 2 - \frac{P\ddot{P}}{\dot{P}^2}. \tag{2.78}$$

If the observed pulsar braking index remained at $n = 3$, our spin-down prediction models of pulsars would have been complete, but this is hardly ever the case. The measurement of $\ddot{\nu}$ is contaminated with contributions to the pulsar model that we do not understand, called timing noise (see e.g. Chukwude [19]). Thus, the Crab pulsar has a characteristic age of $\tau_c \approx 1240$ yr, confirming its place on the $\dot{P} - P$ diagram (Abdo et al. [1]) and on the historic time line of ancient astronomers.

One more classification parameter is needed, namely the magnetic field strength. If we assume that the braking mechanism is dominated by magnetic dipole radiation, then we know that the magnetic dipole is related a magnetic field strength by:

$$B \approx \frac{\mu}{r^3}. \tag{2.79}$$

This relation can be used together with the rotational power loss equation due to dipole radiation to produce an estimate of the magnetic field strength at the surface of the neutron star (e.g. Goldreich & Julian [34]):

$$B_{\text{surface}} \approx (10^{12})(\sin\alpha) \left[\frac{\dot{P}}{10^{-15}}\right]^{0.5} \left[\frac{P}{\text{s}}\right]^{0.5} \text{G}, \tag{2.80}$$

where α is the inclination angle of the magnetic axis relative to the spin-axis, which produces a characteristic magnetic field strength of $10^{11} - 10^{12}$G. This environment is principally the core engine for the observed radio to gamma-ray radiation produced by pulsars (Abdo et al. [1]).

2.2.5 The pulsar magnetosphere

The neutron star can not be considered as an atmosphereless rotating compact object ever since its first appearance in the radio band nearly 60 years ago. Since coherent beamed radiation is observed from a pulsar, there must exist plasma near the surface of the neutron star and particles are accelerated from this plasma along magnetic field lines to emit a broad spectrum of energies.

The plasma-filled atmosphere of the neutron star that is susceptible to the extreme magnetic fields is known as the pulsar magnetosphere and is not well understood. The basic model that describes this highly dynamic magnetosphere is known as the Goldreich-Julian model (Goldreich & Julian [34]). The induced electric field in the laboratory frame is (Goldreich & Julian [34]):

$$\boldsymbol{E} = -\frac{(\boldsymbol{\Omega} \times \boldsymbol{r}) \times \boldsymbol{B}}{c}. \tag{2.81}$$

Due to the rapid rotation of the neutron star there will be a spatial charge distribution inside the star due to extreme centrifugal forces, which leads to an external magnetic field that can be derived from Maxwell's equations together with the necessary boundary conditions (e.g. Goldreich & Julian [34]).

The gathered surface charges induce an external quadrupole electric field with a corresponding field magnitude at the surface of the neutron star of:

$$E_{\text{surface}} = \frac{\boldsymbol{E}.\boldsymbol{B}}{B} = -\frac{\Omega B R}{c}\cos^3\theta. \tag{2.82}$$

This field produces a force on the surface particles that exceeds the gravitational forces by many orders of magnitude (from here the filled atmosphere). These conditions strip the particles from the neutron star surface and fill the surrounding vacuum with plasma, having a density of (e.g. Goldreich & Julian [34]):

$$\rho_e = \frac{B\Omega R^3}{4\pi c r^3}(3\cos^2\theta - 1). \tag{2.83}$$

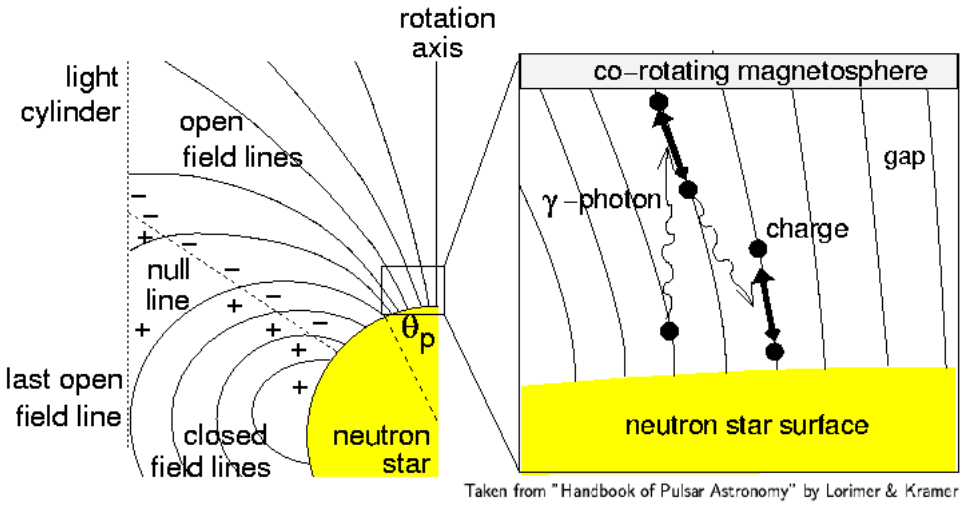

Fig. 2.22: The pulsar magnetosphere as depicted by the Goldrech-Julian model, adopted from Lorimer & Kramer [54]).

The plasma filled atmosphere of the neutron star co-rotates with the compact object and the plasma is accelerated along the magnetic field lines. This co-rotation sculptures the idea of the light cylinder (see Fig.2.16), which essentially is the distance from the neutron star where the co-rotating plasma reaches the speed of light ($R_{\rm LC} \to c$). The radius of the light cylinder is:

$$R_{\rm LC} \approx 4.77 \times 10^4 \,{\rm km} \left(\frac{P}{\rm s}\right). \tag{2.84}$$

Inside the co-rotation radius the magnetosphere consists of regions of closed and open field lines (see Fig.2.22). The open field lines region define the polar cap of the neutron star and its outer edges are enclosed by the last open field lines located at:

$$R_{\rm polar} \approx R \sin\theta_{\rm polar} = 150 \,{\rm m} \left(\frac{P}{\rm s}\right)^{0.5}. \tag{2.85}$$

The Goldreich-Julian model illustrates a very basic model of the neutron star that can at least explain the presence of the magnetosphere filled with plasma and hence the presence of the observed pulsed emission. In reality the observed radio emission is complex and not well understood, thus more complicated neutron star models

have since emerged that incorporate the broad spectrum emission phenomena largely driven by magneto-hydrodynamic simulations.

If charge flow along open field lines is assumed in the magnetosphere of the rapidly rotating pulsar (Cheng, Ho & Ruderman [18]), then it can result in extended regions of charge depletion in the outer magnetosphere of the pulsar. The outer-gap is defined as the elongated region wedged in between the last open field line and the null surface, see Fig.2.22 and 2.16. Within this outer-gap region plasma can be accelerated due to the large non-vanishing component of $\boldsymbol{E}.\boldsymbol{B}$ producing a potential drop of 10^{15} V along $\boldsymbol{B}$, ultimately setting the stage for high energy pulsed emission. It is believed that radio emission originates from the polar cap region (via curvature radiation) and that gamma ray emission originates in the outer gaps (magnetic field strengths in the outer gaps are relatively smaller in that of the polar cap, see e.g. Cheng, Ho & Ruderman [18] and Ruderman & Sutherland [80]). Both pulsed radio and gamma rays produced by the pulsar can be used for timing purposes, but with different induced timing accuracy (see Fig.2.23), this will be discussed in the next chapter on pulsar timing (both in radio and gamma-ray).

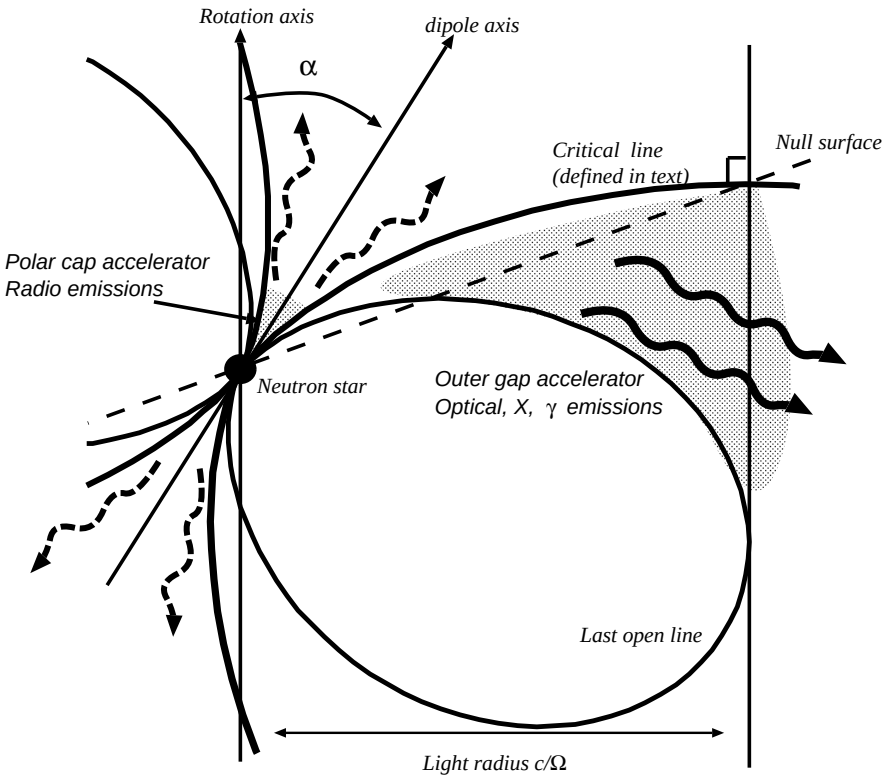

Fig. 2.23: The pulsar magnetosphere depicting the geometrical representation of the polar cap and the outer cap regions, adopted from Takata & Chang [86].

2.2.6 Beyond the polar cap

It remains useful to investigate alternative emission models when trying to tie any observed dynamic features in the broad spectrum emission of pulsars to any activity in the magnetosphere of the pulsar itself. These models describe the interplay between plasma in the magnetosphere and the strong magnetic fields of the pulsar, specifically focusing on different regions of emission producing different energies of pulsed emission that are associated with different regions of the pulsar magnetosphere. One such model is called the striped wind model; whereby in the case of an oblique rotator, significant energy can be carried away from the neutron star in the form of a toroidal magnetic field of alternating polarity (due to the alternating polarization states of the pulsar's poles, see e.g. Punsly & Coroniti [73] and Michel [61]). This particular emission process is believed to occur outside the light cylinder. When correlating radio and higher emission pulsar pulse profiles, it could be useful to consider that 3D magneto-hydrodynamic force-free simulations of pulsar magnetospheres suggest that the high energy pulse profiles are reproduced better when assuming that the emission arises just outside the light cylinder (see e.g. Pétri [74] and Pétri & Dubus [75]).

This model was specifically applied to PSR B1259-63 that is close to an orthogonal rotator due to its double radio pulse and the ability to observe both its emission poles. Observations of pulsar jets (such as the Crab and Vela) suggest that the neutron star's spin is transcribed in the wind with alternating polarization (from here the name striped wind), see Fig.2.24.

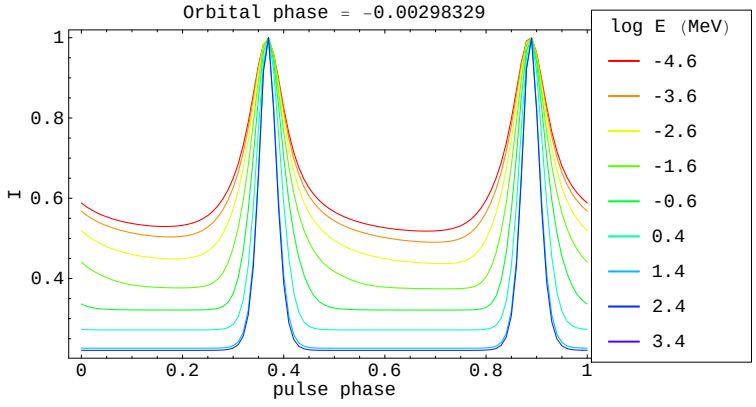

Fig. 2.24: The striped wind model can also be applied to gamma ray binaries, specifically also including orbital dependencies in the model's predictions. Adopted from Pétri & Dubus [75].

The phased resolved polarization properties for gamma ray pulsars can also be modeled using the striped wind model (see Cerutti, Mortier & Philippov [16]). The mod-

elled phase resolved properties produced by the striped wind model can be matched to the Crab pulsar's phase resolved optical data, see Fig.2.25.

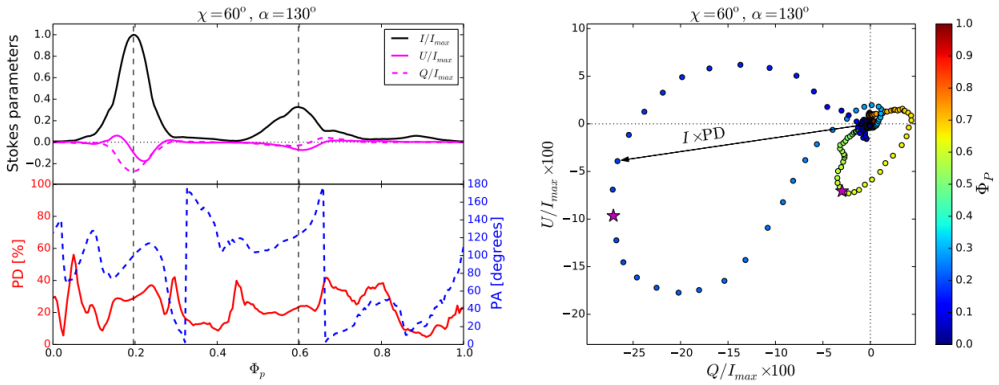

Fig. 2.25: Calculated polarization properties of Crab-like properties specifically for the solution with $\chi = 60\,\text{deg}$ ($\chi = \beta$ in standard geometrical model) and magnetic inclination of $\alpha = 130\,\text{deg}$. Adapted from Cerutti, Mortier & Philippov [16].

2.2.7 Pulsar energetics

In this section measurable quantities that can be associated with the pulsar are derived, namely radio luminosity (L) and flux (S). Estimating the luminosity of a pulsar is difficult since only a one dimensional cut through a beam of unknown structure and complexity is observed (this topic induces extensive research efforts). Other major issues are the distance to the pulsar that is difficult to obtain and the varying flux due to interstellar effects (ISM), all of which can be improved by observing pulsars with wide-band interferometers.

Following along the lines of [49], Camenzind [15] and Condon [20], if we idealistically assume that the emission along the observer's line of sight is a total representation of the radio emission beam (whether hollow or patchy), then the luminosity of a pulsar at a distance d becomes:

$$L = \zeta d^2 \int S(f_{\text{peak}}) df, \tag{2.86}$$

where ζ is the solid angle spanned by the beam and is related to the opening angle of the beam (ρ) by

$$\zeta = \int 2\pi \sin\rho d\rho = 4\pi \sin^2\left(\frac{\rho}{2}\right). \tag{2.87}$$

The observed peak flux density is generally expressed as the mean flux density (S_{mean}), i.e. the average observed intensity over the full rotation cycle of the pulsar. The mean flux density has a power-law dependency on the observing frequency of the experiment,

$$S_{\text{mean}}(f) = S_{\text{mean}}(f_0)\left(\frac{f}{f_0}\right)^{\eta}, \tag{2.88}$$

where $S_{\text{mean}}(f_0)$ is the mean flux density measured at the centered frequency f_0. To derive the response of the receiver to pulse with known mean flux density, an hypothetical pulse is generated in the form of a "top-hat" pulse (with pulse width W). This assumption is purely for estimation purposes since in reality the pulse is far from a perfect top-hat pulse and follows an unique pulse morphology. Knowing that the pulse is sometimes on and other times off, the mean flux density can be estimated with the relation $S_{\text{mean}} = \frac{WS_{\text{peak}}}{P}$. Together with the top-hat pulse duty cycle, $\delta = \frac{W}{P}$, an expression for the luminosity of the pulsar can be obtained:

$$L = \frac{2\pi d^2}{\delta}(1-\cos\rho)S_{\text{mean}}(f_0)\frac{f_0^{-\eta}}{\eta+1}\left(f_2^{\eta+1} - f_1^{\eta+1}\right), \tag{2.89}$$

here $f_1 - f_2$ is the frequency range of the observation (also known as the bandwidth).

The radiometer equation (see chapter 1.3) suggested a uncertainty in the measurement of the flux density of a source due to receiver's varying system noise. This radiometer equation can be modified to calculate the minimum observable flux density associated with a pulsar, i.e. the minimum flux density required to exceed the system noise of the receiver. The radiometer equation was previously defined in the introduction of radio astronomy:

$$\Delta T_{\text{system}} = \frac{T_{\text{system}}}{\sqrt{n_p B\tau}}, \tag{2.90}$$

where n_p represents the number of polarizations, B represents the bandwidth and τ represents the total observation time (also known as integration time). This equation needs to be modified for a top-hat pulse (which is the idealistic representation of the observed radio pulse) of certain width (W), period (P) and peak temperature $T_{\rm peak}$. The fluctuations in the receiver temperature of the pulse switching between on and off states needs to be calculated (producing either $T = T_{\rm peak}$ or $T = T_{\rm sys} - T_{\rm peak}$ which idealistically represent the on or off state of the pulsar). A good start will be to break up the total integrated observation time, τ, into the time intervals that the signal is on or off:

$$\tau = \tau_{\rm on} + \tau_{\rm off}, \tag{2.91}$$

where $\tau_{on} = \frac{W\tau}{P}$ and $\tau_{off} = \frac{(P-W)\tau}{P}$, thus the total fluctuation of the receiver output due to the on and off state is:

$$\Delta T_{\rm sys} = \sqrt{[\Delta T_{\rm sys}(\tau_{\rm on})]^2 + [\Delta T_{\rm sys}(t_{off})]^2}. \tag{2.92}$$

The modified radiometer equation that includes both the on and off states of the signal can now be written as :

$$\Delta T_{\rm sys} = \frac{T_{\rm system}}{\sqrt{n_{\rm p} B\tau}} \left(\frac{P}{\sqrt{W(P-W)}} \right). \tag{2.93}$$

The signal to noise ratio is defined as $S/N = \frac{T_{\rm peak}}{\Delta T_{\rm sys}}$, which is:

$$S/N = \sqrt{n_{\rm p} B\tau} \frac{T_{\rm peak}}{T_{\rm sys}} \frac{\sqrt{W(P-W)}}{P}. \tag{2.94}$$

The S/N can be converted to a flux density by using the telescope gain ($S_{\rm peak} = \frac{T_{\rm peak}}{G}$ in units of Janskys), the mean flux density over the whole pulse period becomes:

$$S_{\rm mean} = S_{\rm peak}\frac{W}{P} = \frac{WT_{\rm peak}}{GP}. \tag{2.95}$$

Substituting the expression for $T_{\rm peak}$ into the expression for the S/N and assuming that $S_{\rm mean} = S_{\rm min}$, the minimum observable flux density associated with the pulsar can be retrieved:

$$S_{\rm min} = \frac{(S/N)T_{\rm sys}}{G\sqrt{n_p\tau B}}\sqrt{\frac{W}{P-W}}. \tag{2.96}$$

It is clear that the parameters that determine the "visibility" of pulsars with regards to radio telescopes, depend on the S/N, width of the pulse, period of the pulsar, observation bandwidth and system noise. Most importantly, different populations of pulsars will not be equally "visible" by the same radio telescope.

2.2.8 Pulsed emission: the light-house model

The pulsar light-house model is based on a stable narrow radio pulse from the open field lines region of the rapidly rotating and magnetized neutron star that is typically associated with the polar cap region. The standard profile of a pulsar is normally hundred to thousands of pulses summed/stacked together and is used for timing purposes since it is stable and is needed for a stable reference to compute the time of arrival (TOA) at a given frequency (see Fig.2.26).

In the broader picture the radio beam (whether patchy or hollow) is produced by plasma being stripped from the surface of the neutron star and flowing along the open magnetic field lines and narrowly radiates in the direction of acceleration tangential to the field line (see Goldreich & Julian [34] and Fig.2.22). Considering Fig.2.27, the emission cone has angular opening ρ, the rotation and magnetic axis are offset with angle α. The cone's opening angle is cut by the line of sight of the observer which defines β, measured from the magnetic axis to the line of sight. The position angle is measured with respect to the projected direction of the magnetic

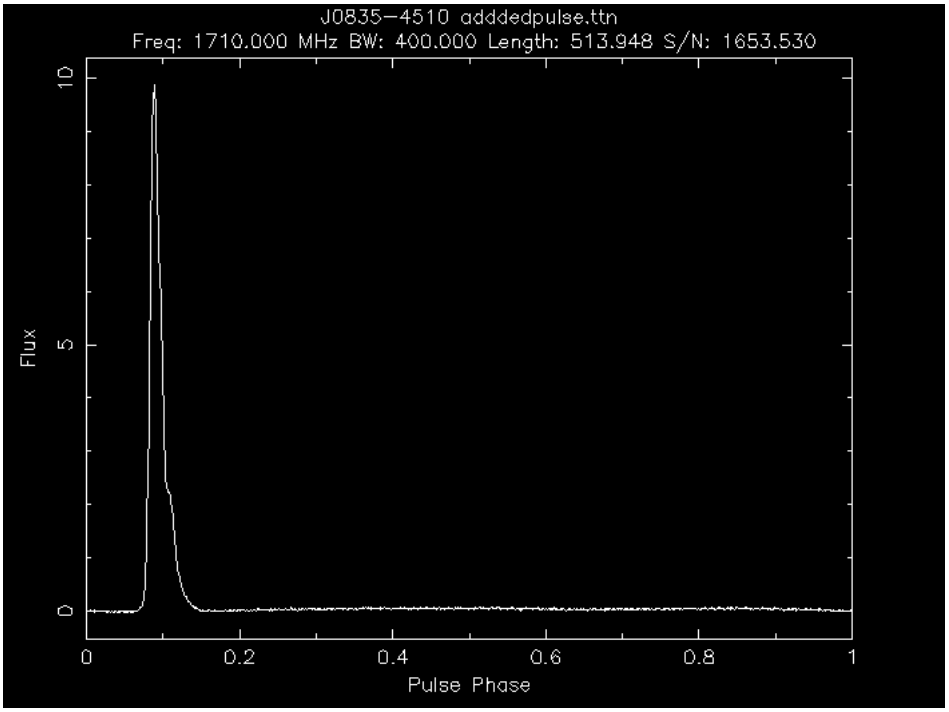

Fig. 2.26: The standard pulse of Vela with a large signal to noise ratio.

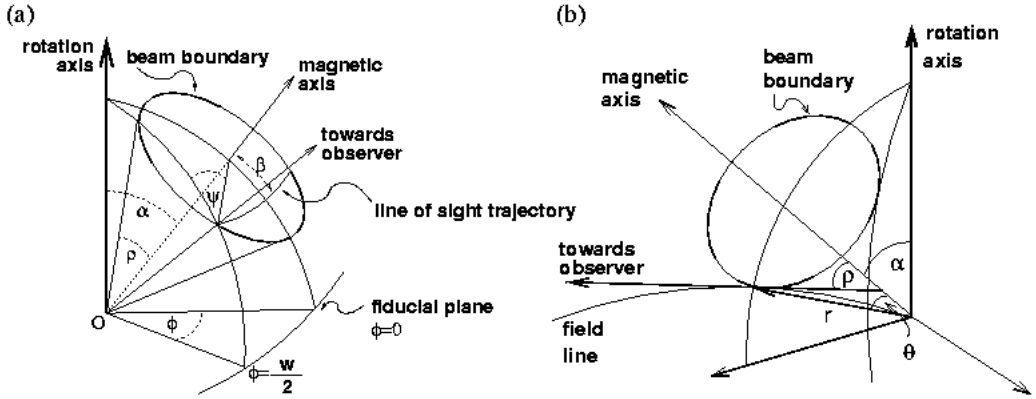

Fig. 2.27: a) Geometry of the pulsar emission beam (adopted from Lorimer & Kramer [54]), (b) the angular radius of the emission cone, ρ.

axis.

The width of the pulse can be expressed as:

$$\sin^2\left(\frac{W}{4}\right) = \frac{\sin^2\left(\frac{\rho}{2}\right) - \sin^2\left(\frac{\beta}{2}\right)}{\sin\alpha\,\sin(\alpha+\beta)}. \tag{2.97}$$

The opening angle of the emission cone (ρ) can be related to the angle between the observer's line of sight and the magnetic axis (θ) in polar coordinates (see Fig.2.27(b)), which is:

$$\tan\theta = -\frac{3}{2\tan\rho} \pm \sqrt{2 + \left(\frac{3}{2\tan\rho}\right)^2}. \tag{2.98}$$

If the emission region is close to the magnetic axis ($\rho < 30^\circ$), then

$$\theta \approx \frac{2\rho}{3}, \tag{2.99}$$

thus the opening angle becomes

$$\rho \approx 1.24^\circ \left(\frac{r_{\rm em}}{10\,{\rm km}}\right)^{0.5} \left(\frac{P}{\rm s}\right)^{-0.5}. \tag{2.100}$$

Here $r_{\rm em}$ is the emission height. The opening angle scales with $P^{-0.5}$. The observed opening angle deviates from the power-law for several reasons: the dipolar field assumption breaks down and the angles needed to construct the beam geometry, are not accurately known.

If the beam-width for several observed pulses are calculated at different frequencies, the beam width decreases as the frequency increases. This translates to radio emission associated with a specific emission height (since higher frequency emission is produced nearer to the neutron stars surface). This phenomena is not generally seen in millisecond pulsars (pulse width remains stable over different observational frequencies), since the size of the magnetosphere is smaller compared to normal pulsars (since $R_{\rm LC}$ is smaller and leaves less room for beam spreading and strong frequency dependencies) Dolch et al. [27]. This phenomena will be discussed in the next subsection.

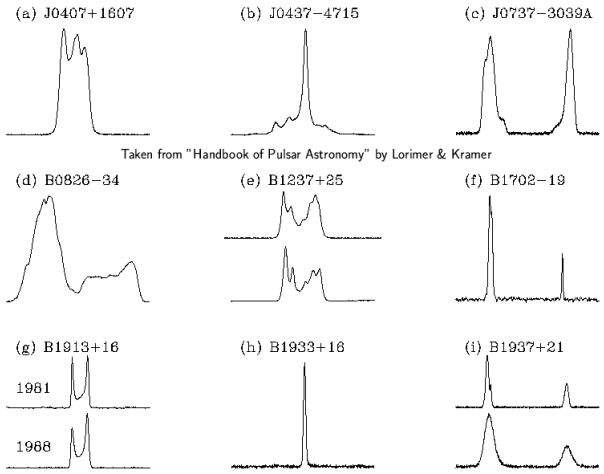

Fig. 2.28: Integrated profiles of several well-observed pulsars, one can clearly see different beam structures. Adopted from Lorimer & Kramer [54].

As seen in Fig.2.28 some pulsars have more than one or two pulse structure components. To account for this type of observed structure there currently exist two beam models: the hollow cone model (Rankin [78]) and the patchy beam model (Lyne & Manchester [57] and Karastergiou & Johnston [46]). The patchy beam model proposes that the interior of the radio beam is filled randomly with emitting regions since only parts of the emitting region are active (from here the term patchy). In the other hand, the hollow cone model implies that if the observer's line of sight cuts the radio beam across longitudinally, then several beam components will be observed and if the line of sight grazes the radio beam only one pulse component will be observed. Pulsar observations generally support the cone model, since observations follow the opening angle power-law, $\rho \approx P^{-0.5}$.

Particles that gyrate around magnetic fields produce electromagnetic radiation that have polarization properties. When observing pulsars, the dominant emission mechanism is synchrotron radiation and the radiation is predominately linearly polarized. The polarization can be characterize by comparing the decomposed parallel and perpendicular signal components of the projection of the magnetic field per unit frequency (see Fig.2.29, adopted from Rybicki & Lightman [81])

$$\Pi(\omega) = \frac{P_{\parallel}(\omega) - P_{\perp}(\omega)}{P_{\parallel}(\omega) + P_{\perp}(\omega)}. \tag{2.101}$$

The best supporting argument for the cone model is the behavior of the polariza-

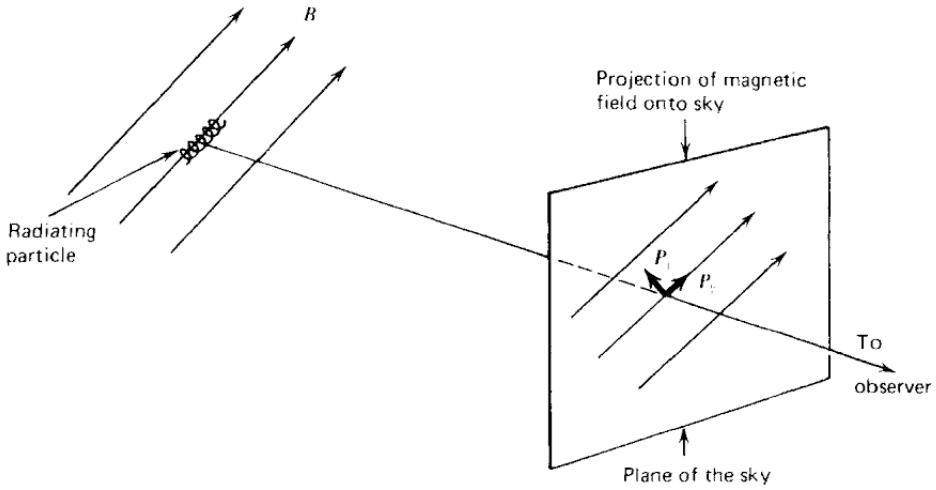

Fig. 2.29: Decomposed parallel and perpendicular components of the observed signal power produced by synchrotron radiation. Adopted from Rybicki & Lightman [81].

tion angle (PPA), $\Psi = 0.5 \tan^{-1}\left(\frac{U}{Q}\right)$, observed in integrated pulses (Radhakrishnan et al. [76]). This is predicted in the Rotating Vector Model (RVM) which states: the polarization position angle follows an S-shape swing since the direction from the point of emission to the magnetic axis varies slowly at the edges of pulse longitude and changes rapidly at the assumed profile center as the pulse sweeps by. The PA changes with (see Fig.2.28):

$$\tan(\Psi - \Psi_0) = \frac{\sin\alpha \sin(\psi - \psi_0)}{\sin(\alpha+\beta)\cos\alpha - \cos(\alpha\beta)\sin\alpha\cos(\psi - \psi_0)}, \tag{2.102}$$

where β is the impact factor, α is the magnetic inclination angle and ϕ is the rotational phase of the pulsar.

The magnetosphere of the pulsar is filled with ionized plasma that can be accelerated along the magnetic field lines to produce a wide variety of emission via the process of pair cascade. This process will produce emission ranging from radio (as seen in above mentioned radio light house model) to gamma ray pulses. In the outer-gap models (e.g. see Abdo et al. [1]) the gamma-rays are generated by the ultra-relativistic charged particles in the outer-gap (near the location of the null-line, $\Omega.\boldsymbol{B} = 0$, which separates the charges with different signs), see Fig. 2.16, producing wide gamma-ray fan beams from each pole. However, radio emission emanates from near the magnetic poles of the pulsar via electron-positron cascade narrowly beamed along the open field lines producing coherent pulsar emission. The timing procedure

of the seemingly different pulsed emission mechanisms will be discussed in the next chapter.

2.2.9 Radius to Frequency Mapping

This section will be a summary of the work that was done in Chen & Wang [17] and references therein. It is believed that pulsars exhibit frequency dependence of the average stable pulse (i.e. the profile morphology is transient across several frequencies) profile of which some pulsars's profiles remain stable over a wide-band of observation. One particular pulsar, PSR B1133+16, exhibits the phenomena of its double peaked profile moving closer to one another in pulse longitude as the band moves from several Megahertz to Gigahertz. Even the pulsar of interest for this study, PSR J1326-5859, illustrates morphology changes in the profile when observing at higher frequencies, with additional components of the pulse profile appearing and single peaked pulse profile structures becoming singular. It is commonly believed that the width of the pulsar profile is dependent on the observation frequency, specifically the separation between the double peak feature that many pulsars exhibit. Most of the earlier work that were done had been based on the Thorsett-relation, which can be stated as:

$$\theta = A\nu^{-\alpha} + C, \tag{2.103}$$

where θ is the opening angle of the radio pulse (see e.g. Fig.2.30) and clearly illustrates a power-law frequency dependence. The main idea behind radius-to-frequency-mapping (RFM) is the pulse profile width generally increasing with decreasing observing frequency that can be interpreted as some relation to emission radius, the height of emission and observation frequency. This concept was introduced in the 80's by Cheng, Ho & Ruderman [18], who suggested that the height of emission might be determined by the local plasma density. The frequency dependence is best seen in samples that illustrate the traditionally believed hollow cone emission model. For normal pulsars the emission heights can be several hundred kilometers. To illustrate the RFM effect the reader can refer to Fig2.31, Fig.2.32, Fig.2.33, Fig.2.34 for a collection of pulsars that follows the power-law relation, see Fig.2.35 for a collection of pulsars that do not follow the RFM. The reader can refer to Fig.2.30 for the setup and geometry of the RFM model and an illustration of the different emission heights with respect to the surface of the neutron star.

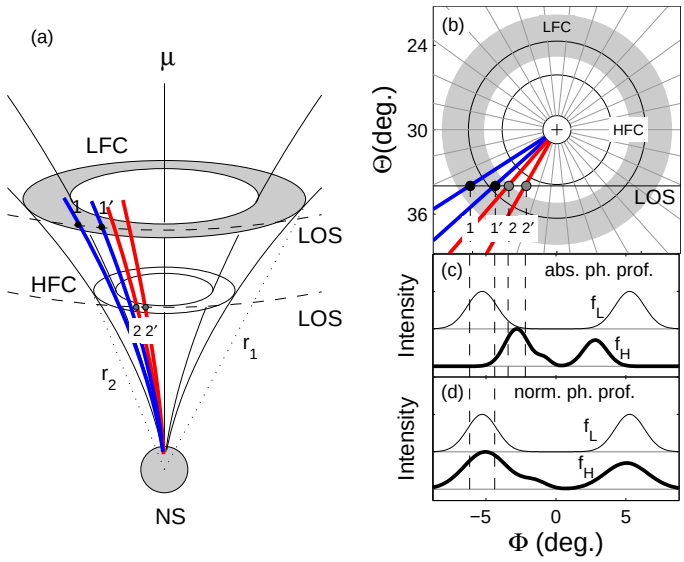

Fig. 2.30: Geometry of the radius-to-frequency-mapping model. Adopted from Chen & Wang [17].

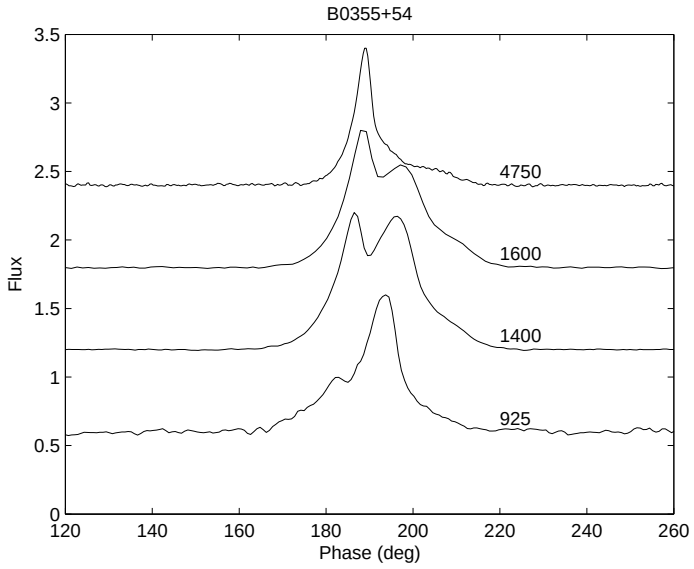

Fig. 2.31: Multi-frequency observations of PSR B0355+54. Adopted from Chen & Wang [17].

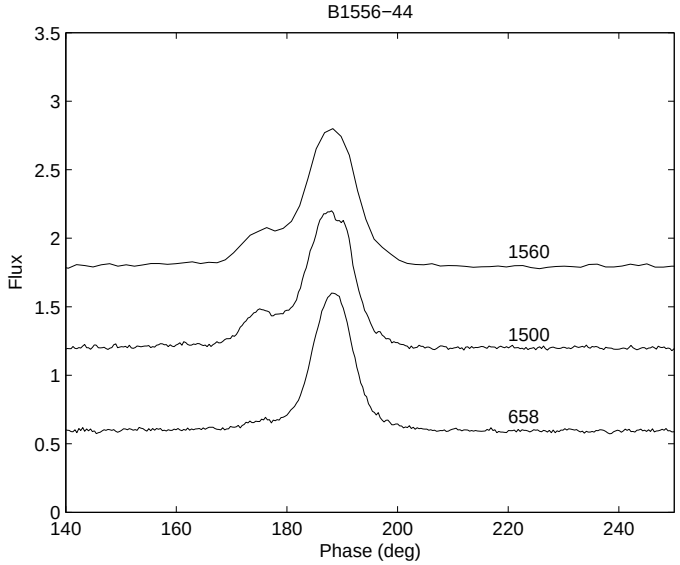

Fig. 2.32: Multi-frequency observations of PSR B1556-44. Adopted from Chen & Wang [17].

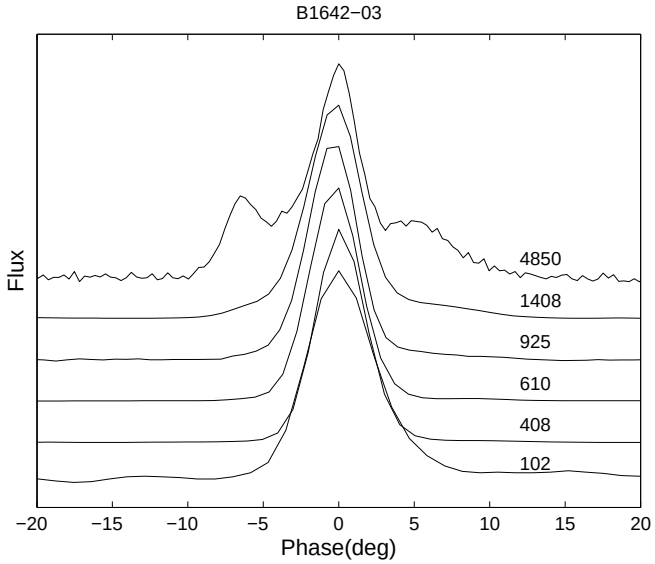

Fig. 2.33: Multi-frequency observations of PSR B1642-03. Adopted from Chen & Wang [17].

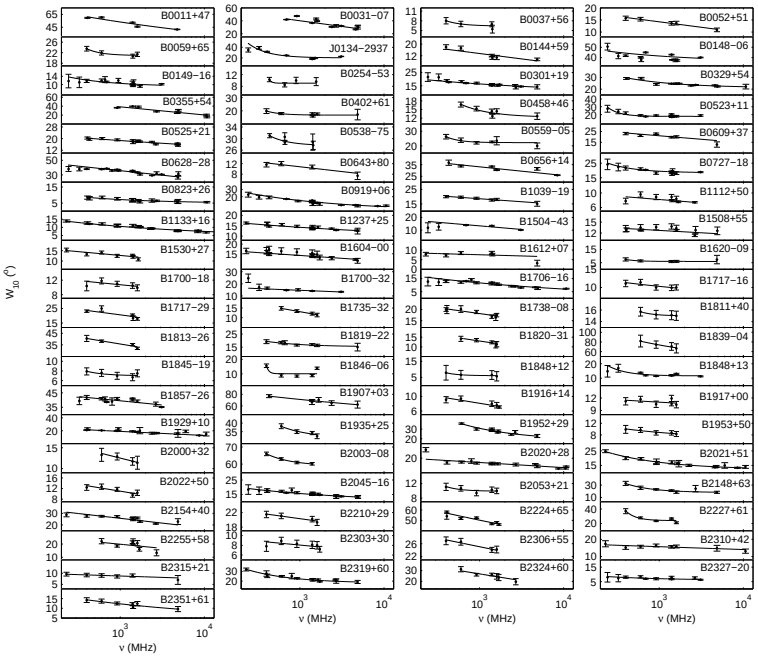

Fig. 2.34: Multi-frequency observations of several pulsars (Group A). Here W_{10} is the same as the opening angle of the radio pulse θ. Adopted from Chen & Wang [17].

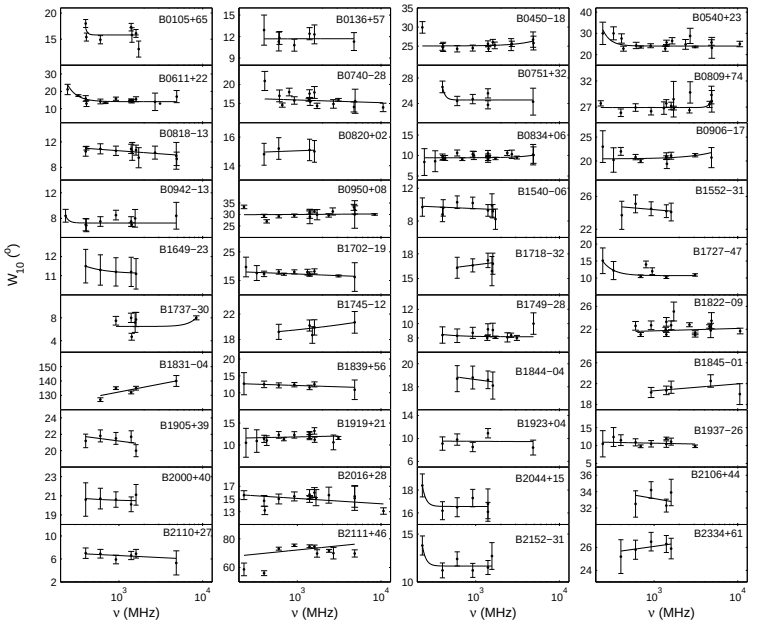

Fig. 2.35: Multi-frequency observations of several pulsars (Group B). Here W_{10} is the same as the opening angle of the radio pulse θ. Adopted from Chen & Wang [17].

Group A in this sample shows considerable pulse broadening towards the higher frequencies and group B shows marginal increases of the pulse width towards higher frequencies. The average Thorsett relationship is indicated on Fig.2.34 but marginally in Fig.2.35. Investigating the RFM model and implications thereof are of scientific importance towards the considerations of the studies of profile variability. Any future pulse variability studies can be centered around wide-band MeerKAT data that will automatically include the phenomena of pulsar profile-frequency evolution. PSR B0355+54 shows double peak structure evolution over 925 MHz to 4750 MHz; classically following the RFM model. However, PSR B1642-03 exhibits pulse profile evolution along the lines of profile component evolution from 102 MHz to 4850 MHz. PSR B0355+54 follows a similar profile evolution as exhibited by PSR J1326-5859 that is of interest for this study. According to Fig.2.30 and the use of the hollow cone model, we can see two emission heights (LFC and HFC); higher frequency observations will be probing the regions nearer to the surface of the pulsar and lower frequency observations will be higher up. The model is dependent on the Line of sight of the observer (reflects how the emission cone is cut).

In this chapter the reader was introduced to the basic radio and pulsar astronomy principles that cover measurable quantities, telescopes, radio sources in the local universe, energetics of pulsars and the magnetosphere of pulsars. In the next chapter the reader will be introduced to the principles that govern the process of pulsar timing and the applications thereof.

Chapter 3

Timing Pulsars

3.1 Methodology of timing pulsars

Pulsar timing is a method that debut in 1992 and was used specifically by Frail and Wolszczan to detect the first exoplanets, which orbit pulsars and change their timing properties in a periodic manner that can be predicted by applying the appropriate timing models and will produce periodic timing residuals. A year after that, in 1993, a Nobel Prize was awarded to Hulse and Taylor that proved indirectly the existence of GW with the help of the technique of pulsar timing (Hulse & Taylor [41]).

The technique of finding planets around pulsars also sets the stage for searching for other spin variations; in that the method consists of searching for variations in the time stamps of the light house pulses due to the perturbation of the motion of the pulsar produced by the orbiting planet. Wolszczan & Frail [97] used the 305-m Arecibo radio telescope to perform accurate timing on the millisecond pulsar PSR 1257+12 which is a 6.2 ms pulsar that is believed to be orbited by two Earth mass objects at a distance of a fraction of an astronomical unit, see Fig.3.1.

The methodology of timing pulsars are based on the use of a list of time of arrivals (TOA) associated with each pulse produced by the rotating neutron star that were obtained by radio observations (of which some examples will be discussed in the next few sections). The process of timing pulsars will be discussed further in this section and will follow closely what were discussed in Kraus [49], Camenzind [15], Condon [20] and Lorimer & Kramer [54]. The TOA is generated by correlating some fiducial point on the recorded pulse profile, that can theoretically be described as the point that coincides with the plane that can be mathematically constructed using the rotation and the magnetic axis and needs to be chosen consistently throughout the process of timing, to a stable profile. The stable profile of the pulsar is constructed by adding several thousand pulse profiles in order to create a stable reference point for the process of computing the TOA. It should be noted that standard pulse can

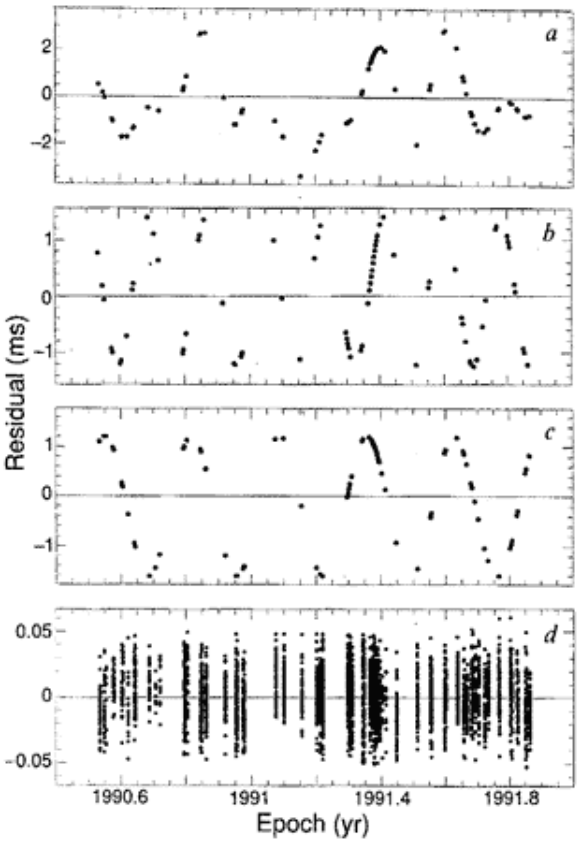

Fig. 3.1: Timing perturbations produced by each of the orbiting planets around PSR 1257+12, adopted from Wolszczan & Frail [97].

not consist of the addition of too few pulses, since there do exist evolution in the individual pulse profiles. The offset between these points can be added to a accurate reference point in time kept by masers to ultimately produce the TOA. Associated with these TOA are instrumental uncertainties that need to be taken into account when used for the pulsar timing purposes, i.e. there are uncertainties associated with the time stamps of pulses that is a superposition of instrumental uncertainties.

Depending on the sensitivity and processing back-end of the radio telescope, the TOA can either be determined in real-time or via post-processing. The process of gathering TOA can be performed in the time domain or the frequency domain with some pre-determined accuracy. The accuracy of the TOA are based on the pulse width and the signal-to-noise-ratio of the observation, i.e.

$$\sigma_{TOA} = \frac{W}{S/N}. \tag{3.1}$$

To analyze the list of TOA we first need to find a mechanism that describes the pulsar rotation and rotational evolution, this is essentially the spin-down model of pulsars.

If the spin frequency of the pulsar is the rate of change of the pulse number N (see Lorimer & Kramer [54]), then the pulse number will also evolve as the spin-frequency:

$$N = N_0 + \nu_0(t - t_0) + \frac{1}{2}\dot{\nu}_0(t - t_0)^2 + \frac{1}{6}\ddot{\nu}_0(t - t_0)^3..., \tag{3.2}$$

with N_0 being the pulse number at epoch t_0 and will typically be an integer. If the starting point t_0 coincides with the observatory time stamp of the pulse, together with the assumption that $\dot{\nu}$ of the pulsar is accurately known through the process of high precision timing, then the pulse train can be predicted by integer multiples of N_0.

The observatory time stamps of the recorded pulses (topocentric TOA) are maintained by hydrogen masers at the observatory. The time stamps are compared to Coordinated Universal Time (UTC) by using Global Positioning Systems (GPS). UTC is always an integral number of seconds from International Atomic Time (TAI) that is kept by atomic clocks. Lastly, astronomers introduce occasional leap seconds to TAI and convert this time standard to Terrestrial Dynamic Time (TT) via TT = TAI + 32.184s (see Appendix A2.3 of Burke [14]) and represents the idealistic time stamp of the pulse at the observatory (see Lorimer & Kramer [54] and Camenzind [15]).

Before we can analyze pulsar timing data the topocentric TOA (time stamp that is recorded at the observatory) need to be converted to barycentric TOA, i.e. we need to correct for time delays caused by the planets, the Sun and the earth's orbit in our solar system (see e.g. Camenzind [15]):

$$t_{\mathrm{bary}} = t_{\mathrm{top}} + t_{corr} - t_{\mathrm{DM}} + \Delta(\mathrm{R}, E, \mathrm{S}) \tag{3.3}$$

where $(t_{\mathrm{top}} + t_{\mathrm{corr}})$ is the corrected observatory time stamp of the pulse, t_{DM} is the dispersive delay due to the ISM and $\Delta(R, E, S)$ represents the delay contribution

due to Roemer effects, Shapiro effects and the Einstein delay for both the solar systems and the presence of a binary companion. The Roemer delay is the classical light-travel time between the observatory and the solar system barycenter. The Shapiro correction accounts for the time delay induced by the gravitational curvature of the masses in the solar system. The Einstein delay describes the additional delay induced by the motion of the Earth in the Solar System. When performing barycentric corrections of time stamps on satellites, an additional correction term needs to be included for the orbit of the satellite around the earth.

Via the process of minimizing the χ^2 value, the initial timing parameters can be systematically estimated through a process of trail and error (see equation 8.5 in Lorimer & Kramer [54]):

$$\chi^2 = \sum_i \left(\frac{N(t_i) - n_i}{\sigma_i} \right)^2, \tag{3.4}$$

where σ_i represents the uncertainty in the TOA due to instrumental limitations and $N(t_i) - n_i$ represents the offset between the predicted pulse number at TOA $= t_i$ and the nearest integer to the predicted pulse number (this difference needs to be minimized in order to retrieve best-fit timing parameters). Idealistically the χ^2 method can be used to obtain a phase-connected solution that can account for every single pulse observed from the pulsar. In reality this process is performed using a small list of TOA that are closely spaced in the time domain to infer a preliminary set of parameters for the spin-down model of the particular pulsar. Finally, the residuals are formed from the difference of the observed and the predicted TOA. These non-zero residuals can be used to investigate effects that are either contributed by the pulsar itself, the surrounding local environment of the pulsar or un-modelled effects caused by the interstellar medium. In summary, the pulsar astronomer start with a few TOA and estimate primarily parameters such as spin period and spin-frequency using the χ^2-method, as more TOA are recorded, the astronomer can determine the full coherent timing solution of the particular pulsar.

Scientific investigations (such as strong gravity tests) that are derived from pulsar timing, rely on how accurate the spin frequency of the pulsar can be determined. The change in the spin frequency of the pulsar is $\Delta f \propto \Delta\phi$ where the phase is measured in rotations. Thus, the accuracy of the frequency can be determined by how accurate we can measure any change in the phase over long time periods (could be up to decades as part of long-term observational pulsar programs). To illustrate the

power of pulsar timing, the reader is introduced to the original millisecond pulsar, PSR B1937+21 (also an occasional bright pulse emitter) which has a pulse period of P≈ 0.00156 s and a TOA accuracy of $\sigma_{\rm TOA} \approx 1\ \mu$s which translate to a phase error of $\Delta\phi \approx 6 \times 10^{-4}$ rotations (see Chapter 6 of Condon [20]). This pulsar has been timed for more then 25 years, thus

$$\Delta f \approx \frac{\Delta\phi}{\Delta T} \approx 8 \times 10^{-13}\text{Hz}. \tag{3.5}$$

This is of the same order of the time that a IBM Silicon-Germanium transistor executes one switching machine cycle. In the next section the signal path of the observed voltage through the radio telescope will be discussed.

3.2 Timing pulsars with radio pulses

3.2.1 Hardware of pulsar astronomy

It is no wonder that the backbone of pulsar astronomy is based on the development and innovation of electronic systems that can record and analyze individual pulses that are produced by pulsars in real-time and with exceptional accuracy. The above mentioned methodology surrounding the timing of pulsars, requires leading electronic system development. Great technical challenges surround the detection-speed, accuracy and storage of individual pulses produced by many different classes of pulsars. Modern pulsar astronomy is based on the principle of coherent signal processing, i.e. retrieving the phases of the input signal via Fourier transformations and altering these phases to correct for certain systematic effects. Most of the hardware and storage requirements are of the utmost importance during this step of coherent signal processing.

Typically the signal arrives at the pulsar back-end of the telescope in the form of an analog signal, this signal gets sampled via an analog-to-digital converter (or ADC). The ADC samples and digitizes the signal and assembles it in the form of a data stream that gets passed to the field-programmable-gate-arrays (FPGAs) where the input stream gets converted to the Fourier domain. This step is crucial in the field of pulsar astronomy since it reveals systematic effects in the bandwidth of data that are due to the ISM or the instrument itself. Once the bandwidth of data is de-dispersed and cleaned of Radio Frequency Interference (RFI), the data are stored in structures containing the corrected phases and amplitudes of the sampled data stream. This raw structure resembles a base-band recording that is the starting

point of real-time or post-processing analyses. The process of base-band recording, de-dispersing, calibration and folding will be discussed in the following sections and will be based on the discussion found in Lorimer & Kramer [54].

Base-band recording

In order to manipulate the phases and amplitudes of the observed complex voltage $V_{\rm complex}(t)$ centered around some frequency f_0, we make use of a base-band recording. In order to access the amplitude and the phases of $V_{\rm complex}(t)$ we down-convert the signal by mixing it with some local oscillator with frequency f_{LO} and by applying a low-pass filter to remove the frequencies $f_0 + f_{\rm LO}$ and $f_0 - f_{\rm LO}$. If we choose $f_{\rm LO} = f_0$ we create a base-band with size of $\left[-\frac{\Delta f}{2}, \frac{\Delta f}{2}\right]$ centered around f_0. The digitized real and imaginary parts of $V_{\rm complex}(t)$ become:

$$\mathrm{I}(t) = \frac{1}{2} a(t) cos(\phi(t)) \tag{3.6}$$

$$\mathrm{Q}(t) = -\frac{1}{2} a(t) sin(\phi(t)). \tag{3.7}$$

The signals $\mathrm{I}(t)$ and $\mathrm{Q}(t)$ provide access the to amplitude and phase of signal. The signals $\mathrm{I}(t)$ and $\mathrm{Q}(t)$ are sampled at Nyquist-rate, that is $2\Delta f$. To extract the phases for polarimetry we perform an additional Fourier transform that, together with base-band recording, lead to complex sampling rather than real sampling. This base-band recording of the signal $V_{\rm complex}(t)$ gets transformed to the Fourier domain can manipulated by filters and RFI rejection algorithms. The process of coherent de-dispersion will be discussed in the next subsection.

De-dispersion

The process of de-dispersion can either be done in post-processing (i.e. folding the data and removing dispersion by hand) or by using the process of coherent dispersion (Hankins & Rickett [36]). Coherent de-dispersion uses the fact that the effects produced by the instellar medium (ISM) on the signal can be modelled as a filter, this is:

$$V_{\rm pulsar}(f) \rightarrow H_{\rm ISM} \rightarrow V(f), \tag{3.8}$$

where $V_{\rm pulsar}(f)$ represents the pulsar signal in the Fourier domain and $H_{\rm ISM}$ changes $V_{\rm pulsar}(f)$ in some systematic way that can be modelled.

Idealistically the inverse of $H_{\rm ISM}$ needs to found and applied to the observed signal in the Fourier domain, this is:

$$V(f) = V_{\rm pulsar}(f)H^{-1}(f_0 + f), \tag{3.9}$$

where $H(f_0 + f)$ is the transfer function and $V(f)$ represents the corrected pulse train observed from the pulsar.

$$H(f + f_0) = \exp\left(\frac{i2\pi D}{(f + f_0)f_0^2}{\rm DM}f^2\right), \tag{3.10}$$

where $D = 4.148808 \times 10^9$ cm^3 pc $^{-1}$ MHz, DM corresponds to the dispersion measure of the pulsars in units of cm^{-3} pc (De & Gupta [25]).

The transfer function $H_{\rm ISM}$ reacts sensitively to the dispersion measure of a particular pulsar in the sense that in the low frequency regime the total delay induced by dispersive effects are more than the delays induced in the higher frequency domains. This DM-dependent characteristic of the transfer function $H_{\rm ISM}$ limits the particular back-end of the radio telescope to a certain cut-off DM. The transfer function of the ISM is also sensitive to the distance to the source.

Polarimetry and calibration

The process of coherent-dispersion is based on the sampling of complex voltages and all four Stokes parameters are available. After sampling two orthogonal signal feeds ($\mathcal{X}$ and $\mathcal{Y}$), the combined Stokes vector, defined earlier becomes

$$
\begin{aligned}
I &= \langle \mathcal{X}^2 \rangle + \langle \mathcal{Y}^2 \rangle && (3.11)\\
Q &= \langle \mathcal{X}^2 \rangle - \langle \mathcal{Y}^2 \rangle && (3.12)\\
U &= \langle 2\mathrm{Re}(\mathcal{X}\mathcal{Y}^*) \rangle && (3.13)\\
V &= \langle 2\mathrm{Im}(\mathcal{X}\mathcal{Y}^*) \rangle, && (3.14)
\end{aligned}
$$

which for left/right-hand circular polarization, reduces to:

$$
\begin{aligned}
I &= \langle \mathcal{L}^2 \rangle + \langle \mathcal{R}^2 \rangle && (3.15)\\
Q &= \langle \mathcal{L}^2 \rangle - \langle \mathcal{R}^2 \rangle && (3.16)\\
U &= \langle 2\mathrm{Re}(\mathcal{L}\mathcal{R}^*) \rangle && (3.17)\\
V &= \langle 2\mathrm{Im}(\mathcal{L}\mathcal{R}^*) \rangle. && (3.18)
\end{aligned}
$$

Associated with the observed total intensity of the pulsar emission, is the degree of linear/circular polarization (measured with the above mentioned method). However, to insure that the polarization data resemble an accurate degree of polarization we need to calibrate the polarization data as well. This is done by the same process in Fourier space as what was done previously for the de-dispersion process. The instrumental effects need to be tracked that could change the original polarization of the data. If these effects are corrected (called the Mueller matrix) in the Fourier domain then a transfer function (similar to the de-dispersion filter) can be constructed in the following way, see e.g. (Lorimer & Kramer [54])

$$
\mathcal{M} = \mathcal{M}_{\mathrm{amp}} + \mathcal{M}_{\mathrm{CC}} + \mathcal{M}_{\mathrm{Feed}} + \mathcal{M}_{\mathrm{PA}}, \qquad (3.19)
$$

where $\mathcal{M}_{\mathrm{amp}}$ represents the effect of different amplification signal paths that induce extra phase changes in the original signal, $\mathcal{M}_{\mathrm{CC}}$ is the effect of cross coupling the two different probes, $\mathcal{M}_{\mathrm{Feed}}$ corrects for the use of linear or circular feeds and $\mathcal{M}_{\mathrm{PA}}$ corrects for the 2PA phase change due to phase plane rotation of the parallactic

angle (PA).

The Mueller matrix can then be used to obtain the original signal as recorded by the telescope, this is

$$\mathcal{S}_{\text{measured}} = \mathcal{M} \times \mathcal{S}_{\text{initial}}. \tag{3.20}$$

This calibration process is done with a combination of telescope hardware and pulsar analysis software.

Modern hardware

The extension of radio telescopes that enables pulsar astronomy is based on modern coherent de-dispersion hardware and software, see e.g. (De & Gupta [26]) and (Naidu et al. [62]) for complete summaries of both the hardware and software capabilities of modern pulsar astronomy. This subsection will provide a basic signal flow associated with modern pulsar-backends.

Pulsar astronomy relies on the process of base-band recording and coherent de-dispersion, that is, recording of the full-bandwidth signal (or base-band) and performing all necessary signal processing in the Fourier domain. Once the analog signal is converted to a digital signal, that is: the continuous signal was converted to discrete values, what we are left with is a data stream of sampled values in the time domain of the EM wave. This list of discrete samples are passed to the signal processing block that converts the list to the Fourier domain. Thus, we are left with a list of phases and amplitudes to manipulate and correct according to our pulsar model. We represent this list as:

$$\textit{Input Stream} \rightarrow \textit{channeled} \rightarrow [\phi_0, \phi_1, ..., \phi_N]. \tag{3.21}$$

To retain the original resolution of the data the Fourier process depends on data blocks with size N to insure Nyquist sampling at twice the bandwidth. Most the manipulation of the observed phases can be done in a parallel way with a combination of processing units that include: FPGAs, CPUs and GPUs. The FPGAs are the Fourier transformation workhorses, CPUs act as the control environment and the

GPUs act as the workhorses for the filter processing.

3.2.2 Observing known pulsars

Once the output stream of voltages is de-dispersed, that is, the sampled phases were corrected for the effects of the ISM and instrumental effects, then known pulsars or new pulsars can be searched for in the base-band recording data. This subsection will outline the process of observing known pulsars and will form the main technical methodology of the timing noise analysis of a known pulsar which will be explained in the proceeding chapters.

As stated in the chapter of the basic principles of pulsar astronomy, telescopes are sensitivity limited due to the ever-present instrumental noise generated by the telescope. Generally, pulsars are weak radio sources (except for young energetic pulsars such as Vela) and this characteristic leads us to the process of folding the data with a known period. Folding is analogous to phase stacking the signal to increase the S/N. The folding process is done with respect to a known pulsar period and can be executed in phase space for a specific integration time. What are left after this process is a list of integrated pulses which can be analyzed and accessed for further manipulation.

Associated with known pulsars are high precision ephemerides that can be used to determine the phase of the observational epoch. A list of phases per epoch can be generated and used for timing purposes (see the previously mentioned methodology about the timing of pulsars). The TOA that are produced have errors of magnitude:

$$\sigma_{\mathrm{TOA}} \approx \frac{\mathrm{W}}{\mathrm{S/N}} \tag{3.22}$$

When a known pulsar is discovered its period, dispersion and position can be roughly calculated and improved as more and more pulses are recorded. The pulsar ephemeris can be kept updated continuously by frequent observations. To retrieve accurate recorded flux densities we use noise diodes as calibration sources as mentioned in chapter two. This can be done in several ways: switching the diode between on and off states during the observations or by simulating a pulsar with a switching diode and folding the data to detect the calibrated pulses.

Hydrogen masers are used to determine the observatory time tag for every TOA. As

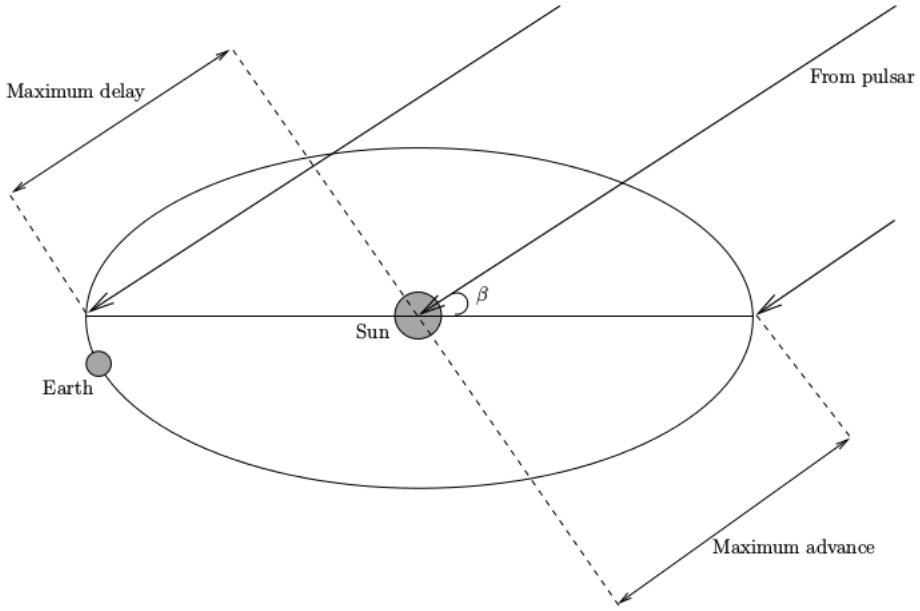

Fig. 3.2: Basic geometric setup for determining the Roemer delay. Adopted from the 2004 version of Lorimer & Kramer [54].

mentioned in the methodology of timing pulsars, we need to apply clock, frequency and barycentric corrections to the TOA before any analysis can be performed. To retrieve the position (astronomic data) of the pulsar relies on the observation of the annual variation in the TOA as predicted by the Roemer delay, see page 227 of Condon [20] and Fig.3.2 for the geometrical setup.

$$\Delta_{R\odot} = A\cos(\omega t - \lambda)\cos\beta, \tag{3.23}$$

where A, ω, λ and β represent the light travel time from the Earth to the Sun, angular velocity of the Earth around the Sun, the ecliptic longitude of the pulsar and the ecliptic latitude of the pulsar. This variation induced in the TOA has a maximum amplitude of:

$$\Delta_{R\odot} \approx 500\,\mathrm{s} \times \cos\beta, \tag{3.24}$$

where β represents the ecliptic latitude and greatly effects the accuracy of the distance, however, the accuracy of the pulsar's distance can be improved by simple interferometric observations. Lastly, it is note that the timing residuals can suffer

from unforeseen effects such as the presence of the relative motion of the pulsar (as predicted by pulsar-supernova kicks, see Lai, Chernoff & Cordes [50]) or the timing parallax that is caused by the orbit of the earth around the sun, specifically seen in nearby pulsars. However, most of these corrections, including the presence of a binary companion, can now be corrected via packages such as *Tempo2*, see www.atnf.csiro.au.

In the next section discussing the pulsar's magnetosphere we introduce the reader to different emission regions (e.g. polar cap, outer cap and striped wind) and different energies of pulsed emission. There exist fundamental synergies between radio, X-ray and gamma-ray pulsed emission and all three types of pulsed emission can be used for timing purposes. It is for this reason that the timing procedure for pulsars in the gamma ray regime was investigated in the next section to introduce the reader to pulsed emission from other regions in the magnetosphere besides emission from the polar cap. It needs to be emphasized to the reader that the timing process within different energies are different in the sense of timing accuracy and instrumental procedure.

3.3 Timing pulsars with gamma rays

Obtaining TOA with satellites are fundamentally different from the recording process using radio telescopes. As mentioned in the previous section; TOA are formed by matching the observed radio pulse with a well-known pulse template. The resulting radio pulse profiles are governed by Gaussian statistics. The TOA that are observed via satellites such as the Fermi gamma-ray telescope, are formed by observing single photons stacked on the ever-present background noise and require Poisson statistics and Bayesian analysis. A single TOA produced by a gamma-ray pulsar can be due to many hours of observation, the resolution associated with the timing procedure becomes coarse (Kerr et al. [48]).

The Large Array Telescope (LAT) on board the Fermi satellite opened a new window on the Universe for energies ranging from 200MeV to 300GeV. As an example to illustrate pulsar timing of a gamma-ray pulsar, the Vela pulsar was chosen. The data extraction process was done for Vela using both the Fermi tools and the python package Enrico. Both these tool sets are open source and can be downloaded from `https://github.com/gammapy/enrico` and `https://fermi.gsfc.nasa.gov`. The applications and use of these tools could also be applied to the search for AGNs and blazars.

The LAT Data set, which was released one year after the Fermi launch, can be

analyzed using the Fermi Science Tools using a series of command line options. However it quickly becomes evident that the Science Tools lack very important features such as light curve production and are very technical to configure for the use of several computer CPUs. It is for this reason that the data are analyzed using both the Science (Fermi) Tools and a python package called Enrico (Sanchez & Deil [82]). These tools will be used in the analysis of Vela which could be found in the Fermi two year catalog (see `http://fermi.gsfc.nasa.gov/ssc/data/access/lat/2yr_catalog/`).

3.3.1 Software setup

Detailed installation instructions for both the Science Tools and Enrico (see Fig.3.3) can be found at `http://enrico.readthedocs.org` and `http://fermi.gsfc.nasa.gov/ssc/data/analysis/software/`. There are several methods to install these software packages, but the recommended method entails the installation of the Fermi tools through the download of the source code. Compiling the source code will insure that the workstation will be equipped with all the correct mandatory libraries. Installing Enrico is the simplest part since all that needs to be done is to retrieve the binary distribution from the web-site (a binary distribution of a software package is a folder that contains the pre-compiled software). To manipulate fits file one also needs to install HEASOFT from the Fermi site (see `http://heasarc.nasa.gov/lheasoft/`). This software package allows the user the access fits files, view or plot certain columns and join several photon data files together, which is possible since the fits files that are retrieved from the Fermi data server are decomposed into smaller fit files.

3.3.2 Vela Pulsar

For the Fermi analysis of the Vela pulsar (Abdo et al. [1]) a photon data set from dates MET=239557417 to MET=240105600 between the energy range 3 MeV to 3000 MeV was used. This data, or any other data set, can be retrieved from the Fermi data server.

Once the chosen photon data set is retrieved from the server, the first step will be to perform a selection of what photons to use in the data set, thus several compulsory steps will have to be performed. Assuming that the photon data file is called `Vela_PH00.fits` and that the space craft file is called `Vela_SC00.fits`. The outputs of the commands will only be showed once and neglected for the rest of the section, starting with:

```
> gselect evclass = 2 (this makes a sub selection)
```

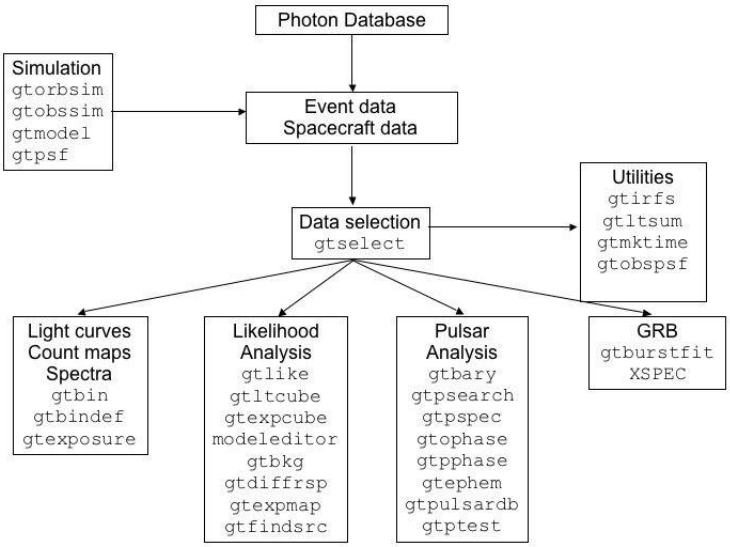

Fig. 3.3: Hierarchy of the Science Tool set; we will be implementing tools for Pulsar extraction, but the global method remains identical for Blazars and AGNs. This tool set will also form the basis of the python package Enrico

```
Input FT1 file[]  Vela_PH00.fits
Output FT1 file[] Vela.fits
lower energy limit (MeV) (0:) [] 100
upper energy limit (MeV) (0:) [] 300000
maximum zenith angle value (degrees)
(0:180) [] 100


> gtmktime (This applies the Space
craft corrections)

Spacecraft data file[] Vela_SC00.fits
Filter expression[] (DATA_QUAL>0)
&&(LAT_CONFIG==1)
Apply ROI-based zenith angle cut[] yes
Event data file[] Vela.fits
Output event file name[] Vela_gtis.fits


> gtbin (This produces a counts map)
```

```
Type of output file
(CCUBE|CMAP|LC|PHA1|PHA2) [CMAP]
Event data file name[] Vela_gtis.fits
Output file name[] Vela_cmap.fits
Spacecraft data file name[] Vela_SC00.fits
Size of the X axis in pixels[] 300
Size of the Y axis in pixels[] 300
Image scale (in degrees/pixel)[] 0.1
Coordinate system  (CEL|GAL) [CEL]
First coordinate of image center[]
128.8391
Second coordinate of image center[]
-45.1792
Rotation angle of image axis, in degrees
[0]
Projection method:[] CAR
```

The user can also download the emphemeris of the Vela pulsar from `http://fermi.gsfc.nasa.gov/ssc/data/access/lat/ephems/`. This file could be used to assign phases to each photon in the data set. This could be done by using

```
> gtpphase

Event data file name[]
Geminga_gtis.fits
Spacecraft data file name[]
Vela_SC00.fits
Pulsar ephemerides name[]
Vela_ephemeris.fits
Pulsar name[] Vela
How will spin ephemeris be specified?
[DB]
```

to obtain general information regarding any Fermi tool or syntax description of the tools. The output produced by the command of `gtphase` will be stored in the `Vela_gtis.fits` file as an extra column. These photon phases can be plotted from the fits file, see Fig.3.4.

The process of classifying the object as a pulsar is simplified if the user knows the ephemeris of the pulsar, if the pulsar ephemeris is not known then the process becomes more involved (this is also true for extracting blazars and AGNs from the

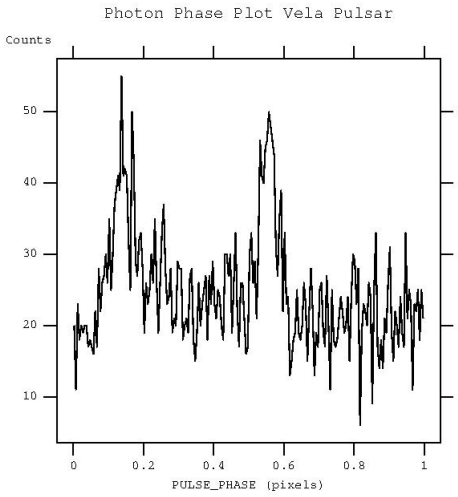

Fig. 3.4: Folded light curve of the Vela pulsar, clearly showing two peaks (F_1 and F_2) , an off-pulse phase (between F_1 and F_2) and a bridge emission phase after F_2.

Fermi data). If it is not clearly known what type of point source the data represents, then the user proceeds with the process of likelihood analysis. This analysis allows the user to fit a chosen model to the Spectral Energy Distribution (SED) of the data to the best statistical significance. The likelihood analysis can be done via a Binned or Unbinned analysis, the Unbinned analysis is the preferred analysis method of Fermi data (of one uses large data sets). This analysis can be done by first using the command:

```
> gtltcube

Event data file[]
Vela_gti.fits
Spacecraft data file[]
Vela_SC00.fits
Output file[]
Vela_ltcube.fits
Step size in cos(theta)[]
0.025
Pixel size (degrees)[] 1
```

These commands create a livetime cube, which is a HealPix table, covering the full sky, of the integrated livetime as a function of inclination with respect to the LAT

z-axis. One of the last steps in the likelihood process is that of creating a exposure map, this is done by the command:

```
> gtexpmap

Event data file[]
Vela_gti.fits
Spacecraft data file[]
Vela_SC00.fits
Exposure hypercube file[]
Vela_ltcube.fits
output file name[]
Vela_expmap.fits
Response functions[] P7SOURCE_V6
Radius of the source region[]
30
Number of longitude points []
120
Number of latitude points  []
120
Number of energies (2:100) []
20
```

Lastly, the user must create a model file that assigns to each source in the region of interest (ROI) a spectral model, this model could be straight forward power laws (for AGNs or diffuse backgrounds) or more specifically power laws with exponential cut-offs (for gamma ray pulsars). These models could be designed directly by using the prescribed models on the Fermi site (`http://fermi.gsfc.nasa.gov/ssc/data/analysis/scitools/xml_model_defs.html`) and just pasting it into a file with a `.xml` extension using `gedit`. At this stage the user must download the latest galactic and extra galactic models from the site `ov/ssc/data/access/lat/BackgroundModels.html`, these files will be used in the likelihood analysis to fit spectral models to the diffuse sources (note that these sources are also specified in the `.xml` file)

```
> gtlike plot=yes sfile=Vela_output_model.xml

Statistic to use (BINNED|UNBINNED) [] UNBINNED
Spacecraft file[] Vela_SC00.fits
Event file[] Vela_events_gti.fits
Unbinned exposure map[] Vela_expmap.fits
```

```
Exposure hypercube file[] Vela_ltcube.fits
Source model file[] 3C279_input_model.xml
Response functions to use[] P7SOURCE_V6
Optimizer  [] NEWMINUIT
```

This command will produce the Spectral Energy Distribution (SED) of the Vela pulsar, see Fig.3.5, Fig.3.6 and Fig.3.7 for different fitted models.

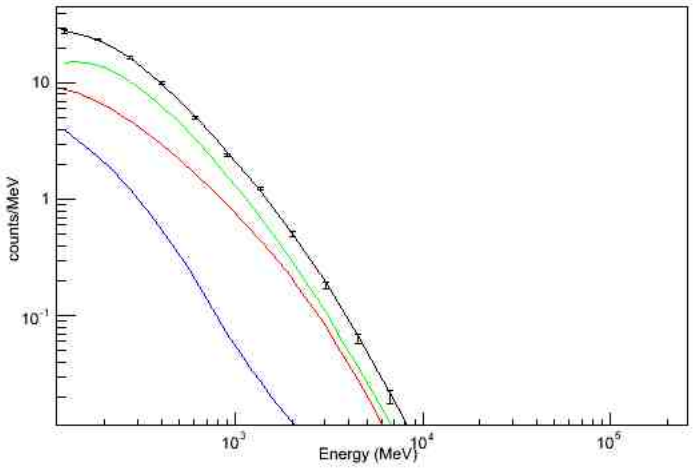

Fig. 3.5: Fitted SED of the Vela Pulsar fitted with a clear power law with exponential cut-off.

The user could also use a encapsulated python package (called Enrico) that contains all the steps mentioned above in a sort of an automated package. This software package is very fast and produces admirable publishable figures. The user can consult the site `http://enrico.readthedocs.org` for more information and installation guides. Within the same working folder (that contains all the data files, spacecraft files and diffuse models) the user can initialize the Enrico package by following a few simple commands from (Sanchez & Deil [82]); first create a `config` file that contains all the time-cut and energy range information:

```
>enrico_config Vela.conf
```

The user must answer some simple questions regarding the data files and energy ranges for the pulsar photon data that was downloaded by hand (these data files are located in your working folder). The package reads the second year Fermi catalog and automatically creates a `.xml` file for the chosen point sources:

```
>enrico_xml Vela.conf
```

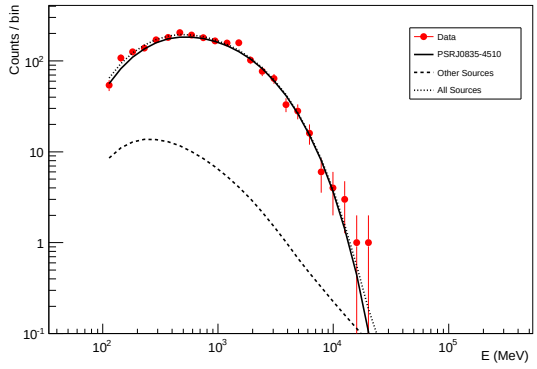

Fig. 3.6: Fitted SED of the Vela Pulsar fitted with a clear power law with exponential cut-off.

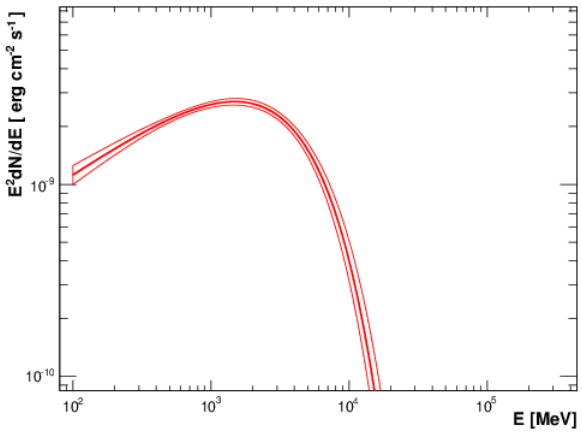

Fig. 3.7: Just the fitted SED of the Vela Pulsar fitted with a clear power law with exponential cut-off.

The user can now relate this `.xml` produced by Enrico with the `.xml` file produced in the previous section. These files may only be different in the sense that the number of sources included in the ROI may be be different, but both files will contain the primary source and the diffuse sources. The user could use Enrico the produce a SED for Vela by using the command:

```
>enrico_sed Vela.conf
```

3.3.3 Ties between gamma-ray and radio pulses

Rookyard et al. [79] investigated the relationship between gamma ray detected pulsars (GDP) and non gamma ray detected pulsars (NGDP) and found that the NGDP have wider radio pulse profiles with a dependency on the rate of energy loss and the

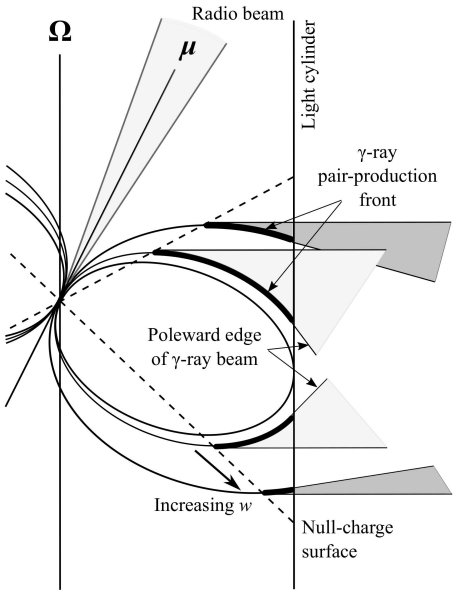

Fig. 3.8: Geometry associated with emission regions, divided up into the radio emission region (polar cap,narrow beam) and outer-gap emission region of which the gamma-rays are beamed along tangents to the gamma ray pair-production front. This illustration shows the Goldreich-Julian null-surface, together with the misaligned magnetic and rotation axis. Figure adopted from Rookyard et al. [79].

peak separation of the gamma ray light curve. The authors propose that their selection of pulsars form a single population of pulsars of which their gamma ray detectability are based on their total spin-down power output and viewing angle towards the "light house" and that their results quantitatively justify the current radio and outer-magnetospheric gamma-ray emission models, see Fig.3.8.

They selected a sample of young energetic pulsars that excluded millisecond pulsars and of which the radio profiles were measured at a single frequency of 1400 MHz to prevent profile width changes with frequency. The authors used this sample of pulsars to investigate the correlation between the radio profile width (Width at ten percent intensity, W_{10}, in degrees), the separation between the two main gamma ray peaks of the light-curve and the spin-down power of the pulsar, see Fig.3.9 and Fig.3.10 for visual representation of the relationship between the pulse width and the spin-down energy ($\dot{E}$) and the pulsar peak separation.

The correlations described above can be explained by smaller inclination angles (a small inclination angle can produce a wide profile), higher emission heights, a large ratio between size of the emission region and dipolar open field region or different impact parameters. The width-$\dot{E}$ correlation suggests that current models are realistic and the interplay between radio and gamma ray timing will play a significant

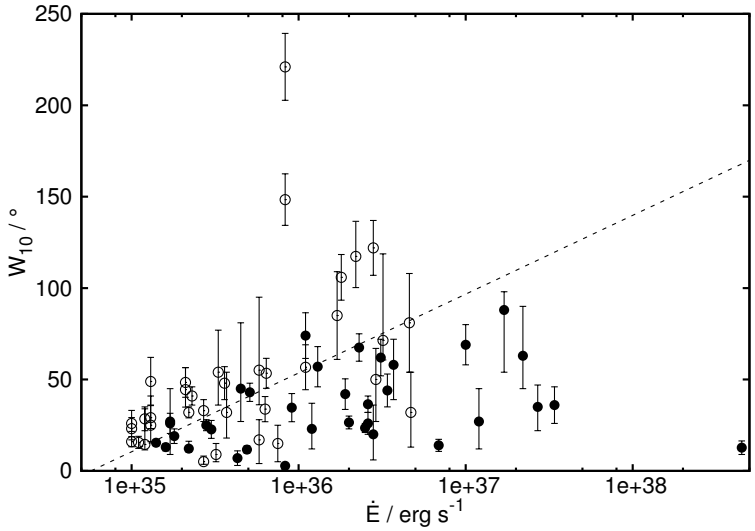

Fig. 3.9: Correlation of radio profile as a function of the pulsar's $\dot{E}$. Adopted from Rookyard et al. [79]. Here the empty and filled circles represent the millisecond and the normal pulsar population.

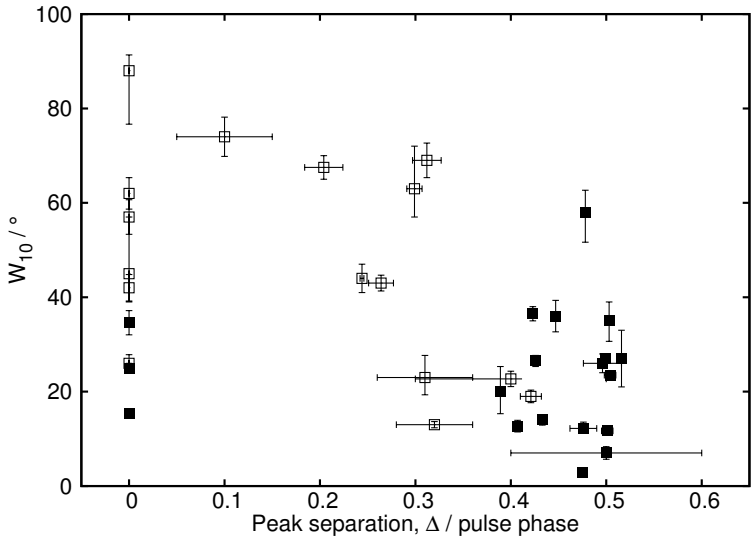

Fig. 3.10: Correlation of radio profile as a function of the pulsar's gamma ray peak separation. Adopted from Rookyard et al. [79]. Here the empty and filled circles represent the millisecond and the normal pulsar population.

role in the near future as more sensitive telescopes come online. The science sector created by combining radio observations with gamma ray observations of pulsars, is proving to be fruitful in the sense that combined emission models are now being tested with the aid of more and more gamma ray pulsars being detected with Fermi. Pétri [74] constructed a combined model that includes both the polar cap model and the striped wind model in one broadband emission model and can explain the time lag between the light curves. The latter mentioned model combines the Compton radiation in the wind model with a basic polar cap model along and around magnetic axis and can explain the observed gamma-ray and radio correlation. According to their composite model the radio emission is produced at lower altitudes closer to the cap, and gamma ray emission is produced just outside the light cylinder.

In the next chapter the reader will be introduced to the phenomena of timing noise, i.e. the non-zero timing noise residuals that can be observed in some pulsars over decades, and the analysis tools thereof.

Chapter 4

Timing noise

The main aim of pulsar timing is to account for every turn of a pulsar, ultimately enabling astronomers to use pulsars as stable clocks. However, not all pulsars can be considered as stable clocks, being unable to be reasonably fitted to the pulsar spin-down model. These unpredictable clock characteristics are broadly due to the clock mechanism itself, the mechanisms associated with the neutron star that produce the clock ticks (or observable pulses) in the magnetosphere, the interstellar medium (ISM) and some local reference clock effects (inaccuracies in the local observatory time stamps).

The "noise" contribution due to the clock mechanism (or pulsar) itself include glitches (sudden changes in the spin of the pulsar) and spin-noise (random variations in the spin-down parameters of the pulsar). The effect of several glitches on a neutron star can be visualized in Fig.4.1.

The "noise" induced by the ISM include frequency dependent dispersive delays of the pulse train, Faraday rotation (rotation of the polarization of the emitted electromagnetic pulse propagating along a magnetic field) and scattering (smearing of the pulse) due to irregularities or dense patches in the ISM.

The ISM smears the pulse train analogous to the well-known pulse anti-smearing filters that are used in the telecommunications industry to change the input signal systematically to produce an output that can be described as $Y = HX$, where H is called the transfer function that changes the signal in some mathematically described way. The transfer function for the ISM can be written as

$$H_{\mathrm{ISM}} = \exp \frac{2\pi D D_m (f - f_0)^2}{f f_0^2}, \tag{4.1}$$

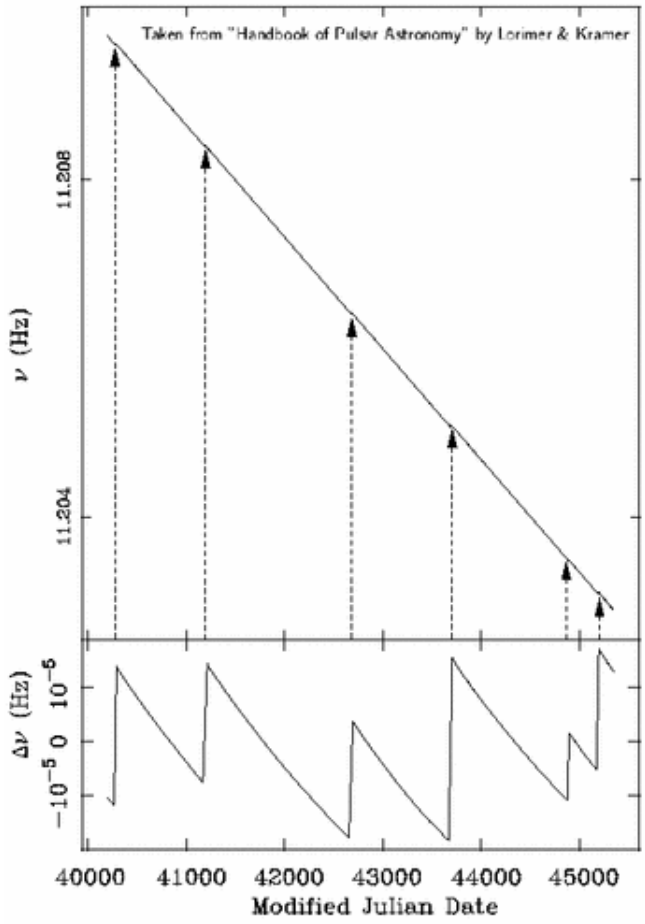

Fig. 4.1: Systematic glitches observed in the Vela pulsar over several years. The arrows indicates the glitch events that produce sudden changes in the spin-down rate. Followed by the glitch event is period of relaxation of spin-down rate of the neutron star, adopted from (Lorimer & Kramer [54]).

where D_m is the dispersion measure of the pulsar which represents the total electron density between the observer and the pulsar and is measured in cm^{-3} pc, $D = 4.148808 \times 10^9$ is a constant, f_0 is the lower edge of the observing band and f is the frequency at which the observation was performed (van Straten & Bailes [90]).

In the time domain it can be presented as a time delay induced between two neighboring frequency bins (f_1 and f_2), this is:

$$\delta t = 4.15 \times 10^6 (f_1^{-2} - f_2^{-2}) D_m, \tag{4.2}$$

where δt is dependent on the dispersion measure (D_m) and the frequency resolution of the observation ($f_1^{-2} - f_2^{-2}$). Additive to the "noise" reservoir are the dynamics of the mechanism that produces the clock ticks, changing the phase of some pulses, ultimately producing pulse variations both in frequency and time. Single pulse variations can be visualized by Fig.4.2.

Lastly, the local clock effects include the "noise" contribution from the ionosphere (which influences radio propagation), polarization instrumental cross-coupling (changes in the amplitude and phase of the signal produced by the superposition of the antenna-patterns), radiometer thermal noise of the system's electronics and the process of converting the times of arrival (TOA) to the solar system barycenter. The process of converting to the barycentric TOAs depends heavily on the chosen solar system ephemerides, thus inaccuracies in the chosen ephemeris lead to observed timing inaccuracies (see e.g. Lorimer & Kramer [54]).

Pulsars that exhibit dynamical features in their spin-down and emission properties with cycle times between seconds, days or even years, offer a unique opportunity to expand the current spin-model for pulsars to include long-term timing noise effects (see e.g. Lyne [56] and Backer [3]). Aiding the campaign in the attempt to link timing noise to possible fundamental mechanisms that influence the emission and spin-down of the pulsar, new pulsars were discovered that undergo "pulse nulling" (dramatic switching between radio ON and OFF emission states), mode switching (pulsar switching between several spin-down and emission states). For the latter mentioned observed rotational dynamics of the pulsar, the spin-down state is often correlated with the pulse shape (Lyne et al. [55]). It is also believed that the population of pulsars that exhibit "pulse nulling" and mode switching could be closely

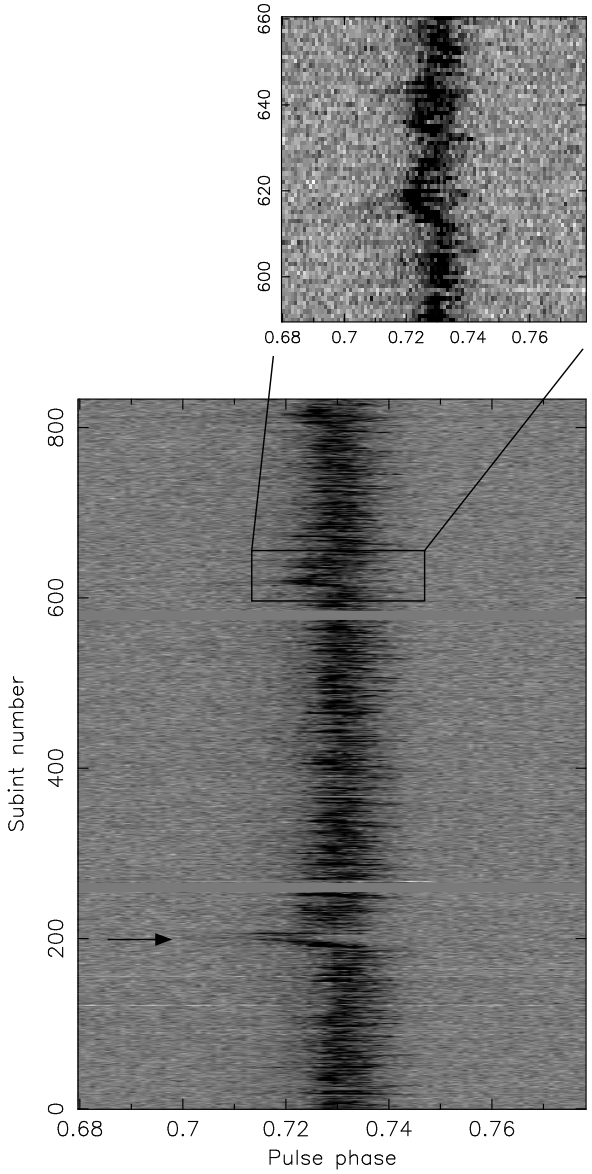

Fig. 4.2: Abnormal emission mode seen in the pulse train of PSR B0919+06, if not modeled, this effect can induce extra "noise" in the timing process, adopted from Perera et al. [69].

related (Wang, Manchester & Johnston [93]) since the conditions in the magnetosphere of the pulsar that produce both phenomena are tied, that is, fluctuations in the magnetosphere's plasma density.

Timing noise can be characterized by a random walk process in one or more of the spin parameters used in the spin-down model of pulsars (Cordes & Helfand [21]) and can be observed in long-term timing of some normal pulsars and millisecond pulsars (Lasky et al. [51]). Timing noise has already been diagnosed in the 80's (see e.g. Shannon & Cordes [84] and references therein) and analyzed using two main techniques; using a statistical parameter that characterizes the strength of timing noise (dimensional Alan variance-like parameter, see Fig.4.3 and Fig.4.4) or directly computing the spin-down rate and computing percentage changes in the spin-down of the pulsar over time. The power density spectra of the timing noise phase residuals follow a red-noise type frequency dependence, see Fig.4.5, and can be removed (or whitened) with relative ease. However, by blindly removing red noise, one can withdraw the opportunity to link the variation in the pulsar's spin parameters to some physical model that could be present among several classes of pulsars (perhaps a unique class of pulsars). The first technique is useful in investigating the relationship of the strength of timing noise and the position of the pulsar exhibiting timing noise on the P-$\dot{P}$ diagram; the latter is useful to extract astrophysical models from the structure of timing noise.

The influence of pulsar timing noise on the timing process can be tracked through the measurement of the braking index of pulsars

$$n = \frac{\nu\ddot{\nu}}{\dot{\nu}^2}, \tag{4.3}$$

Assuming a pulsar with a measured spin-period of $P \approx 500$ ms, first frequency derivative of $\dot{\nu} \approx 10^{-14}$ s^{-2} and a second derivative of the spin frequency of $\ddot{\nu} \approx 10^{-26}$ s^{-3}, we get a value for the braking index of $n >> 3$. This derived value of the braking index contradicts the theoretical index predicted by the dipole spin-down model of pulsars.

Essentially any observed timing noise signature can be linked to variations in the spin parameters of the pulsar, ultimately leading to the hypothesis of the origin of timing noise; either being produced inherently by the pulsar itself or by some external mechanism. Spin variations produced by the pulsar itself are fundamentally

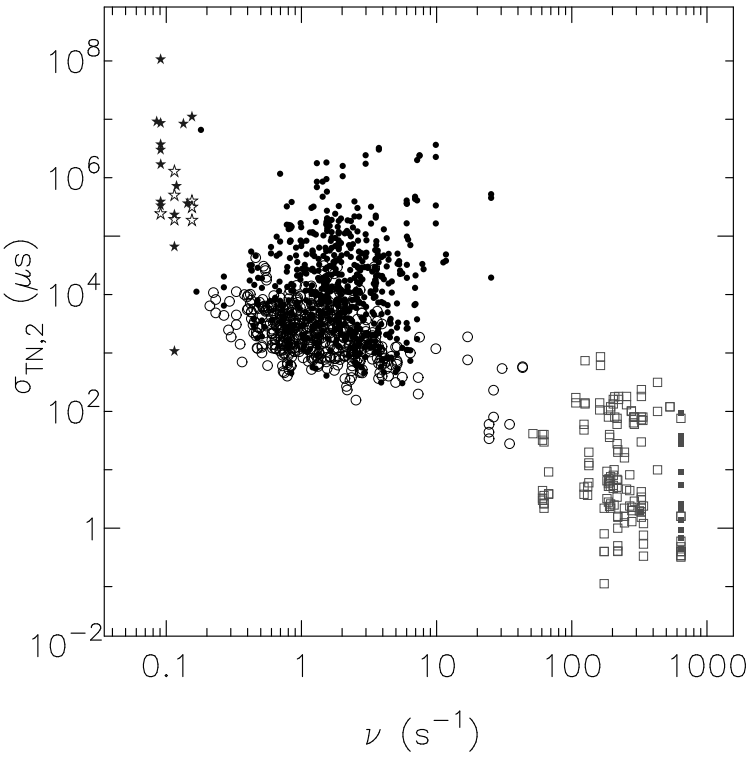

Fig. 4.3: Scatter plot of correlation between the measured rms timing noise and the spin frequency. Filled data points represent detected pulsars with timing noise. Stars represent magnetars. Open symbols represent pulsars exhibiting weak timing noise. Open square symbols represent millisecond pulsars exhibiting timing noise. Older more stable pulsars, such as millisecond pulsars, show less timing noise in comparison with their younger and more energetic counterparts. Adopted from Shannon & Cordes [84].

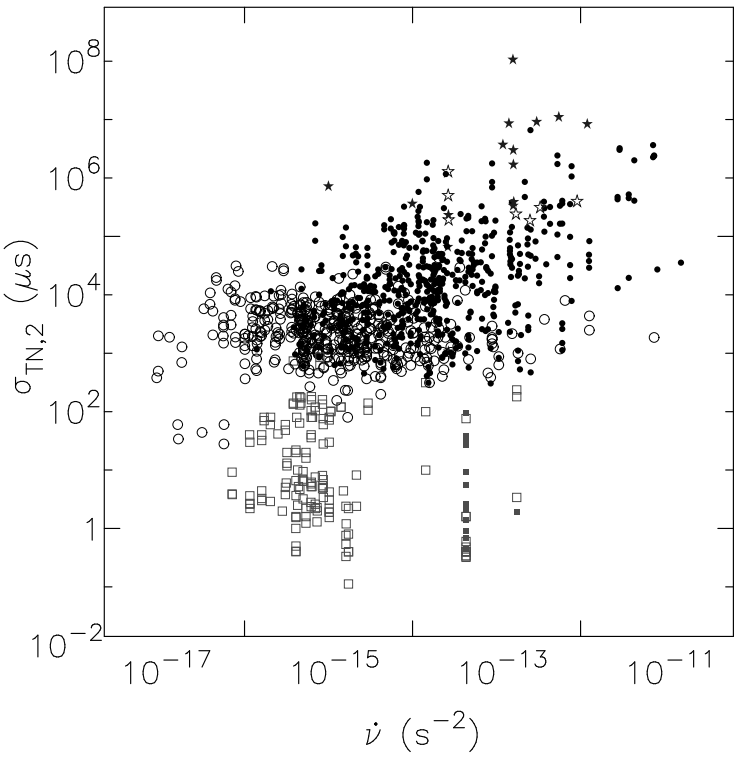

Fig. 4.4: Scatter plot of correlation between the measured rms timing noise and the spin-down rate. Symbols are the same as stated in figure above. Adopted from Shannon & Cordes [84].

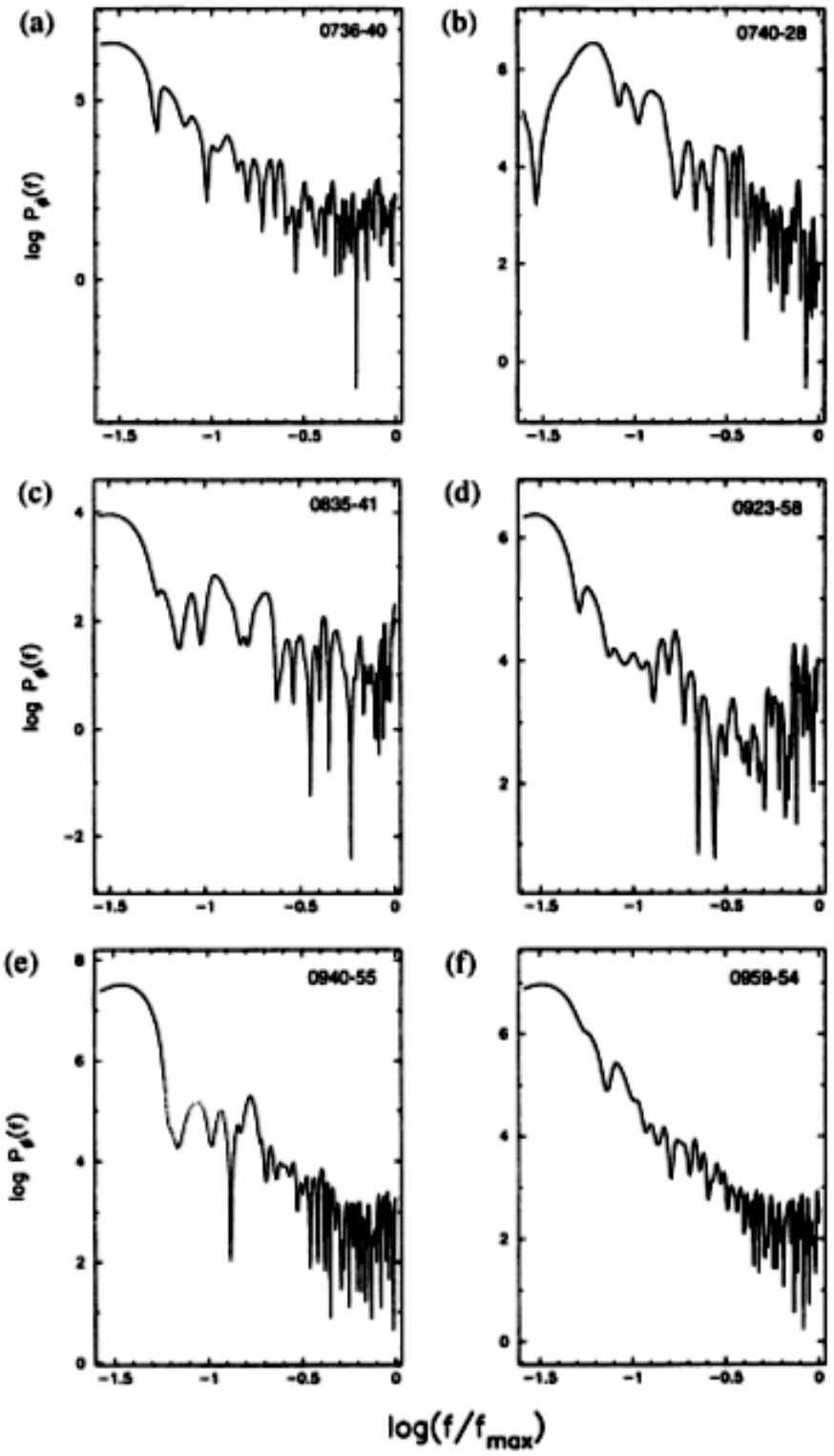

Fig. 4.5: Timing noise spectra of several southern pulsars, adopted from D'Alessandro, Deshpande & McCulloch [22].

tied to the theory of neutron stars that are effects such as neutron star precession (Frescura & Flanagan [30]), sudden spin-ups of the star in the form of glitches (Lyne, Smith & Pritchard [58]) and magnetic field oscillations (Arzamasskiy, Philippov & Tchekhovskoy [2]).

Following one of the largest studies of the timing noise properties of 366 pulsars observed with the 76.2 m Lovell Telescope at Jodrell Bank (Hobbs, Lyne & Kramer [40]), Lyne et al. [55] investigated the most promising timing noise candidates from the list of 366 pulsars. Lyne et al. [55] analyzed the long-term timing noise signatures seen in several pulsars and showed that their spin-down behavior are linked to their pulse shape changes, see Fig.4.6 and Fig.4.7

Following the study of Lyne et al. [55], it became evident that linking the spin-down behavior of a pulsar to any pulse shape changes could shed light on the origin of timing noise, i.e. whether timing noise is caused by spin-deviations of the neutron star itself or due to some external mechanisms that are acting on the star, or a combination of the two mechanisms. One example of these proposed mechanisms are mentioned in Özsükan et al. [64] that models Vela's interaction with a possible fossil disk.

The latter mentioned diagnostic tool led to investigation of pulsars exhibiting unique spin-down rate and pulse shape variations over an extended amount of time, none so spectacular as the activities reported in the timing of PSR J0738-4042 that encountered an proposed asteriod of which the debris can systematically migrate and accrete on the pulsar ultimately changing the star's total torque and emission of which no inherit pulsar process can explain the observations (Brook et al. [11]), see Fig.4.8.

This work extended into the development of new techniques to search for correlations between long-term variability in both the spin-down rate and emission of 168 pulsars in the Parkes survey (Brook et al. [12]). The authors tested their algorithms in the sense of searching for known correlations in the pulsar spin-down rates and emissions, where-after they searched for unknown correlations in the rest of the pulsars remaining in the sample of Parkes pulsars. Their algorithms include methods to calculate profile variability in the form of profile variability maps, which describe the interpolated differences between each observation and integrated pulse profile that is illustrated in the form of a map. From this work PSR J1602-5100 showed clear correlated changes over the total data span, see Fig.4.9.

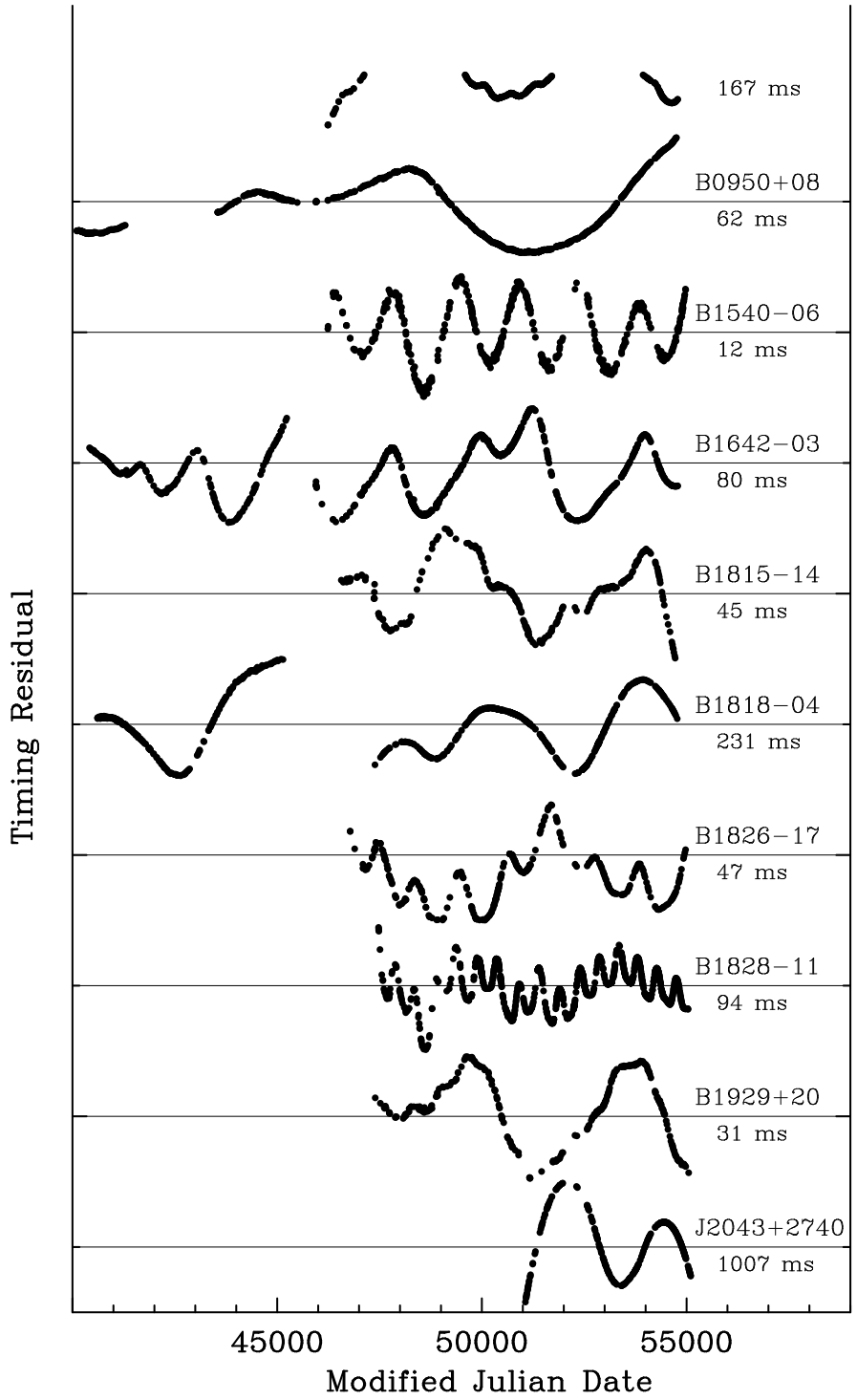

Fig. 4.6: Residual patterns of several pulsar showing timing noise, adopted from Lyne et al. [55].

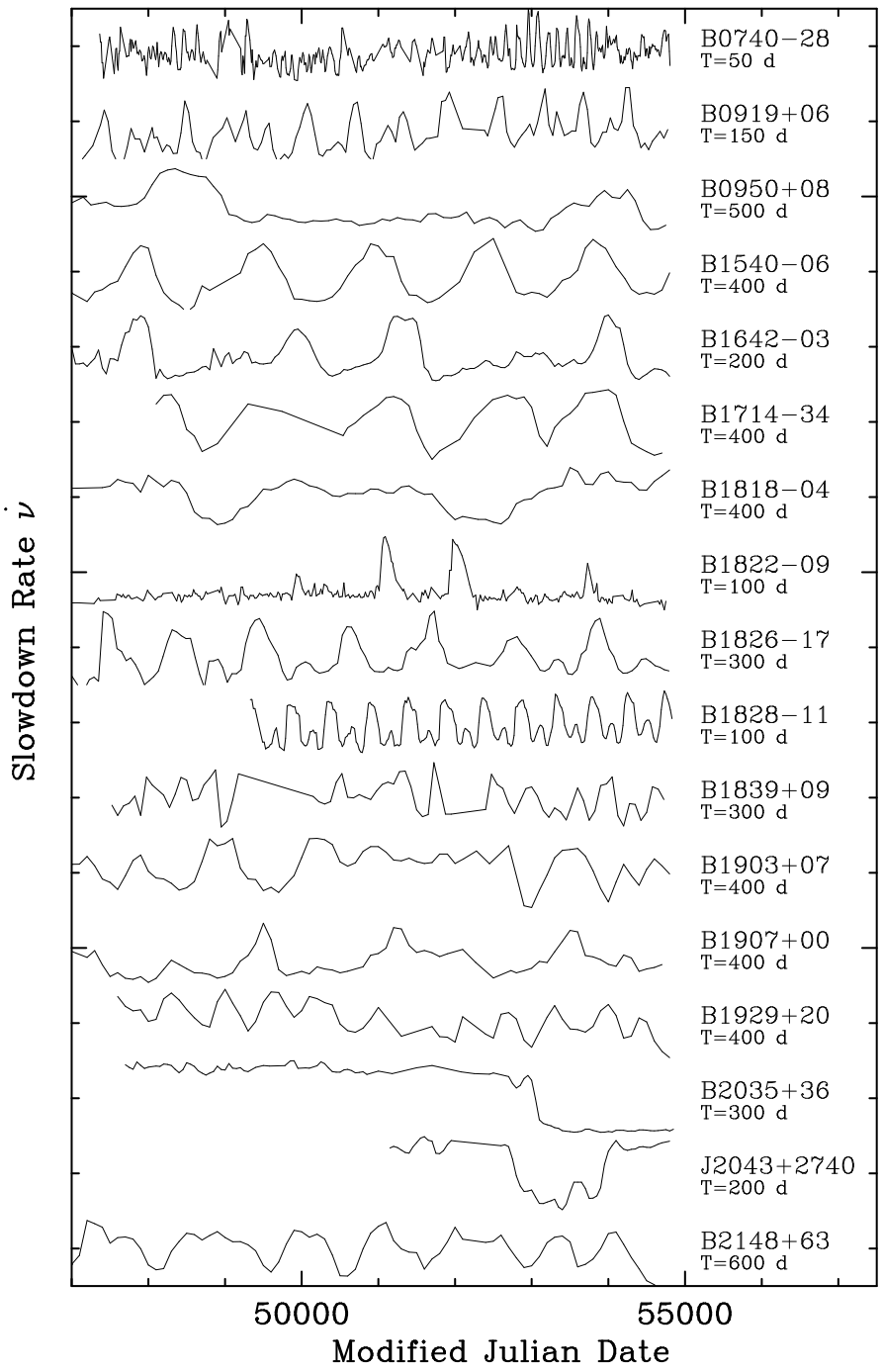

Fig. 4.7: The corresponding spin-down behavior of the pulsar showing timing noise, exhibiting concrete switching between two or more spin-down states, adopted from Lyne et al. [55].

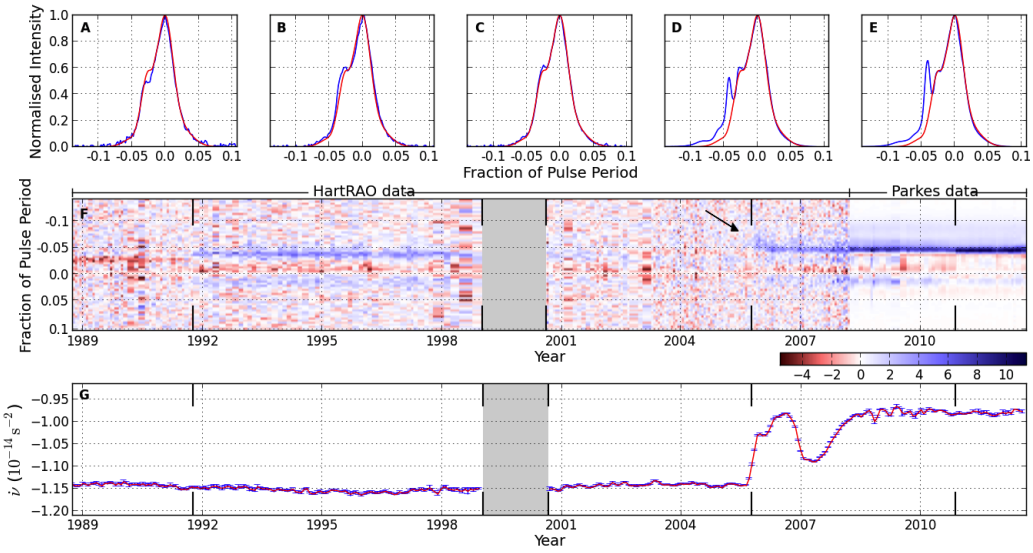

Fig. 4.8: Panel G shows the spin-down rate of PSR J0738-4042 over several years, around 2006 the average spin-down rate increased that is correlated with changes in the average pulse profile (Panel D and E). The grey part in data span represent the time when no observations were taken of PSR J0738-4042, adopted from Brook et al. [11].

In the case of a pulsar encountering an asteroid, the correlated emission changes (or magnetospheric changes) with rotational variations can positively be linked to the interaction of debris with the pulsar, in the sense that the accretion of debris causes a spin-up effect of the pulsar. However, some pulsars exhibit even more mysterious features in their spin-down evolution that can not be correlated to any profile changes, one such case is PSR B0919+06 (Perera et al. [70]) of which 30 years of timing confirms a quasi periodic spin-down evolution, but no profile shape changes, see Fig.4.10.

Kerr et al. [47] searched for variations in 151 young, energetic pulsars, using the Gaussian log likelihood analysis via Carlo Markov Chains methods on the full spin-down model (that include both white and red noise spin contributions). They found the existence of variations of 0.5-1.5 yr in seven of them, possibly owing it to quasi-periodic switching in the magnetosphere of the pulsars.

If the phenomenon of timing noise can be linked to some variation in the spin-parameters of the pulsar, then we can attempt to track the spin-down evolution (or spin-down variations) over an extended period and try to link those variations to some proposed mechanism. This process can be done through precision timing of the

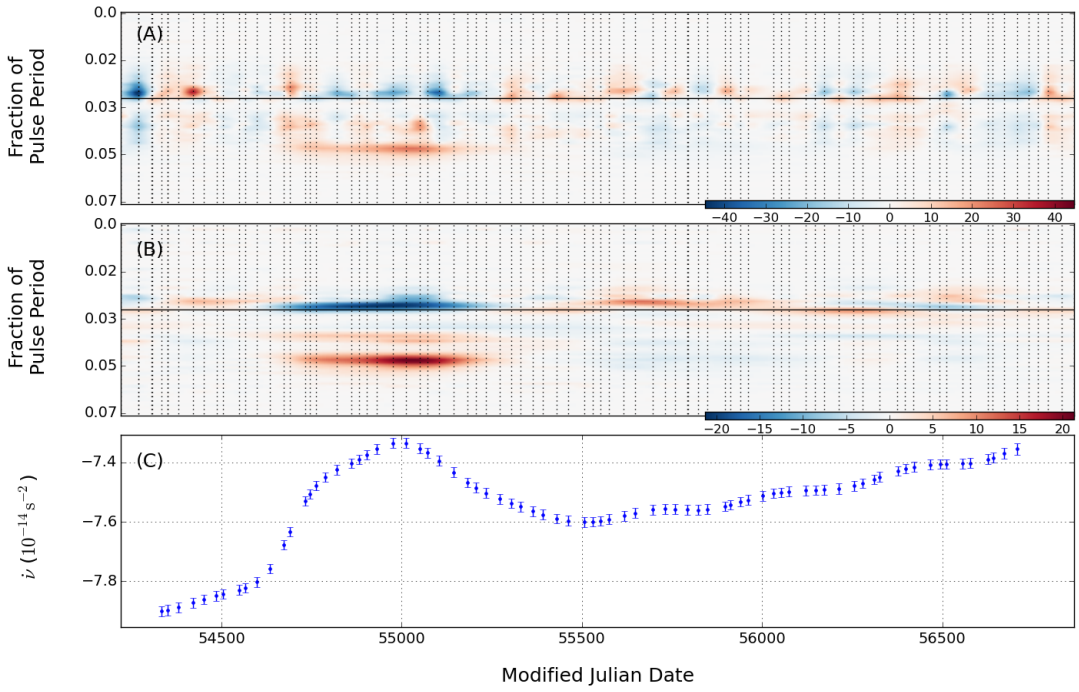

Fig. 4.9: Panel A: profile residual as a function of time for PSR J1602, Panel B: same as Panel A, but in this case the authors use normalized pulse profiles and Panel C shows the spin-down evolution of the pulsar. Adopted from Brook et al. [12].

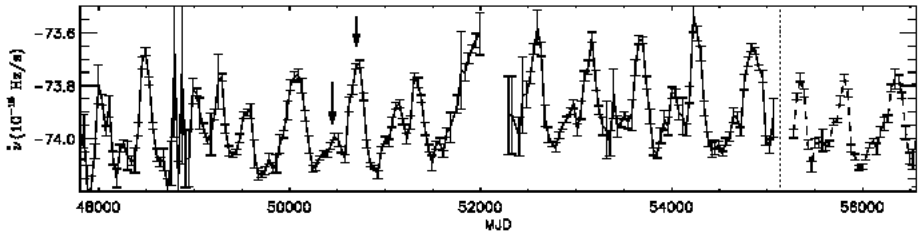

Fig. 4.10: Repeating cycles seen in the spin-down of PSR B0919-06 over several decades, clearly illustrating some clock mechanisms that are rooted in the dynamics of the neutron star. Adopted from Perera et al. [70].

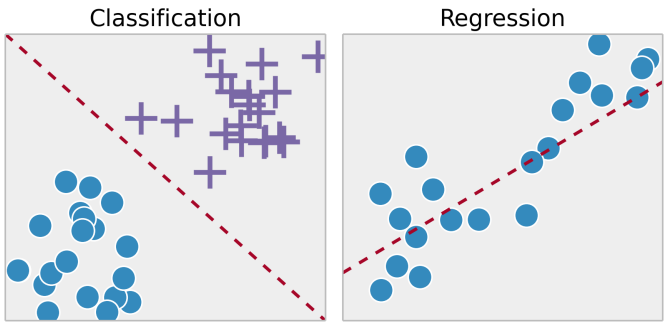

Fig. 4.11: Options in machine learning consisting of either supervised/unsupervised classification or regression among others. Adopted from the sci-kit learn package.

pulsar and the utilization of the timing residuals to produce the pulsar spin-down over time. This is a sensitive operation since we perform first and second derivatives of the residuals to produce the spin-down evolution. There exist several techniques for inferring the first and second derivative from noisy input data, but given the fact that timing noise signatures are generally characterized by quasi-periodic oscillations that are "predictable" in some sense, we specifically focus on the method of Gaussian process curve fitting (henceforth the GPCF method) for the analytic fitting of the residuals and their derivatives. The Gaussian process curve fitting procedure allows the user to generate an analytic expression for the spin-down rate and infer useful information between neighboring epochs of observations, thus producing a highly optimized technique for timing noise residual fitting.

Within the industry, specifically data science, machine learning codes are becoming a fundamental part of the decision and data extraction process of large scale data being produced by modern telescopes. The most frequently used machine code is the classification/clustering of objects/data with respect to a certain characteristic or trends that they might exhibit over time. Classification focuses on identifying to which category/group an object or data entry belongs to, whiles clustering focuses on grouping similar objects/data entries into classes or sub-classes (see Fig.4.11), effectively extracting structure from data possibly not noticed by the observer. To clarify, the reader can refer to Fig.4.12 that illustrates the process of classifying/clustering pulsars on the P-$\dot{P}$ diagram according to their spin properties. Regression machine codes are used to extract an continuous representation of time series data that can allow the observer to extract valuable information/trends from the time series data. For the purpose of this work we initiated minimal pre-processing, since the data was already in a format that was suitable for regression machine learning codes. Some regression machine learning codes depend on some level of feature extraction that can serve as the base for supervised machine learning; a typical feature of timing

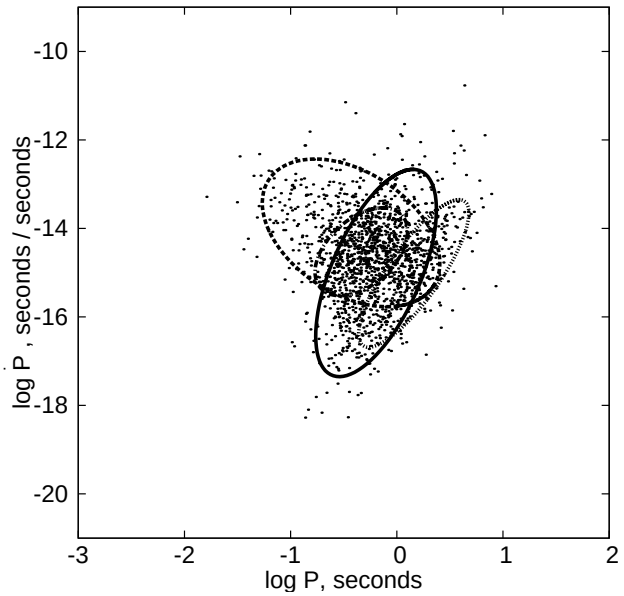

Fig. 4.12: Gaussian mixture model classification of pulsars on the P-$\dot{P}$ diagram, clearly showing subgroups of pulsar populations. This specific classification machine learning code uses that each sub-population on the P-$\dot{P}$ diagram can be described a Gaussian probability distribution. Adopted from Igoshev & Popov [43].

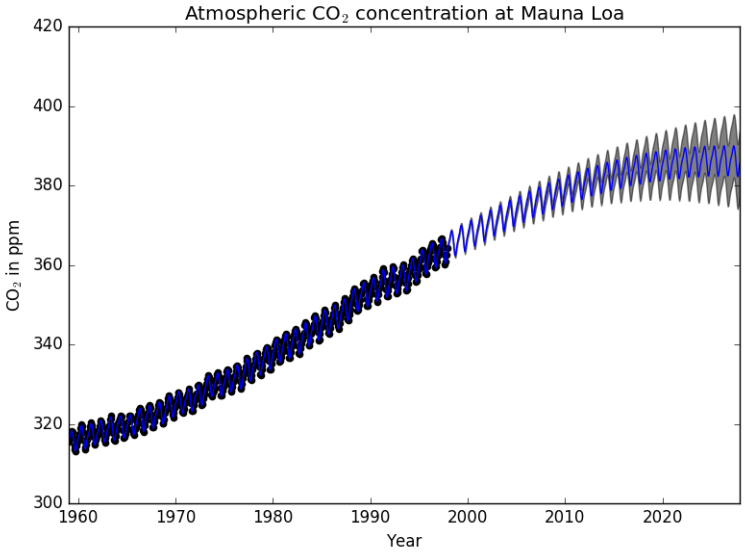

Fig. 4.13: Gaussian process regression of long term CO_2 emission at Mauna Loa observatory in Hawaii, adopted from scikit-learn machine learning package, www.scikit-learn.org

noise will be it's quasi-periodic nature.

The reader is introduced to the concept of Gaussian Process regression via machine learning by using the example of tracking the atmospheric levels CO_2 levels at Mauna Loa observatory in Hawaii over several decades, see Fig.4.13, the objective of this experiment was to model the long-term trend of the CO_2 concentration over decades and infer some information from it. Firstly, an initial kernel needs to be constructed that can be used for supervised learning, this can be done by extracting features from the data that we do have. As a result, the reader will see a long-term smooth rising trend, a periodic trend, some irregularities and noise terms in the data. Then the kernel is constructed to include a radial basis function network (includes the length-scale of features), a seasonal component (includes the periodic component) and a white noise model.

The GPCF method is based on the construction of a statistical kernel that describes the relationship between two neighboring points in the data set with regards to the entire trend of the data set. It is a supervised learning method that is designed to solve regression and classification problems associated with data. This method is being used in the fields of artificial intelligence (AI) where the nature of the data is more or less predictable. The main benefit of this reconstruction process is that the selection window is optimized and the error of the reconstructed function decreases if the residuals are locally predictable, i.e. the algorithm performs better, knowing that

the data is locally predictable, specifically when constructing the co-variance matrix that describes the data. The recipe of the Gaussian Process remains standard:

- **Inspect the data**
- **Choose the appropriate covariance kernel**
- **Construct the priors for the kernel**
- **Train the priors and maximize their likelihood**
- **Find the most probable mean and variance**
- **Load covariance function into memory**
- **Compute derivatives**

The Gaussian fitting process requires no assumptions of whether f (the residual pattern) is related to a specific model that generates the timing residuals. The value of f at some point can be described by x, where x is a Gaussian random variable with mean $\mu(x)$ and variance $var(x)$. The function values at a point x and some other point x' are related by the co-variant matrix, $k(x, x')$. Thus, the latter indirectly implies that fitting a semi-predictable signature (or time series) will produce a good fit to the residuals within a reasonable statistical error margin. The GaPP (Gaussian process in Python) code (Seikel, Clarkson & Smith [83]) was used to perform the GPCF process on the residuals and any time series data for that matter. The GaPP code is widely used for the reconstruction of dark energy and expansion dynamics, without assuming a parameterisation of the function that describes the data or any sub-part of the data.

The GaPP code initializes the Gaussian process with initial parameters for the mean and the variance according some chosen kernel (the different kernels will be discussed at the end of this section):

$$k(x, x') = \sigma_f^2 \exp\left(-\frac{(x - x')^2}{2\ell^2}\right). \tag{4.4}$$

The GaPP code optimizes the step length (l), ultimately producing a fit within the smallest error margin.

Once the kernel that describes the statistical relationship between one point and the other, had been constructed, the function at any point x in the data series can be

calculated by using:

$$f(x) = \mathrm{GP}\left(\mu(x), k(x, x')\right). \tag{4.5}$$

If the data contain considerably large gaps that exceed the constrained length of the chosen kernel, a second kernel with length of that of the largest gap in the appropriate time units can be added to the main kernel. By adding two kernels together, a mathematical operation is executed between the two kernels that is equivalent to the *OR* operation, that is, the resultant kernel will have a high value if either of the kernels have a high value. The addition of kernels automatically conserves the importance of each kernel's step-length.

To illustrate the workings of the GaPP code (specifically when utilizing the Gaussian Process), some build-in examples are illustrated that use data published in Seikel, Clarkson & Smith [83]. The ability of the GaPP code is illustrated by the construction of kernels and their derivatives, which is the most important ability of the code for the purposes of this study. Since the application in this study will be using the derivatives of the reconstructed residual signature to produce the spin-down rate of the pulsar, see Fig.4.14.

The next chapter will be applying the GPCF process to set of timing noise residuals that exhibits quasi-periodical cycles as well as bin-resolved difference of integrated pulses over an extended time span. Before entering this stage, the reader can once again re-visit the standard GPCF process recipe to prepare the method for applications used in this study, particularly towards timing noise signatures in general:

- **Inspect data: Long-term predictability**
- **Choose the appropriate covariance kernel: Square exponential**
- **Construct the priors for the kernel: Residuals with errors**
- **Train the priors: Within the TOA error bounds**
- **Find the most probable mean and variance**
- **Load covariance function into memory**
- **Compute derivatives: Need second derivative**

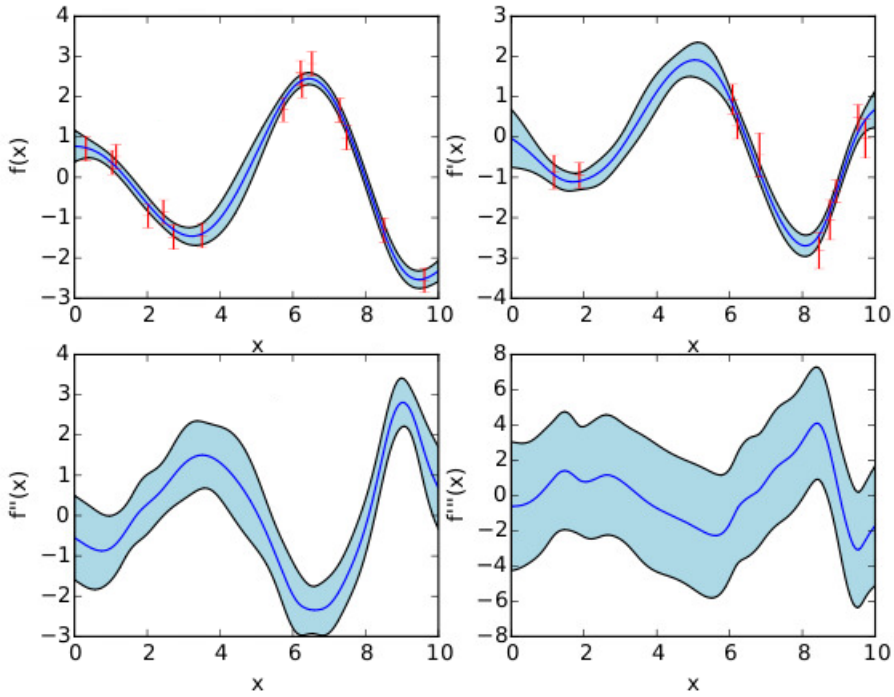

Fig. 4.14: Reconstruction of data based on work of [83], note that the light blue band is represents the error band of the GPCF process.

It needs to be stressed that there exist several GPCF process kernels such as the squared exponential (this is the kernel that was implemented in this study), see e.g. Seikel, Clarkson & Smith [83]

$$k(x, x') = \sigma_f^2 \exp\left(-\frac{(x - x')^2}{2\ell^2}\right), \tag{4.6}$$

which is defined by a length-parameter that has the same dimension as the data set and a variance σ_f which acts like a scaling factor. This length-scale parameter sets the smoothness of the data set, i.e. a small length-scale translates to data that can vary quickly and a large length-scale translates to data that varies over longer timescales. The squared exponential kernel is smooth and suitable for data that is locally predictable. The squared exponential operates under the idea that function variables that are close in the input space are highly correlated and function variables further apart are not.

The double squared exponential kernel can be described as two combined squared exponential kernels

$$k(x, x') = \sigma_{f_1}^2 \exp\left(-\frac{(x-x')^2}{2\ell_1^2}\right) + \sigma_{f_2}^2 \exp\left(-\frac{(x-x')^2}{2\ell_2^2}\right), \tag{4.7}$$

and contains two unique length-scales, l_1 and l_2 and two scaling factors σ_1 and σ_2 that describe the average distance from the mean of the data.

The Matern 32 kernel (see wwww.scikit-learn.org for complete overviews of all the standard kernels) is smooth only up to first derivative and thus not particularly useful for timing residuals regression (of which some useful applications of this kernel will be discussed in the next section). However the Matern 32 kernel is just one of the Matern-class kernels:

$$k(x, x') = \sigma_f^2 \frac{2^{1-\mu}}{\Gamma(\mu)} \left(\frac{\sqrt{2\mu}(x-x')}{\ell}\right)^{\mu} K_{\mu}\left(\frac{\sqrt{2\mu}(x-x')}{\ell}\right), \tag{4.8}$$

where Γ is the gamma function, K_μ is the modified Bessel function, σ_f is the variance (scaling factor), l is the characteristic length-scale that translates the sensitivity of the kernel $k(x, x')$ to the distance between data and μ is the co-variance parameter. The co-variance parameter for the Matern 32 kernel can be chosen as $\mu = \frac{3}{2}$, which produces

$$k(x, x') = \sigma_f^2 \exp\left(-\frac{\sqrt{3}(x-x')}{\ell}\right)\left(1 + \frac{\sqrt{3}(x-x')}{\ell}\right), \tag{4.9}$$

The above mentioned kernels hold the added benefit of addition and multiplication of separate covariance functions remaining covariance functions, thus allowing for the creation of complex covariance functions that will be useful for the Gaussian Process of pulse profile data. From this point forward GPCF kernels that are based on the square exponential kernel will be used due to the fact that it is defined by some variance (σ_f) and step length (ℓ) that can easily be constrained from observations.

Now that a foundation has been laid regarding the various aspects of pulsar timing,

the attention is turned to the source under investigation in this study, i.e. PSR J1326-5859.

Chapter 5

Timing noise of PSR J1326-5859

PSR J1326-5859 is a southern hemisphere isolated pulsar with a period of 478 ms and dispersion measure of 287.30 cm^{-3} pc (D'Alessandro et al. [23] and Hobbs et al. [39]). PSR J1326-5859 maintains an average spin-down of $\dot{\nu} = -1.4172 \times 10^{-14}$ s^{-2} and exhibits quasi-periodic changes in its spin-down evolution. In the past, PSR J1326-5859 had been fitted with a binary companion model and the authors could not reconcile the quasi-periodical timing noise with the binary model (Frescura & Flanagan [31]). The pulse profile of PSR J1326-5859 at 1377 MHz consists of two components that are partially linearly polarized (Johnston, Karastergiou & Willett [45]). See Table 5.1 for the properties of PSR J1326-5859.

The timing data of PSR J1326-5859 is based on a combination of pulsar timing campaigns of which the longest timeline was recorded using the 26 meter dish at the Hartebeesthoek Radio Astronomy Observatory (25.8900 deg S 27.6853 deg E)(e.g. see Fig.5.1). The observations that were performed using the 26m radio dish at HartRAO were centered on the 18 cm and 13 cm bands, both having system temperatures of $T \approx 40$ K. The total time span of the HartRAO timing data for PSR J1326-5859 is between 46395 and 55945 MJD (i.e. 9550 days).

Additional archival data was obtained between 52980-57308 MJD from the 64 m

Table 5.1: Properties of PSR J1326-5859 (Manchester et al. [60])

P_0 (s)	0.47799
DM (cm^{-3} pc)	287.30
RM (rad m^{-2})	-579.6
W_{10} (ms)	23
S_{1400} (mJy)	9.9
d (kpc)	3
age (yr)	2.34×10^6

Fig. 5.1: 26m radio dish at HartRAO, credit Mike Gaylard.

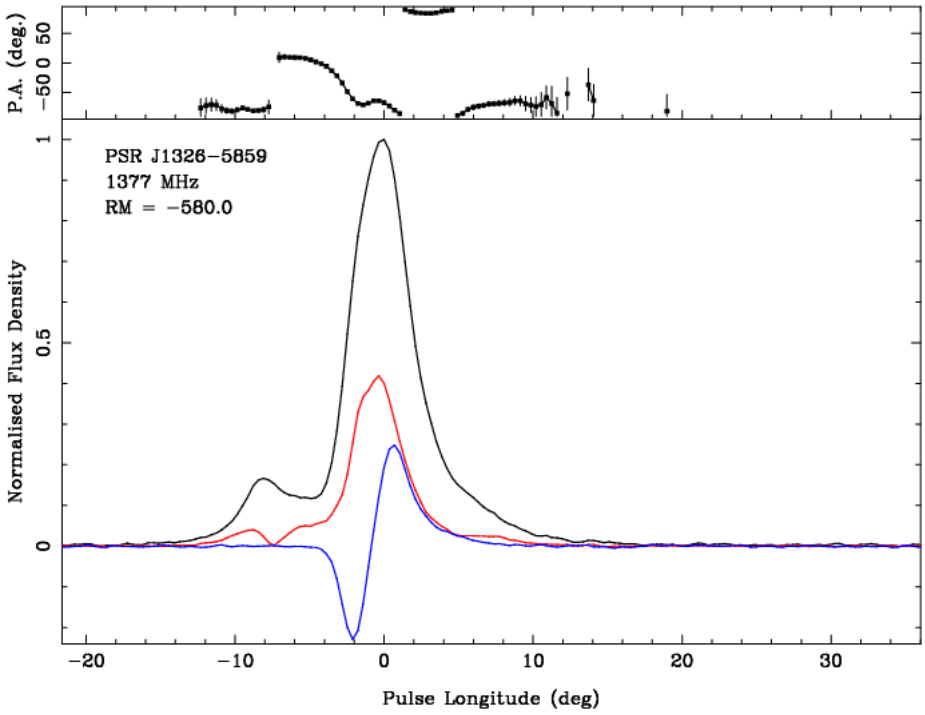

Fig. 5.2: Profile of PSR J1326-5859 at 1377 MHz Johnston, Karastergiou & Willett [45]. The polarization swing shows several polarization jumps, particularly at -7,1 and 5 degrees pulse longitude. The profile is partially linearly polarized (red part), but some part of the profile is also circularly polarized (blue part). Clear Orthogonal Polarization Modes can be observed in the PA profile.

Fig. 5.3: One of the 778m arms of the Molonglo observatory synthesis telescope. Molonglo consist of 352 modules that are individually phased antennae . The modules terminate into 88 receiver boxes within a bandwidth of 100MHz. All the boxes are protected against weather and RFI elements. Pulsars at UTMOST are being timed as part of Molonglo's TIME project.

Parkes radio telescope (Manchester et al. [59]) centered on wavelengths of 10, 20 and 50 cm with two linear polarizations, see Fig.5.2 for the Parkes profile of PSR J1326-5859. The timing campaign was also supplemented with archival data from UTMOST (upgrade to the Molonglo Observatory Synthesis Telescope, see Fig.5.3 and Fig.5.4), between 57134-57591 MJD centered on 840 MHz having single polarization, see Table 5.2 where NTOA refers to the number of times of arrivals.

Both Parkes and HartRAO operate as single dishes connected to two very different pulsar timing machines; HartRAO utilizes a 32 MHz bandwidth IBOB multi-channel timer and Parkes utilizes a multi-beam front-end together with the Parkes Digital Filter Bank 3/4 (PDFB3/4) containing a 1024 MHz bandwidth (that can be divided into a maximum of 8192 channels) and a total of 4 Stokes parameters that can be obtained in pulsar folding mode. UTMOST utilizes 7744 individually phased ring

Table 5.2: Data obtained from three telescopes for J1326-5859

Telescope	Receiver (cm)	T_{system} (K)	MJD	NTOAs
Parkes	10,20,50	35,40,28	52980-57308	43
UTMOST	36	75	57134-57591	42
HartRAO	13,18	35,39	46395-55945	3068

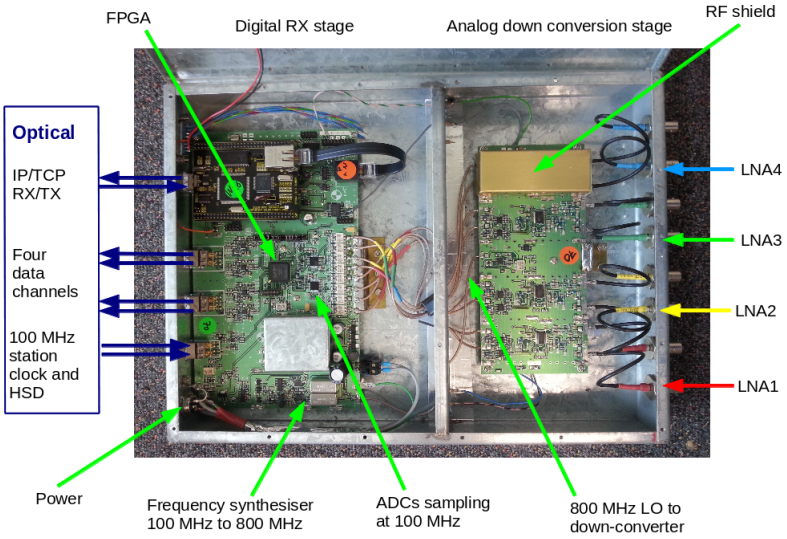

Fig. 5.4: Receiver box of which four Low Noise Amplifiers (LNAs) feed into for processing. This receiver box is one of 88 receivers. The incoming band is centered on 843MHz with 100MHz of bandwidth.

antennae with single right circularly polarization that returns a 100 MHz baseband of usable data using the 2×778 m parabolic cylindrical antennae. Both the Parkes and UTMOST pulsar observations that were carried out for PSR J1326-5859, were done coherently and in-coherently for the observations made by using the 26m radio dish of HartRAO. Coherent pulsar observations made by UTMOST, is done in the the tied array beam mode that basically tie all the modules into a phase array, automatically suppressing radio frequency interference (RFI).

Since the longest base line timing data for J1326-5859 were generated by HartRAO, we will briefly summarize the details of the timing campaign. PSR J1326-5859 was timed regularly with an cadence of once every week as part of the HartRAO pulsar glitch detection program. The HartRAO pulsar glitch detection system was setup and programmed to notify the observer when bright pulsars such, such as Vela, glitched. The back-end (processing computer) folded the 30 minute long base-line data with the period of the pulsar and produced the pulse profiles that were used in this study. The profiles are of low signal to noise ratio (due to fact that PSR J1326-5859 is radio faint) and only total intensity was observed (i.e. no polarization data was observed). These pulses were used in the timing procedure of PSR J1326-5859 to produce the standard pulse profile (which can also be obtained through the ATNF) and generate the list of TOA.

The timing solutions for PSR J1326-5859 for the different telescopes were determined from post-timing and include the necessary timing parameters and phase jumps between different receivers.

- For HartRAO (Chukwude [19] and references therein)

```
PSRJ           J1326-5859
RAJ            13:26:58.27                    550.0394833255903018765O
DECJ           -58:59:29.1                    82505.922498838545280364O
F0             2.0920846016754509171     1    0.00000000001342576834
F1             -1.4151030185417534759e-14 1    1.7037810669560356699e-19
F2             -6.2493502610573602459e-26 1    1.3771061982211963348e-27
PEPOCH         52321.939939302894
POSEPOCH       52321.939939302894
DMEPOCH        52321.939939302894
DM             287.18533614895635608
START          46659.567310245238534
FINISH         54674.593993994869177
TZRMJD         50674.499488182102734
TZRFRQ         1668
TZRSITE        hart
TRES           35092.583
EPHVER         5
CLK            TT(TAI)
EPHEM          DE405
NITS           1
NTOA           2935
CHI2R          0.0000 2931
JUMP MJD 45000 46047.5 -1 0
JUMP -f nccs 1.0418086603617 0
```

- For Parkes (Hobbs et al. [39] and Manchester et al. [59]):

```
PSRJ           J1326-5859
RAJ            13:26:58.27                    0.04000000000000000000
DECJ           -58:59:29.1                    0.40000000000000000001
F0             2.0920902029405675422     1    0.00000000030923949662
F1             -1.4187889495441641255e-14 1    4.8472242546151166386e-19
PEPOCH         47781.786000000000001
POSEPOCH       47781.786000000000001
DM             287.29999999999999999          0.15000000000000000001
```

```
START              52980.870067340336391
FINISH             57129.399495002100593
TZRMJD             54334.111342497549437
TZRFRQ             6200
TZRSITE            pks
TRES               5539.191
EPHVER             2
CLK                TT(TAI)
UNITS              TDB
TIMEEPH            FB90
DILATEFREQ         N
PLANET_SHAPIRO N
T2CMETHOD          TEMPO
NE_SW              9.961
CORRECT_TROPOSPHERE  N
EPHEM              DE405
NITS               1
NTOA               36
CHI2R              0.0000 33
JUMP -B 20CM 0 0
JUMP -B 40CM 0 0
JUMP -B 50CM 0 0
JUMP -dfb3_J0437_56160_60000 1 0.0000004500
JUMP -pdfb1_post_2006 1 -0.0000001300
JUMP -pdfb4_56160_60000_cals 1 0.0000004250
```

It is clear that the above mentioned emphemerides contain the necessary jumps for changes in the receiver systems, specifically when the receiver system is replaced by a more sensitive one, i.e. in the case of upgrading from the Pdfb1 (Parkes digital Filter-Bank) to the Pdfb4 (for more accurate TOA). Both the Parkes and HartRAO ephemerides used the DE405 planetary emphemeris provided by NASA that was created in May 2007. The JPL planetary ephemerides are generally created to support spacecraft missions in the solar system, but the pulsar community uses it for timing specifically when converting the TOA to the solar system barycenter and accounting for time delays induced by the planets and the Sun (e.g. Lorimer & Kramer [54] p.206). The positions of the planets, the Sun, the Moon and the largest asteroids are computed accurately for any instance. The planetary ephemerides can be adjusted between different model coordinates, i.e. between J2000 and B1950 (from here the J and B names of pulsars). The solar system ephemerides are programmed into pulsar timing software such as *TEMPO2* and the TOA (see Chapter 3 for the timing procedure and time standards of pulsars) are converted to the solar system barycenter.

Pulsar timing can also be used to improve the solar system ephemerides via the fitting of the orbital parameters for planets from the non-zero residuals. Very long baseline interferometry (VLBI) observations of pulsars can also be used to construct an accurate reference position for the earth's orbit and improve the solar system emphemerides (see e.g. Li, Guo & Wang [52]). A sufficient number of TOA were recorded by all three telescopes to ensure timing solutions for PSR J1326-5859 and to produce unique parts of the total timing noise signature spanning all the data sets. Generating a timing solution depends on a sufficient amount of TOA to perform the process of least squares to obtain the spin-parameters of the pulsar. From here the observed TOA can be compared with the predicted TOA.

After computing the spin-down history of the PSR J1326-5958, one can look at the spin-down history to identify certain signatures worth investigating and attempt to link those changes to any pulse profile changes or polarization changes. All the latter mentioned parts of the analysis require unique data structures (that can be read by standard pulsar software) and computing tools that will be discussed in detail in this chapter.

Before computing the spin-down history of PSR J1326-5859, a list of residuals and TOA errors (uncertainties in the time stamps of the pulse or the uncertainty in the width of the observed pulse) was compiled for the total data set using the *TEMPO2* package (*TEMPO2* generates a text file containing the timing residuals and their corresponding errors). These residuals and TOA errors serve as the input for the GaPP (Gaussian Process in Python, see Seikel, Clarkson & Smith [83]) code and are the data points that need to be fitted through the process of regression. The GaPP code initializes the Gaussian regression process with initial parameters for the mean and the variance (i.e. the scaling factor of the regression fit) according to the squared exponential kernel, which is:

$$k(x, x') = \sigma_f^2 \exp\left(-\frac{(x - x')^2}{2\ell^2}\right), \tag{5.1}$$

where σ_f is the scaling factor and ℓ (also known as the kernel step length in the field of machine learning) represents the impact parameter that defines what influence the distance between two neighboring points have on the kernel (see chapter 4 for a discussion of the popular regression kernels). The GaPP code optimizes the step length (ℓ), ultimately producing a regression fit within the smallest error margin that can describe the data in a continuous manner. The process of reducing the

error margin can be done by repeating the Gaussian process. If the data contains considerable large gaps in the time domain that exceed the constrained length of the chosen kernel, a second kernel can be added with a length-scale (ℓ) of that of the largest gap in the time series (this will insure that the gap in the time series will be smoothly fitted). By adding two squared exponential kernels to form a new kernel , a mathematical operation between the two unique kernels that is equivalent to the *OR* operation in logic theory will performed, that is, the resultant combined kernel will have a high probabilistic value if either of the kernels have a high probabilistic value. The addition of kernels automatically conserves the importance of each kernel's step-length (ℓ). Lastly, following the training of the parameters that describe the square exponential kernel for the data regression on the complete timing noise signature, calculating the co-variance matrix (i.e. the matrix that describes the relationship between each data point) and the reconstruction of the functions that describe the residuals, the first and second derivatives of the residuals were computed, see Fig.5.5 using the GaPP code. The parameters for the Gaussian process were optimized to be $\ell = 232$ days and $Var(x) = 2.8 \times 10^{-2}$ (i.e. the scaling factor of the regression process) for the entire data set.

The spin-down evolution of PSR J1326-5859 presented in Fig.5.5 shows clear changes (or mode switching) in the spin-down evolution, ultimately moving from a smaller to a larger spin-down state. Two distinct spin-down evolution parts are noticed, from 47000 to 51000 MJD (part A) and from 51000 to 55000 MJD (part B). Part A of the spin-down evolution switches between two states and part B continues this switching, but the average spin-down over this part decreased. Part A and B in the spin-down evolution of PSR J1326-5859 also corresponds to two different parts of the timing noise signature, i.e. after 53000 MJD the timing noise signature changes in structure. The spin-down evolution of PSR J1326-5859 already points to some mechanism that is changing the spin properties of the pulsar on a time scale of several decades. To constrain the inner workings of this mechanism, an investigation was launched to search for possible correlations with activities in the magnetosphere of the pulsar.

In an attempt to link the spin-down evolution of PSR J1326-5859 to the magnetosphere of the pulsar, archival polarization and pulse profile data collected by HartRAO and Parkes telescopes were utilized. The process of searching for correlated activities in the magnetosphere with the spin-down evolution of the pulsar, was initiated by the analysis of archival Parkes polarization data. The evolution of the polarization vector orientation can translate to changes in the magnetosphere or emission region, i.e. dynamical features can be tracked in the magnetosphere of the pulsar (such as accretion). At this point the possibility of external mechanisms (such as pulsar-disk interactions) altering the polarization vector orientation of the

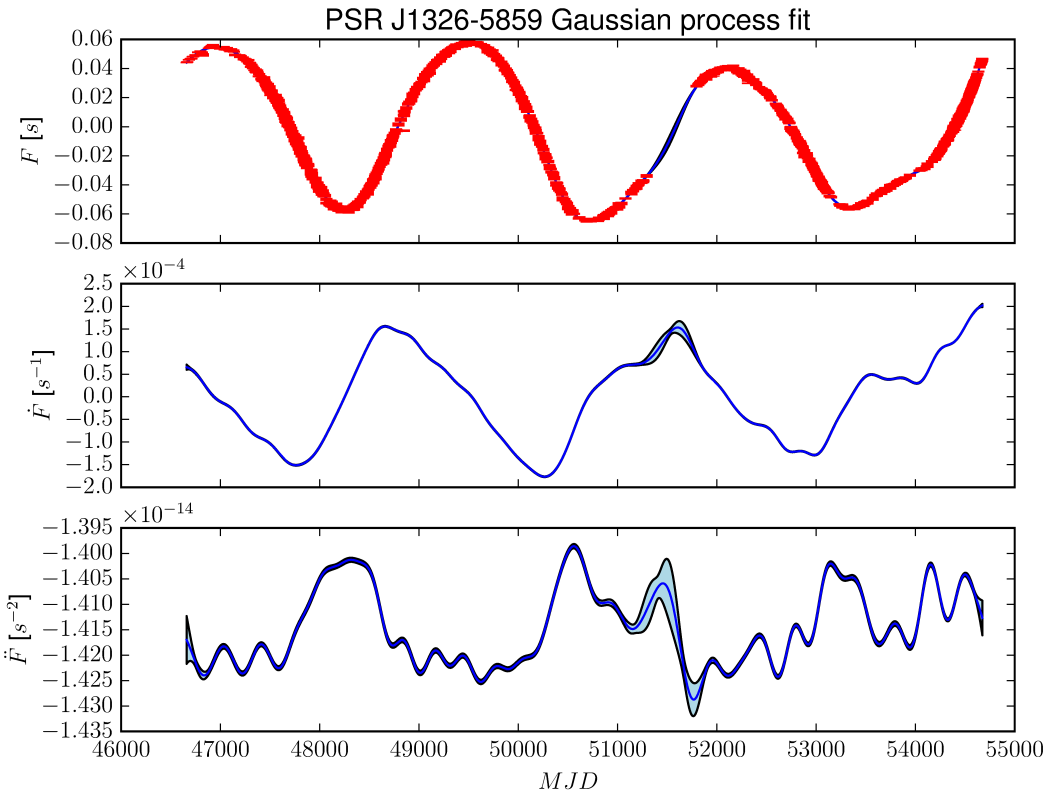

Fig. 5.5: Spin-down evolution of PSR J1326-5859. Upper panel: Continuous regression results after performing the Gaussian process on the timing noise residuals. Middle Panel: Spin-down (ν). Lower Panel: Spin-down evolution ($\dot{\nu}$). Errors of the fit are indicated by the shaded regions. The regressed timing noise residual signature, including the derivatives, are smooth and continuous. F is the fitted residuals, therefore $\dot{F} = \nu$ and $\ddot{F} = \dot{\nu}$.

emission can not be excluded. The reader will firstly be introduced to the basic methodology of phase-resolved polarization studies of pulsar radio emission.

The pulses that arrive at the antenna have a net polarization that is generally stated in terms of the Stokes parameters I, Q, U and V (see chapter 2 for the derivation of the Stoke parameters). These parameters are related to the total observed intensity, which is $I^2 = Q^2 + V^2 + U^2$. Taking the ratios of these parameters will produce the degree of polarization of the radio emission produced by the pulsar. These parameters are generated in the telescope hardware after the measurement of the components of the electromagnetic radiation by the orthogonal feeds of the receiver. Mining the Stokes parameters associated with every observation requires sufficient calibration and tools for tracking any changes over long time spans. A purely linearly polarized wave will have $V = 0$, while $V/Q = 1$ will be true for right-circular polarized pulsed emission and $V/Q = -1$ will be true for left-circular polarized pulsed emission. Most pulsars are known to be highly linearly polarized (due to synchrotron radiation), but also exhibit some degree of circular polarization (see Osłowski et al. [63] for examples). The aim of using polarization in this correlation analysis of PSR J1326-5859 was to search for changes in the polarization data over the total time span of available timing data, for this reason the method of phase-resolved (bin by bin) tracking of the polarization vector was used over many epochs. For example, if the polarization state of one pulse changes from left-handed circularly polarized to right-handed polarized, it will imply that either the emission mechanism (the magnetosphere or magnetic field configuration of the pulsar) or the feeds of the receiver changed the polarization state. As an additional supporting guideline, the reader is referred to Osłowski et al. [63] for a study on the phase-resolved polarization analysis of the single polarized pulses of PSR J0437-4715.

Using this method we can easily see whether the polarization characteristics of the pulse (or components of the pulse) changed and whether it changed in a correlated manner with the spin-down evolution or profile evolution of the pulsar.

To investigate the mode of polarization as it evolves temporally, a phase-resolved polarization analysis (see Osłowski et al. [63]) was performed by plotting the phase resolved polarization vector for every retrieved archival 3100 MHz polarized Parkes pulse (see e.g. Fig.5.6) that was recorded with the wide-band correlator and calibrated to remove feed leakage (Manchester et al. [59]). The list of profiles was phase aligned and centered on phase bin 0.5 by rotating the individual profiles in phase space until aligned (this process was done with PSRCHIVE). The analysis was done by choosing a pulse phase range (p_1, p_2) of interest (could also be the entire phase range of the recorded pulse) after which the polarization vector was computed using

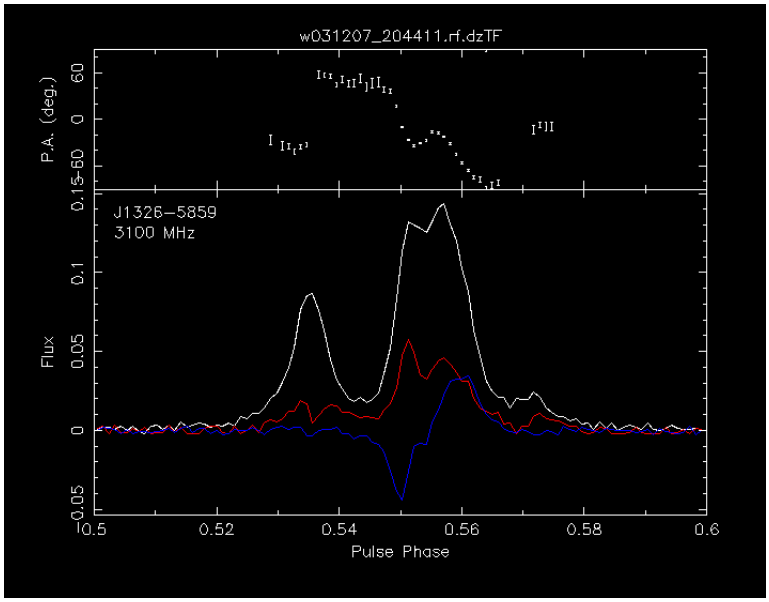

Fig. 5.6: Profile of PSR J1326-5859 observed with the Parkes telescope centered on 3100 MHz and processed with the wide band correlator. The polarization swing across most of the on-pulse profile is eminent from 53174 to 53249 MJD that corresponds to a shift in the spin-down rate from the larger spin-down rate to the smaller spin-down rate (Manchester et al. [59]).

PSRPOL for each phase bin (of 1024 phase bins) within the specified range per epoch. This data were represented as pixels on a sphere containing 768 pixels. The reader is referred to the section that covered radio wave polarization in Chapter 1, that illustrated how to retrieve the polarization vectors for the electric field from Maxwell's equations for a plane wave solution.

Representing each chosen epoch's polarization vector was done using the package HEALPIX (Herarchical Equal Area iso Latitude Pixelation of a sphere, Górski et al. [35]). HEALPIX is used in conjunction with PSRCHIVE to drive fast and accurate analysis of large data sets and is commonly included as part of the HEASOFT package. Representing the polarization vector on a sphere of pixels is nothing else but a representation of the Poincare sphere that can be used to check the nature of the polarization of some part of the pulse (see Fig.5.7 and Wang et al. [94]). This method of illustration can reveal either one or two modes of polarization that originate from two different emission modes, for example orthogonal polarization modes induced by emission propagating through different plasma densities. At any given moment the polarization vector is a composition of all the polarization components of the particular phase bin of the pulse. This polarization vector tracking process was done for archival Parkes polarization data that overlapped the long-term HartRAO data set of PSR J1326-5859, specifically from 52980 to 53964 MJD. The representa-

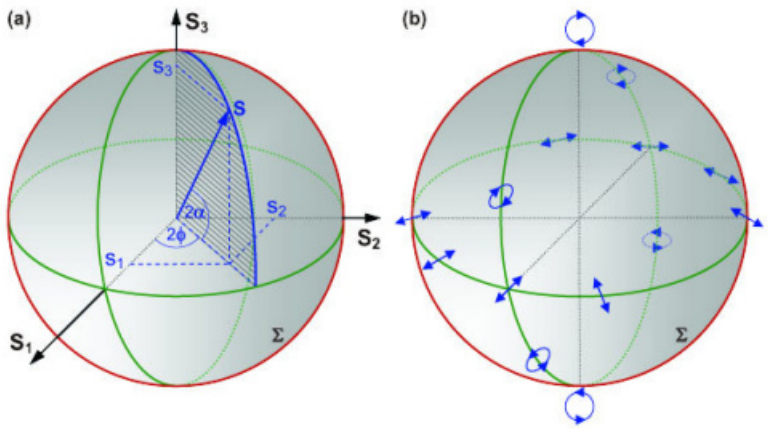

Fig. 5.7: Movement of the projected polarization vector of the electromagnetic radiation on a Poincare sphere through several modes of polarization (e.g. linear to circular). The state of the polarization vector (whether linearly of circularly polarized) can be checked with ease. Adopted from Wang et al. [94].

tion of the polarization vector orientation in a graphical manner allows the observer to track the polarization orientation of the received pulsed EM radiation from one epoch to next. It should be noted that many factors could contribute to the changes in the orientation of the polarization vector, including phase-changes induced by the receiver feeds (cross polarization leakage of the feeds), changes in the plasma levels of the magnetosphere, ISM effects (e.g. Faraday rotation) or polarization swings via the reflection of electromagnetic radiation from dense sheets of material or disks. Using calibrated polarization data will ensure that no man-made polarization swings occur, that could lead to misinterpretations of the dynamics seen in polarization data. It is also equally important to group the polarization data according to the observation frequency to prevent obvious polarization vector changes from one frequency to the next due to receiver changes and depolarization (Gil & Rudnicki [33]).

The result of the phase resolved polarization study of PSR J1326-5859 mentioned above are presented in Fig.5.8. Each column represents a different phase bin of the pulse profile of PSR J1326-5859. Each row represents Parkes polarization vectors at different epochs (chosen to overlap the HartRAO long-term data). Technically, polarization vector in the region of $MJD = [52980, 53039,$
$53117, 53174, 53964]$ reside in the larger spin-down state of PSR J1326-5859 (see Fig.5.5 for the temporal reference) and the polarization vector in the temporal region of $MJD = [53249]$ resides in the smaller spin-down state. The phase-resolved analysis was applied to integrated pulse profiles and (for statistical and continuity purposes) the resolution of the method will improve significantly when single pulses are investigated (on the time sale of the rotation of the pulsar). No orthogonal

polarization modes (OPM) can be seen in the phase-resolved polarization plots (see Fig.5.8), since the representations do not show polarization vectors that are a combination of two polarization components separated by 90 degrees. The absence of observed OPM could prove to be useful when trying to link the spin-down changes to activities in the magnetosphere of the pulsar, since it could help to constrain elements such as plasma density changes within the specific phase bin of the pulse. (Osłowski et al. [63]).

Looking at the folded 3100 MHz Parkes profile (see Fig.5.6) one can see different morphological structures in the pulse that represent emission from different heights or modes. The degree of polarization associated with the profile diminishes in the off-pulse region of the pulse and becomes strongly linearly polarized in the on-pulse region. According to Fig.5.8 the polarization vectors toward the edges of the pulse window become less intense and do not prefer any particular mode of polarization. The polarization vectors become more intense and adopt a particular mode of polarization towards the on-pulse region of the pulse window. The latter mentioned result can be interpreted by the polar cap radio emission model of pulsars, showing predominant polarized emission towards the on-pulse region of the pulse window. It was also noted that the 1377 MHz pulse profile (see Fig.5.2) is different to that of the 3100 MHz pulse profile both in morphology and the degree of both linear and circular polarization. The latter mentioned observation further supports the requirement of grouping the polarization vectors according to observational frequency. If polarization data from different frequencies are used, one could possibly see depolarization towards higher frequencies, which will make the task of systematically tracking the polarization vector over several epochs, difficult (see Gil & Rudnicki [33]).

Changes in the mode of polarization were noticed as the pulsar transcends from one spin-down state to another and back again. In the time domain the latter mentioned spin-down rate switch occurs between $MJD = [53174]$ and $MJD = [53249]$, and back again between $MJD = [53249]$ and $MJD = [53964]$ (see Fig.5.9). This abrupt change in the spin-down rate observed in PSR J1326-5859 correlates with a polarization swing that is eminent across all on-pulse phase components (visible from left to right in Fig.5.8 from 53174 - 53249 MJD), ultimately supporting the implication that the change in the magnetosphere (also the polarization swing) is global and not isolated to specific parts of the pulse. The Poincare representation of the polarization vectors became useful in determining the mode of polarization through investigating the position of the projected polarization vector using the HEALPIX (see Fig.5.8). In this case the polarization vectors (not to be confused with the polarization angle (PPA) swing through one rotation of the pulsar) are separated

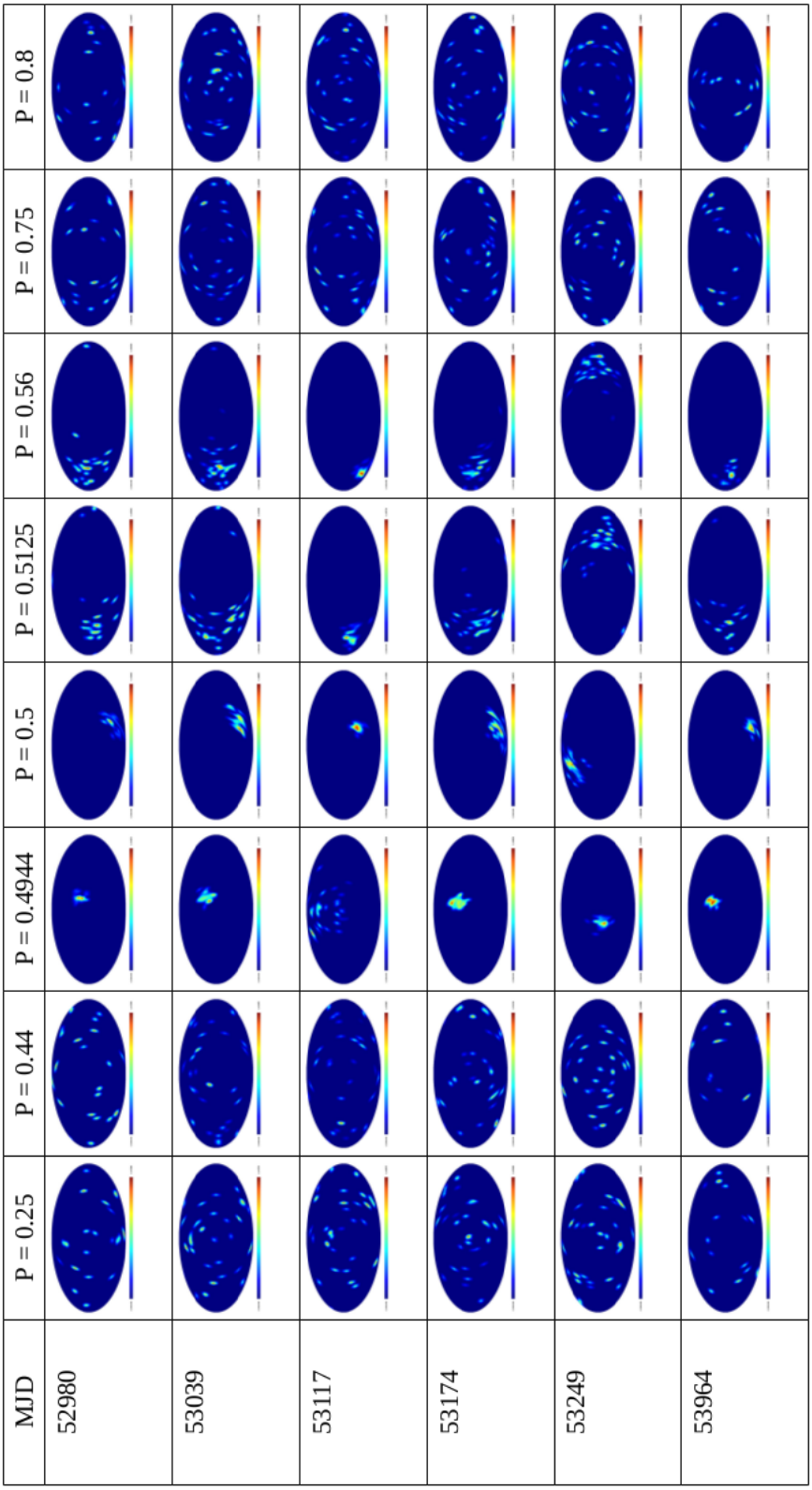

Fig. 5.8: Phase resolved polarization vector maps of J1326-5859 at different epochs for different phase components. Each column represent a different phase bin of the pulse profile. Each row represents Parkes pulse profiles at different epochs.

by roughly 180 degrees as the pulsar switches from a larger spin-down state to a smaller spin-down state and back again, indicating to the possibility that some additional mechanism added to the total polarization mode as the pulsar moved from one spin-down state to another. The latter mentioned phenomena could be in the form of additional reflected emission (with a polarization swing) or accretion from a disk, as will be shown in the next chapter. Idealistically, one wants to prove that every spin-down mode of PSR J1326-5859, can be associated with some particular polarization vector mode and pulse profile morphology/intensity, after which we can tie the observations to a possible model (see Brook et al. [12] and references there-in for similar studies). Correlations between the spin-down, polarization vector and pulse profile changes of PSR J1326-5859 will be discussed later in this chapter.

To search for correlated changes in the pulse profile data, we used the HartRAO pulse profiles that were used for the timing process of PSR J1326-5859 (process of generating TOA) and subsequently the calculation of the spin-down history of PSR J1326-5859. This was done by aligning the pulses in phase space and discarding any pulses that did not meet the required signal to noise ratio limit (a S/N of less than 5). The total number of profiles that were used was approximately 2847 and spanned most of the data set of HartRAO, however, some of these pulses were not used in the process due to low S/N.

One way to investigate the possible variability exhibited by a list of profiles that were observed at the same frequency, is to compute the profile characteristics (profile width, area etc.), but the technique is only effective for high S/N pulse profiles (e.g. in the case of Vela profiles). To deal with low S/N pulse profiles we employed a machine learning technique that was used in Brook et al. [11], known as pulse profile difference maps (also known as profile residuals). This technique employs aligned phase-resolved subtraction between every pulse in the list and an integrated stable pulse. The stable pulse was created by adding all the pulses across the entire data set and forms a fundamental part of the pulsar timing process. However, fitting this difference map with a suitable model relies on a combination of models that can describe both possible variability in the pulse residuals (possibly due to changes in the magnetosphere of the pulsar) and profile uncertainty. This model comes in the form of a combined Gaussian process regression model (the same model as was used to compute the spin-down of PSR J1326-5859) that consists of a kernel described by a white noise Matern function (Brook et al. [11]):

$$k(x, x') = \sigma_f^2 \left(1 + \frac{\sqrt{3}r}{\ell}\right) \exp\left(-\frac{\sqrt{3}r}{\ell}\right) + \sigma_n^2 \delta_{xx'} \tag{5.2}$$

Here, ℓ is the familiar step length of the kernel that can be constrained according to the user's requirements of the fitting process and $r = x - x'$ is the difference between two training points (or epochs). The constraining process of the step-length ℓ relies on the Gaussian model that was fitted to the spin-down data. The constraining of the step-length will save computational cycles, but the user can search for any range of step-lengths. From the Gaussian process regression fit that was used to compute the spin-down evolution of PSR J1326-5859 previously, we can constrain the step-length (ℓ) for the Gaussian process of the pulse residuals to be between 100 and 500 days. We refer the reader to Brook et al. [11] for several examples of this process. Using the pipeline VGP (Brook et al. [11]) we proceeded to produce a difference map for the main pulse component for most of our 1644 MHz HartRAO recorded profiles.

One clearly sees alternating pulse profile intensity changes with time that are centered around the main component of the 1644 MHz HartRAO pulse profile. However, the feature appearing at MJD = 53000 shows a dramatic quenching of the the main pulse profile intensity. This feature corresponds to the time in the spin-down evolution of PSR J1326-5859 where the timing noise characteristic changes (after the gap in the data, see Fig.5.9). This result show some correlated changes between the spin-down history and the variability in the pulse profiles, this is: the feature appearing at MJD = 53000 corresponds not only to the region where the polarization vector changes spin-down states but also where the average $\dot{\nu}$ changes, from $-1.425 \times 10^{-14} s^{-2}$ to $-1.410 \times 10^{-14} s^{-2}$, see Fig.5.9.

The upper panel Fig.5.9 clearly shows that the normalized flux difference map (between individual and integrated pulse profile) varies quasi-periodically and is correlated with the spin-down variations shown in the lower panel. Qualitatively from Fig.5.9 one can deduce that there must exist a mechanism that changes the spin-down rate of the pulsar and changes the emission model. Adding to the mystery, PSR J1326-5859 exhibits no visible pulsations in Gamma-ray, X-ray or optical emission, which could indicate that the mechanism that is influencing PSR J1326-5859's spin-down. Having a multi-wavelength signature allows utilizing data in alternative frequency bands for correlation studies which could confirm or deny the confirmation of extended mechanisms such as a fossil disk.

Using the archival residuals of PSR J1326-5859 observed with the Parkes and UTMOST telescopes, it can be seen that the timing noise residuals remain stable and quasi-periodic at the present time (see Fig.5.10 and Fig.5.11). The additional timing

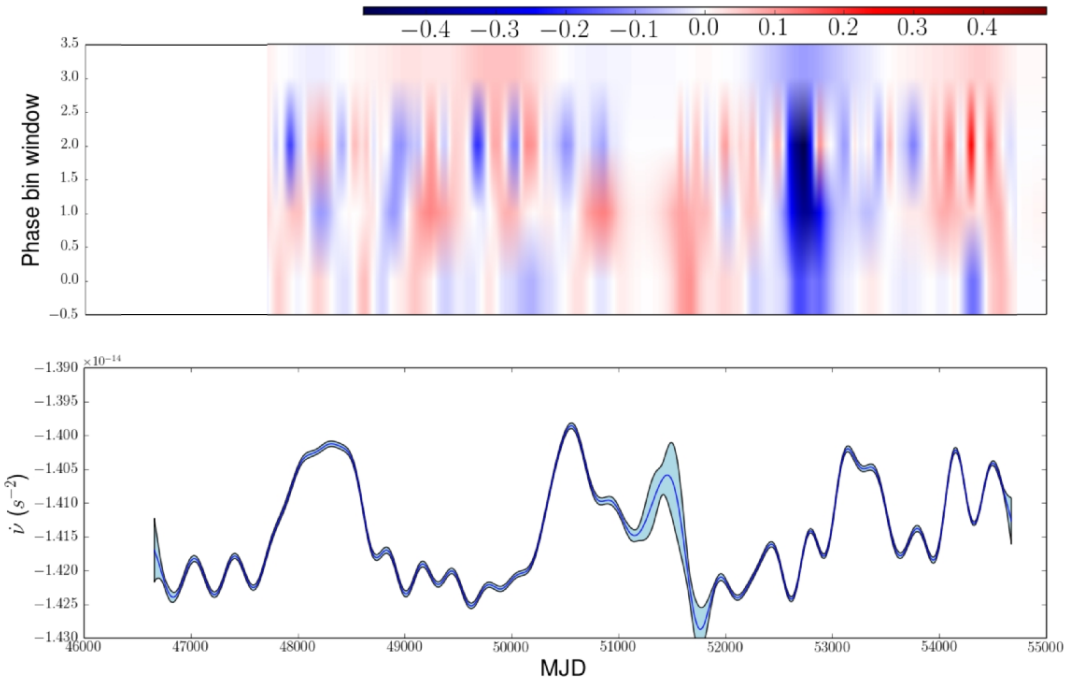

Fig. 5.9: Phase resolved difference map (or pulse residuals) along the main pulse component. This corresponds to a bin size of 10 centered at phase bin 500 (of total bins 2048), see Brook et al. [11]. The lower panel represents the computed spin-down of PSR J1326-5859 via the Gaussian regression process.

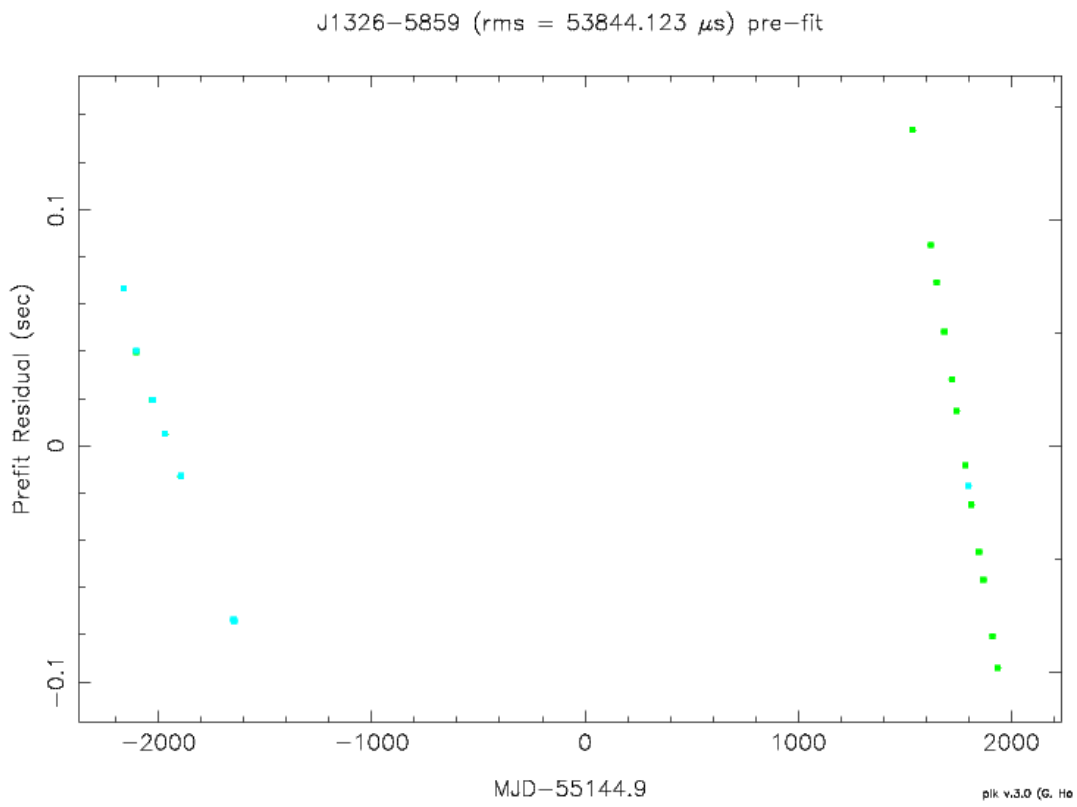

Fig. 5.10: 1300 MHz and 3100 MHz Parkes timing residuals of PSR J1326-5859 showing that the timing noise residual signature is continuing its quasi-periodic nature.

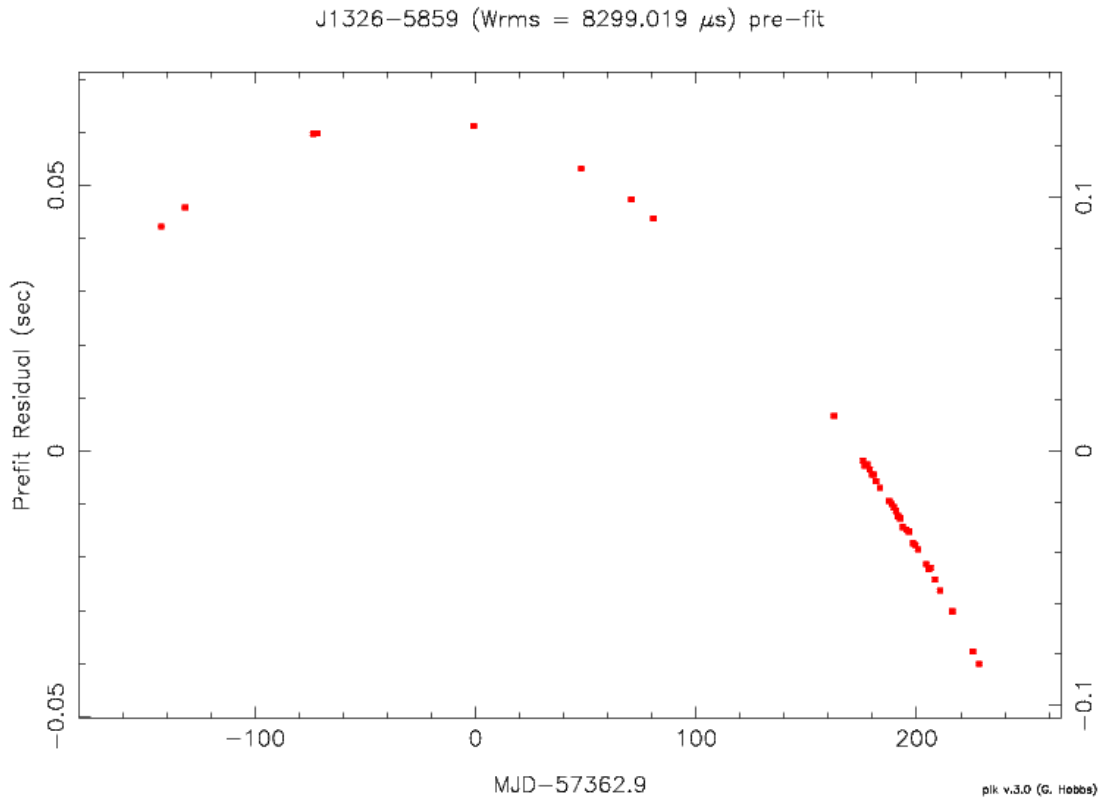

Fig. 5.11: UTMOST 800 MHz timing residuals illustrating that the timing noise signature moved through a crest and are heading for a minimum, thus the timing noise signature remains quasi period.

data and pulse profiles for PSR J1326-5859 retrieved from the Parkes and UTMOST archives can serve as additional reference points within the timing noise signature that was observed using the HartRAO timing data, i.e. in conjunction with the long-term HartRAO timing data that was used in this study, the additional residuals were used to check the timing noise signature's amplitude and quasi-periodic structure at different epochs. All the timing noise signatures (HartRAO, Parkes and UTMOST) of PSR J1326-5859 are consistent both in amplitude and structure.

One can infer several dynamic features from the Gaussian process regression learning that had been done on the long-term HartRAO residuals (ultimately producing the spin-down evolution across several decades) and pulse profiles of PSR J1326-5859 (see Fig.5.9):

- The responsible mechanisms of timing noise are quasi periodic.
- Mechanisms that influence spin-parameters of pulsars are quasi-periodic (stable in some sense).
- The spin-down rate oscillates between two states, between a larger and a smaller spin-down rate.
- The GP regression on residuals and derivatives thereof converged successfully and a model was inferred.
- Phase resolved profile-difference GP regression was performed successfully.
- Correlations exist between variations in spin-down rate, pulse profile and polarization data.
- Radio-emission is quenched quasi-periodically (increasing and decreasing flux of pulses)
- The radio emission is quenched significantly at 53000 MJD that corresponds to a slight decrease in the spin-down rate of PSR J1326-5859.
- Timing residuals that extend beyond the HartRAO data set, shows a continuation of the quasi-periodic nature of the timing noise structure.
- UTMOST residuals have moved through a crest in the residual pattern.
- Parkes residuals appear to be between a maximum and minimum in the timing noise residual pattern.
- Quenching of radio flux can be possibly associated with some level of accretion of plasma from a disk.

The analysis and classification process of the polarization data of PSR J1326-5859 is made difficult since the pulsar exhibits an evolution in the profile domain from 1344 MHz to 3100 MHz. The profile structure at 3100 MHz contains a different profile morphology, see Fig 5.6, with the appearance of an additional third component, where there was no component in the 1344 MHz profile (see Fig.5.2).

PSR J1326-5859 also exhibits a counter-intuitive polarization position angle swing (not to be confused with the polarization vector) that can be seen in the top panel of Fig.5.6 in the sense that the polarization angle swing is not described by the characteristic S-shape swing that is predicted by the rotating vector model (RVM). The polarization angle swing of PSR J1326-5859 is governed by jumps and wiggles and could possibly be due to competing orthogonal modes in the emission region of the pulsar and remains a region of interest for future studies.

In the next chapter the possibility will be investigated whether a fossil disk system is coupled to PSR J1326-5859 that could induce the observed spin-down evolution and polarization changes.

Chapter 6

Interpretation of results

6.1 Justification for choosing the disk model

Non-zero residual patterns in pulsar timing could either be attributed to short term variations in the spin parameters of pulsars that could include glitching and pulse drifting. However these short term variations have prominent residual patterns (see Raithel et al. [77], Palfreyman et al. [67] and Lyne, Smith & Pritchard [58]), none of which match that of PSR J1326-5859. It is clear that the non-zero timing residuals observed in PSR J1326-5859 are due to some long-term effect. These effects include possible GW background detection, presence of a binary companion or possible precession. Residual patterns generated by GW backgrounds are detected with several pulsars in a network and the typical amplitude of such residual pattern will be $\approx$ 1 μs (see Backer & Hellings [4]). PSR J1326-5859 is unlikely associated with a binary system, since no binary system geometry could be found that fits the observed residual pattern of PSR J1323-5859 (see Frescura & Flanagan [31]). It is also highly unlikely that the observed timing residual pattern could be due to precession (see Perera et al. [71] and Perera et al. [70]).

Timing noise can also be observed in both young and millisecond pulsars (see Chukwude [19] and Shannon et al. [85] for examples of timing noise in normal/young and millisecond pulsars respectively). We searched for a model that could possibly unify the combined spin-effects that were observed in the timing data of PSR J1326-5859 (both in the spin-down rate and pulse/magnetospheric variations). We observed that PSR J1326-5859 exhibited quasi-periodic changes in the the pulse flux, spin-down rate and polarization vectors across the entire emission region. Thus, we decided to explore the possibility of whether PSR J1326-5859 could be coupled to a low mass disk that interacts quasi-periodically with the magnetosphere of the pulsar.

Wang [95] explored the fundamentals of disk interaction with compact objects of which the work was extended to pulsars and recently was proposed for Vela (Özsükan

et al. [64]) and to explain the possible spin classes of magnetars (Tong et al. [88]). A stable disk can induce quasi-periodic variations of the spin-down rate of the pulsar by accreting matter onto the pulsar and could possibly also quench the radio emission. The added benefit of exploring the possibility of pulsar-disk interactions, is that polarization vector swings could be induced by reflection of radio emission.

In the next subsection we explore the model parameters of such pulsar-disk system mentioned above and attempt to clarify the observed correlations in the variations of pulse flux, spin-down rate and polarization.

6.2 The Model

Pulsars are rapidly rotating and highly magnetized compact objects that can set the stage for interesting dynamics regarding magnetospheric-disk interactions. Such disks can be formed via supernova explosion fallback (fossil disks) or when companions are consumed through the process of accretion. PSR J1326-5859 does not have any companion associated with it, since the timing residuals do not show any periodic variations. Since the disk has angular momentum associated with it, a systematic interaction of the disk with the pulsar will take place and can generate additional torques on the star that can influence the timing process of the pulsar, since the timing model relies heavily on the spin-down model of the pulsar. The mass and angular momentum of the disk together with the initial magnetic field and spin of the pulsar form the initial parameters of the pulsar-disk system that are based on the interaction between the pulsar's magnetosphere and the rotating disk, see Fig.6.1 for an artist impression of the pulsar-disk system.

Observational evidence of disks around pulsars can be deduced by looking for excess emission in the infrared bands when observing such a candidate, one example of this is the computed emission of PSR 0656+14 that is consistent with the emission of a disk around a pulsar. To model the excess emission from these pulsar-disk systems several authors focused on the modeling of the un-pulsed spectrum of the pulsar in the optical, UV and infrared bands, but it can also occur that the disk can be illuminated by the pulsating X-ray emission in certain accretion power X-ray systems (see e.g. Ballantyne et al. [6]). Wang, Chakrabarty & Kaplan [96] reported a debris disk around an isolated young neutron star, which forms part of the group of neutron stars called the anomalous X-ray pulsars (AXPs). The brightest known AXP is the 8.7 s pulsar named 4U 0142+61 that shows no evidence of binary companions and is bright in X-rays (10^{36} erg s^{-1}). The authors searched the surrounding fields of 4U 0142+61 at 4.5 μm and 8 μm for infrared excess predicted by the X-ray heated fallback disk, see Fig.6.2.

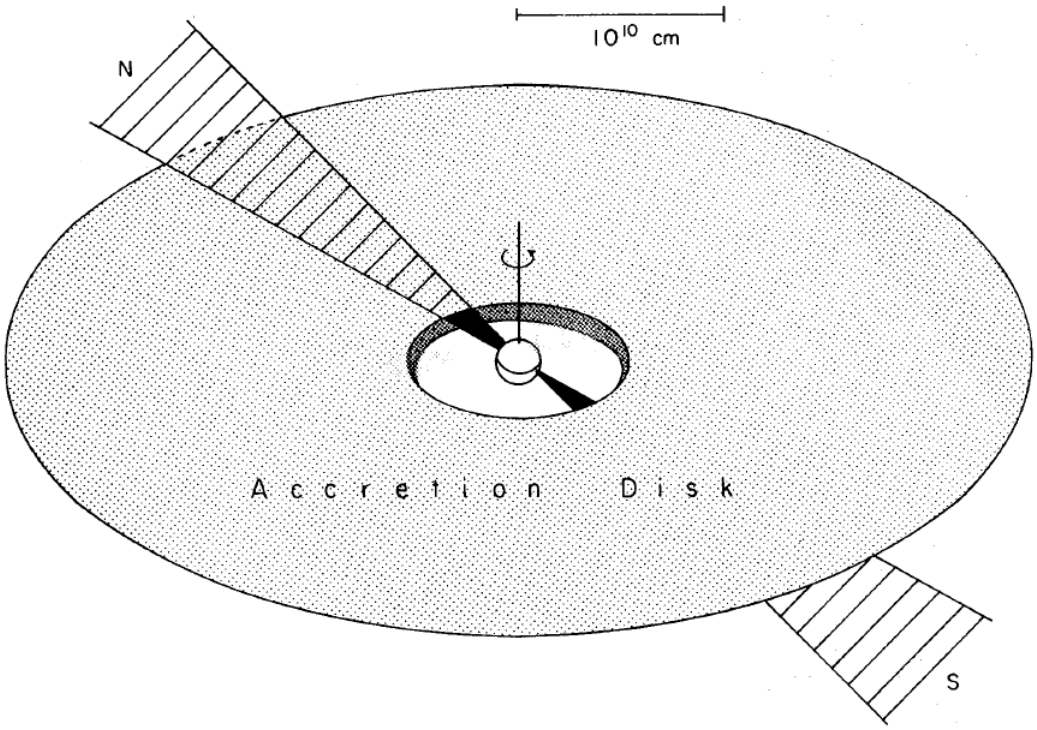

Fig. 6.1: Representation of the pulsar-disk system, the disk contains an inner edge (corresponding to the inner radius of the disk). One pole of the lighthouse can be obscured from the observer. Adopted from Patterson [68]

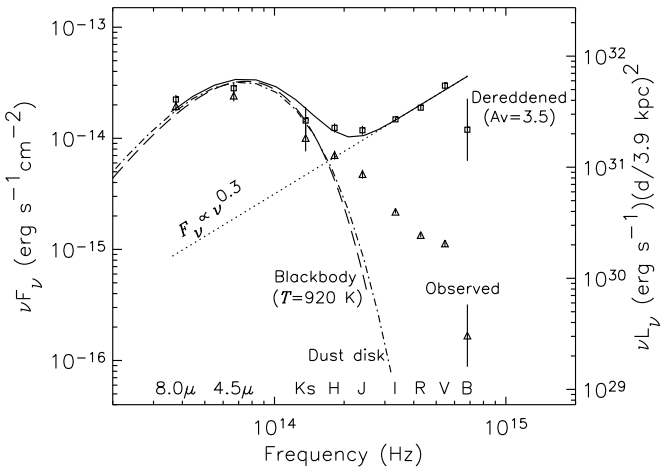

Fig. 6.2: Optical and infrared SED of 4U 0142+61. The dot-dashed curve represents the dust-disk model that includes the irradiation of the X-ray emission. The solid curve represents the summed model consisting of the power-law model and the debris disk model. Adopted from Wang, Chakrabarty & Kaplan [96].

The interactions of the pulsar with the disk can be divided up into two main phenomena, accretion and the propeller phase. Accretion due to the disk takes place where the stresses of the magnetic fields of the pulsar dominate the kinetic energy associated with the accretion flow and material are transported from the disk to the magnetosphere along the magnetic field lines. This transport of material is believed to take place in the vicinity of the the Alfven-radius (see Wang, Manchester & Johnston [93] and references therein):

$$r_A = 3.2 \times 10^8 \dot{M}^{-\frac{2}{7}} \mu^{\frac{4}{7}} \left(\frac{M}{M_\odot} \right)^{-\frac{1}{7}} \text{cm}, \tag{6.1}$$

where $\dot{M}$, μ and M represent the accretion rate (in units of g s^{-1}), magnetic moment (in units of G cm^3) and the mass of the pulsar. To illustrate the concept of the Alfven radius we refer the reader to Fig.6.3. To further illustrate the concept of the pulsar-disk system the reader is referred to Chapter 6 of Frank, King & Raine [29], specifically Figures 6.3 and 6.4 that illustrate a 3D/2D concept of the pulsar's magnetosphere interacting with the disks, see Fig.6.4 and Fig.6.5.

In an attempt to link the spin-down variations seen in the timing noise analysis of PSR J1326-5859 to possible magnetospheric processes that are induced by a fossil disk that could be coupled to PSR J1326-5859, a method is followed along the lines

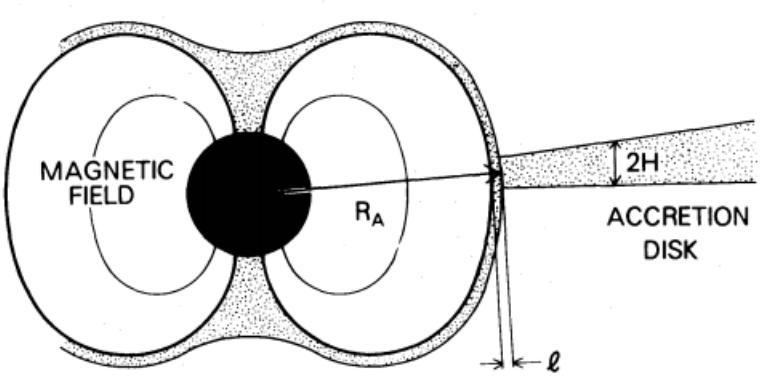

Fig. 6.3: Geometric representation of the Alfven radius, where l is the interaction width determined by the magnetic potential at that point, and H is the disk thickness. Adopted from Ichimaru [42].

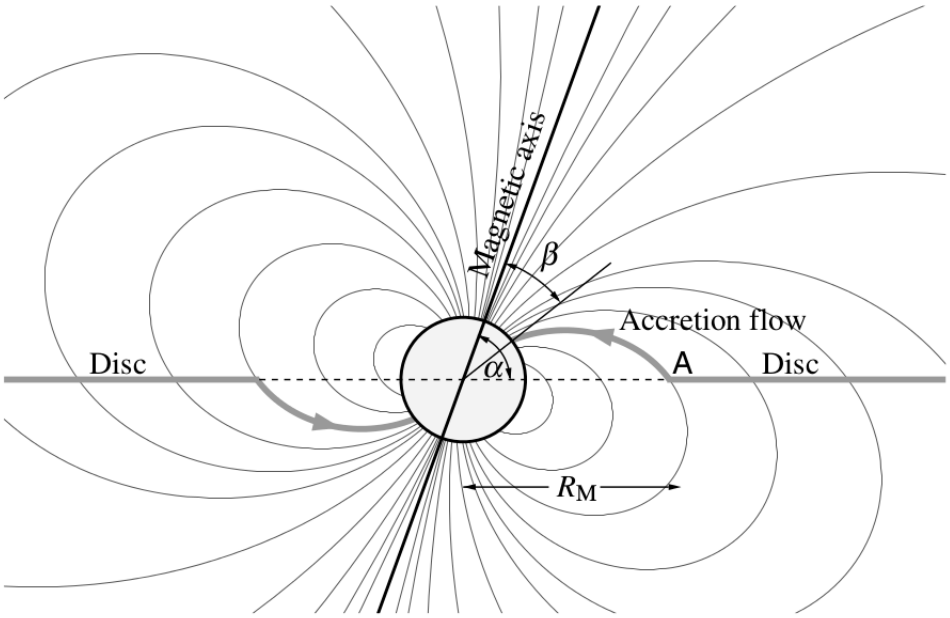

Fig. 6.4: 2D Pulsar-disk setup illustrating the Alfvan radius and geometry of the spinning pulsar, adopted from Frank, King & Raine [29].

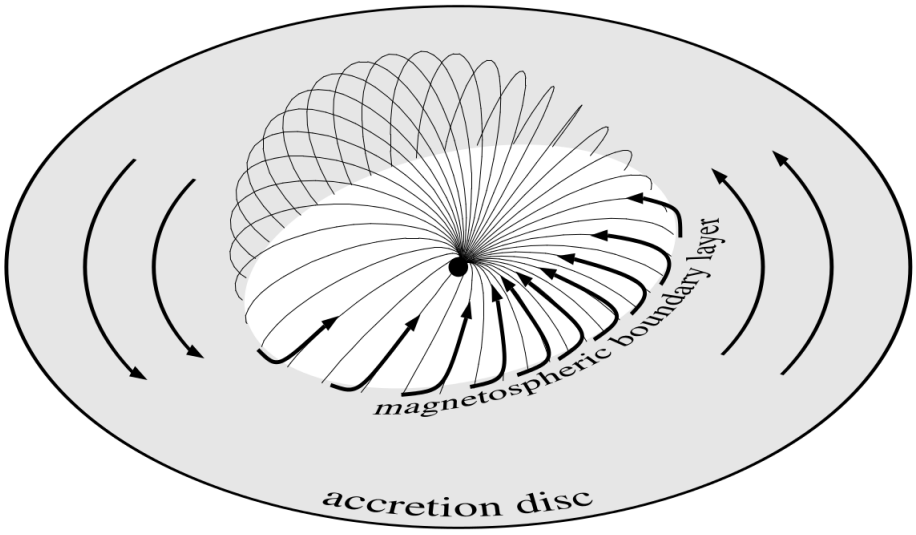

Fig. 6.5: 3D Pulsar-disk setup illustrating the Alfvan radius and geometry of the spinning pulsar, adopted from Frank, King & Raine [29]

of (Wang [95] and Özsükan et al. [64]). Pulsar-disk coupling can occur in isolated pulsar systems, young pulsars and millisecond pulsar systems (see Özsükan et al. [64] and Lasky et al. [51]). It is known that PSR J1326-5859 is an isolated pulsar with no signs of a binary companion, see Hobbs et al. [39] and D'Alessandro et al. [23]. Long-term timing of PSR J1326-5859 reveals prominent timing noise that is quasi-periodic indicating some variation in the spin-parameters of the pulsar.

Using this model, we focused on the total torque that is exerted on the pulsar that consists of the effects of the dipole radiation torque (spinning and radiating neutron star), the presence of the accretion disk and the torque translated to the neutron star via magnetic fields threading the disk (see Fig.6.4). This model relies on the rate of change in the spin-down of the pulsar which can accurately be obtained via pulsar timing.

After fitting the timing noise signature and tracking the spin-down evolution over several decades, it was concluded that the spin-down variations change from a high to a low state and this quasi-cyclic change in spin-down could be due to the evolution of a disk that interacts with the magnetosphere of the pulsar. The hypothesis stated above is based on the fact that the disk can extend partially across the co-rotation radius of the pulsar and that the disk originates from supernovae explosion fall-back material or debris swept up by the pulsar as it is moving through the ISM.

Before setting up the pulsar-disk coupling problem, the physical parameters of such

system need to be defined. The following parameters are assumed: period of pulsar $P = 0.478$s, $\dot{\nu} \approx -1.4151 \times 10^{-14}$ s^{-2}, $\ddot{\nu} \approx -6.249 \times 10^{-26}$ s^{-3}, co-rotation radius $R_c \approx 1.026 \times 10^8$ cm, radius of the neutron star $a \approx 10^6$ cm, mass of the pulsar $M \approx 2.8 \times 10^{33}$ g, moment of inertia $I \approx 10^{45}$ g.cm^2, polar cap radius of $R_{pc} \approx 2 \times 10^4$ cm and a magnetic field strength of $B \approx 10^{12}$ G. Furthermore, it was assumed that the radio emission is coupled with a magnetic dipole structure with a moment of

$$\mu = \frac{Ba^3}{2} \approx 0.5 \times 10^{30} \text{ G cm}^3 \left(\frac{B}{10^{12}\text{G}}\right) \left(\frac{a}{10^6\text{cm}}\right)^3. \tag{6.2}$$

Following along the lines of Brook et al. [11], the total transfer of mass can be calculated for the state changing event seen in the spin-down variation of PSR J1326-5859. If we assume some mass accretion for a period of ≈1000 d between spin-down states (see Fig.5.9), it must bring forth a change in charge density in the pulsar's magnetosphere of

$$\rho = \frac{3I\Delta|\dot{\nu}|}{R_{\text{pc}}^4 B}, \tag{6.3}$$

which translates to a total mass of 10^{19}g in 1000d, or $\dot{M} \approx 10^{11}$ g s^{-1}. Furthermore, if $\Delta\dot{\nu} > 0$ the system will be in a spin-up state and if $\Delta\dot{\nu} < 0$ then the system will be in a spin-down state.

The pulsar-disk system can now be constructed using the inferred parameters that were proposed above. The total torque on the pulsar can be computed by using the accurately observed spin-down of the pulsar,

$$\dot{J}_{\text{tot}} = 2\pi I\dot{\nu}, \tag{6.4}$$

There exist two distinct torques for the two states of $\dot{\nu}$ (see Part A and Part B discussed in the caption of Fig.5.9) that were estimated from the spin-down evolution of PSR J1326-5859, namely for the spin states of $\dot{\nu}_{\text{A}} \approx -1.420 \times 10^{-14}$ s^{-2} and $\dot{\nu}_{\text{B}} \approx -1.4 \times 10^{-14}$ s^{-2}, the corresponding torques are $\dot{J}_{\text{A}} \approx -8.922 \times 10^{31}$g cm^2 s^{-2}

and $\dot{J}_{\rm B} \approx -8.796 \times 10^{31}$ g cm^2 s^{-2}.

The torque contribution due to dipole radiation that is associated with the spinning dipole is (Wang [95])

$$\dot{J}_{\rm mdr} = -\frac{8\pi^3\mu^2}{c^2}\nu^3(1+\sin^2\eta), \tag{6.5}$$

which for PSR J1326-5859 corresponds to $\dot{J}_{\rm mdr} = -3.937 \times 10^{31}$ g cm^2 s^{-2}. Thus, the total torque exerted on the neutron star itself is

$$\dot{J}_{\rm total} = \dot{J}_{\rm mdr} + \dot{J}_{\rm disk}, \tag{6.6}$$

resulting in two possible values for the disk contribution to the torque on the neutron star (in units of g cm^2 s^{-2})

$$\dot{J}_{\rm disk}(A) = -4.985 \times 10^{31}, \tag{6.7}$$

and

$$\dot{J}_{\rm disk}(B) = -4.859 \times 10^{31}. \tag{6.8}$$

Now the disk torque contribution can be decomposed into the contribution of the mass accretion regime and the propeller regime, that is

$$\dot{J}_{\rm disk} = \dot{J}_{\rm accretion} + \dot{J}_{\rm propeller}, \tag{6.9}$$

According to Wang [95] the total torque can also be written as a function of $x_0 = \frac{R_0}{R_c}$, where $R_c = \left(\frac{GM}{\Omega^2}\right)^{\frac{1}{3}}$ is the co-rotation radius of the pulsar and R_0 is the inner radius of the disk. This is

$$\dot{J}_{\text{disk}} = \left(\dot{M}_{\text{disk}} \left(GMR_c\right)^{0.5} x^{0.5}\right) \left(1 + \frac{2}{9x_0^{\frac{9}{80}}}\right). \tag{6.10}$$

Using the two possible extreme torque contributions of the disk $\left(\dot{J}_{\text{disk}}\right)$ on the neutron star, the corresponding values for x_0 were found to be,

$$x_0(A) = 0.9715, \tag{6.11}$$

for $\dot{J}_{\text{disk}} = -4.985 \times 10^{31}$, and

$$x_0(B) = 0.9711, \tag{6.12}$$

for $\dot{J}_{\text{disk}} = -4.859 \times 10^{31}$.

Both the computed values for x_0 that represent the average values of the inner edge of the disk relative to the co-rotation disk, indicate that the system is stable and in a spin-down stage, which correlates well with the observed spin-down evolution of PSR J1326-5859 (see Fig.5.9). Any change in the average value of x_0 translates to a change in the accretion rate that could be tracked with multi-wavelength observations of PSR J1326-5859. For a pulsar-disk system that is in equilibrium $x_0 = 0.971$, see Wang [95] for a complete classification of x_0.

This solution compares well to the solutions that were obtained for several binary X-ray pulsars (SMC X-1, Her X-1, Cen X-3 etc.) by Wang [95].

The origin of the disk can be due to either accreting the matter from a companion

star or forming the disk by fall-back material after a supernova explosion in which the neutron star is born. However, PSR J1326-5859 did not exhibit any orbital modulation due to the presence of a binary companion. The inner radius of the disk remains close to the co-rotation radius of the magnetosphere and does not shift dramatically. The inner radius of the disk oscillates between $R_{in} \leq 0.9715R_c$ and $R_{in} \leq 0.9711R_c$ which are associated with the two extreme spin-down rates of PSR J1326-5859. The observed oscillation of the inner radius of the disk could be explained by the model of accretion disks with the inner disk radii extending to radii inside co-rotation radius of the pulsar. Assuming low accretion rates and a strong magnetic field that are associated with the pulsar; the pulsar truncates the disks close to the star and matter accretes along the closed magnetic field lines onto the pulsar. The pulsar's magnetic field structure becomes entangled at the interaction region, but different to that of pulsars being dramatically spun-up by disks formed by accreting companions; the magnetic re-connection in these fossil disk systems could be less dramatic with less energetic outburst (see D'Angelo & Spruit [24]).

In summary, our model relies on a pulsar coupled to a low mass disk that interacts strongly with the pulsar in the vicinity of the co-rotation radius. The inner radius of the disk remains close to co-rotation radius and oscillates between two values in a stable manner to produce the two extreme spin-down rates that can be accurately observed via pulsar timing. The characteristics of this particular model (spin-period, magnetic field strength of the pulsar) support non-violent X-ray/radio bursts since the re-connection events are not as energetic as AXP-systems. However, enough disk material can be accreted to partially quench normal radio emission in a cyclic manner that if tracked over time, can be correlated with spin-down rate variations. Our model assumes the inner radius of the disk remains close to the co-rotation radius of the disk in a trapped state, i.e. the pulsar disk system does not exhibit extreme variations between full-accretion state and full propeller state. This scenario will ultimately produce small variations in spin down rate that could be correlated with variations in pulse profiles (emission model) that can ultimately suggest a model for timing noise.

However, how likely is it that the normal pulsar PSR J1326-5859 can have a disk associated with it? After the supernova explosion that creates the spinning neutron star, there exist only three known varieties for the newly born neutron star: firstly, the neutron star can be born without any debris disk associated with it, secondly, the neutron star can be born with a fallback disk, that can influence the neutron star's torque and occasionally give rise to accretion onto the compact object, lastly, full-accretion on the compact object from a companion producing an X-ray source; in this case enough material is injected into the polar cap regions that can give rise

to hot-spots by bulk motion and thermal comptonization. It is known through observations of planets around PSR 1257+12 and the disk around 4U 0142+61, that pulsar and disk interactions play an important role in pulsar spin-down and the quenching of emission in the pulsar's magnetosphere, naturally leading to a search for correlations between the pulsar's spin-down history and magnetosphere conditions.

Disk interactions with rapidly rotating neutron stars can also be found in the extreme case of magnetars spinning in the presence of a fall back disk (Tong et al. [88]). From the dynamics of the pulsar-disk model, an extreme characteristic of the magnetar-disk system can be identified, namely the extremely large magnetic field that is associated with the magnetar (up to $\approx 10^{16}$G, see e.g. Tong et al. [88]). The combination of the magnitude of the magnetic field of the magnetar and the mass of the disk sets the stage for possible strong disk interactions that produce certain dynamical spin-down scenarios. If the mass of the disk is smaller than $10^{-6}M_{\odot}$, the interaction of the magnetar and the disk is kept to a minimum and the magnetar remains as predicted with no abnormal spin-down variations. If the disk mass is large but the dipole field strength of the magnetar is smaller than 10^{14}G, the magnetar will spin-down as predicted. However, if the disk mass is large and the magnetar has a significant magnetic field strength, then the magnetar could be slowed down quickly to abnormally long rotational periods. This could explain the super-slow magnetar in the supernova remnant RCW 103 (Tong et al. [88]). The models constructed and used in the works of Tong et al. [88], Shannon et al. [85], Wolszczan & Frail [97], Brook et al. [10] and Özsükan et al. [64], clearly illustrate the importance of neutron star disk interactions and the implications of explaining the possible variations seen in the timing of certain pulsars, especially along the lines of variations in the spin-parameters of the pulsars.

Models of precession and binary companions are discarded for explaining the possible spin-down variations observed in PSR J1326-5859 since the timing residuals do not reflect what is expected for binary companions, which is, periodic variations in the timing residuals of the pulsar. This lead us to introduce an hypothesis that states that fossil disk interaction with pulsars can only be observed and modeled through the process of pulsar timing and by applying machine learning to the long-term residuals of the particular pulsars that exhibit quasi-periodic timing noise signatures.

The reader's attention is turned to the polarization vector swings that were observed in the 3100 MHz Parkes polarization data of PSR J1326-5859 (see Fig.5.8). Interesting phenomena were observed in the form of the polarization vector changing by 180 degrees during the episodic spin-down state changing of PSR J1326-5859 (from 53174 to 53249 MJD). It was concluded that the change in the polarization vector

can not be due to the presence of orthogonal polarization modes (no OPM were detected in the phase bins selected), but rather due to a mechanism that added to the total polarization mode. A primary candidate for the latter mentioned mechanism was considered to be the reflection of the beams from the fossil disk, see Fig.6.1 for a visual demonstration of the disk-reflection model. PSR J1326-5859 does not exhibit an inter-pulse as part of the average folded pulse and supports the hypothesis that one of the poles of the pulsar is obscured by a disk (Patterson [68]). As PSR J1326-5859 transcends from one spin-down state to another, the beam could get wobbled along the line of sight with the effect of the reflected emission produced by the obscured beam being reflected from the inner part of the disk along the line of sight, becoming either more or less prominent as the beam wobbles. Since the polarization properties of the main emission and reflected emission differ by 180 degrees, it could possibly explain the observed polarization changes observed in PSR J1326-5859, specifically the global polarization swing observed across the on-pulse region from 53174 to 53249 MJD. See Fig.6.6 for an artist impression of the pulsar-disk model and the induced polarization changes.

In the future astronomers need to take into account that the latest discoveries that challenges the current model; transitional millisecond pulsars (such as XSS J12270-4849 and PSR J1023+0038) that show transitions between being X-ray powered pulsars and classic rotational power radio pulsars. It will be interesting to attempt to unify these sources with our current disk model.

Further investigations and calculations still need to be performed to answer the question of how the disk survives for the time span of the pulsar's age and what mechanism replenishes the accreted matter from the disk, since we observe evidence of accretion in the form quasi-periodic radio quenching (see Fig.5.9) . Furthermore, it needs to be investigated whether these pulsar-disk systems are unique or whether they perhaps form part of the larger pulsar population. The study will be concluded in the next chapter.

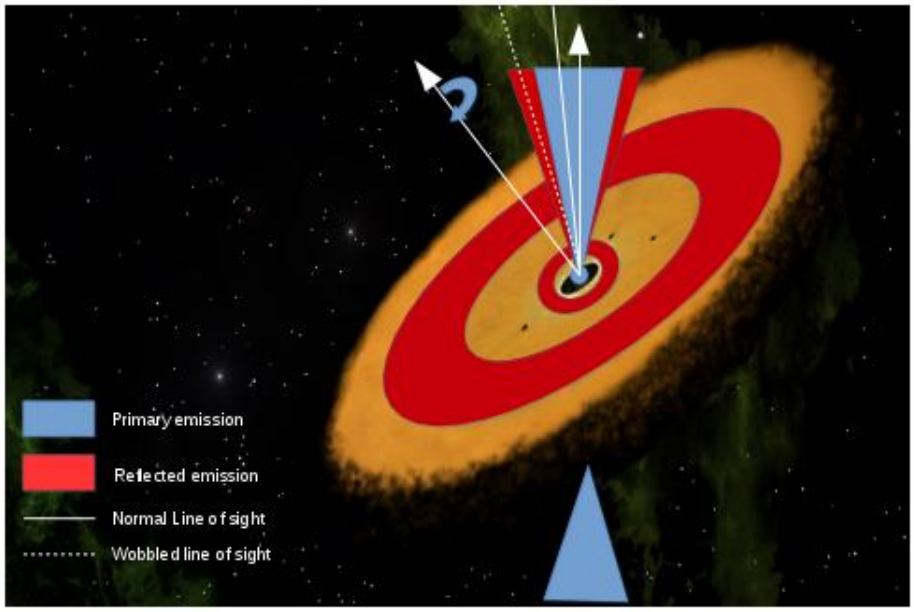

Fig. 6.6: Artist impression of the proposed timing noise model for PSR J1326-5859. Spin-down changes in the pulsar could possibly be due to the presence of a disk that wobbles the beam and changes the polarization mode along the line of sight, ultimately leading to spin-variation that induces timing noise. A key ingredient to these observed polarization swings are reflected emission from the inner parts of the disk due to the obscured beam or due to the primary beam being reflected from the surrounding dense disk region. Adapted from www.nasa.gov, image credit: Jonathan Holden.

Chapter 7

Conclusion

After accounting for contributions from the spin-down of pulsars (primarily through using the pulsar timing model), their variations in astrometric parameters and prominent orbital variations, the excess residuals can be classified as timing noise. Timing noise signatures are very similar to the signal that astronomers suspect pulsar timing arrays to observe from gravitational wave sources. Thus, ironing out the possible mechanisms for timing noise could facilitate the process of finding gravitational waves with the use of timing arrays.

Timing noise residual patterns can be seen in long term timing campaigns of normal and millisecond pulsars and set the stage for many possible interpretations of which almost all the explanations rely on spin-variations of the neutron star itself, induced by some internal or external mechanism (e.g. precession, beam wobbling, mode switching or disk interaction). This work focused on the model that describes an external mechanism that could induce the observed spin-variations and magnetospheric emission conditions observed in PSR J1326-5859 in a systematic and stable manner. In this study it has been shown that the long-term spin-down variations of PSR J1326-5859 can be reconciled with the interaction of the rapidly rotating neutron star with a fossil disk. Regression methods (based on machine learning) were implemented to find the spin-down rate evolution of PSR J1326-5859 in an continuous manner and to correlate the variations with any shape changes in the profiles of PSR J1326-5859 over decades. It needs to be stressed that timing noise can be completely modelled using a red noise spectrum, and can be removed (the residuals can be whitened). However, for the purpose of extracting astrophysical phenomena and models from surplus timing residuals, it remains useful to try to carefully re-construct the timing noise signature with the aim of calculating the spin-down evolution of the pulsar and correlate it with pulse profile and polarization data.

Considering the pulsar-disk system in general and its dynamics for explaining some of the timing noise signatures seen in millisecond and normal pulsars, sets the stage

for possibly reconstructing the timing noise signatures observed in long-term pulsar timing data. Specifically, addressing the uniqueness of the quasi-periodic structure seen in certain pulsar's timing noise signatures. Each pulsar is unique in the sense of its magnetic field strength and spin-dynamics (spin-down, spin-down rate, glitches, burst-events, etc.) and the interactions of these parameters with a possible disk can effect the net torque that is exerted on a rapidly rotating spinning neutron star. It should be stressed that internal neutron star effects, such as glitches, possible star precession and the presence of companions will produce residuals with characteristic periodic timing residuals and can be identified quickly. However, the neutron star precession model remains a competing model to disk interactions, but have drawbacks along the lines of sustainability of the precession process and the detectability of observable consequences (for example minute pulse profile shape changes or spin-down rate variations due to precession).

Pulsar-disk systems and precession models share a common domain whereby a pulsar with a disk could induce and sustain a wobbling effect on the neutron star, that ultimately rocks the pulsar beam slightly and produces correlated spin and magnetospheric variations. The rocking of the pulsar's beam is caused by the miss-alignment of the angular momentum of disk and the angular momentum of the neutron star (similar to attempting to twist a spinning bicycle wheel perpendicular to the plane of rotation), thus, if the observer's line of sight is fixed the beam will slightly wobble across the observer's line sight. Both models also share difficulties in the domain of direct detection; physically detecting the disk requires sensitive measurements of IR excess and the effect of precession could go undetected due to observation time or hardware sensitivity limitations.

The possible astrophysical models that could describe the timing noise phenomena remain tantalizing and the software development that goes with it, equally so. In the past few years pulsar astronomers have moved over to interpreting timing residual patterns using sub fields of machine learning techniques, that can perform smart regression by using parts of the timing noise residual pattern to fit the features in a continuous manner with the necessary confidence levels. Particularly, the machine learning codes of interest will be those that were used in this study, which were GaPP (primary source), Vgp (primary source), Scikit learn (secondary source) and TensorFlow (secondary source); all of which remain open source and can be adapted for the purposes of regression of timing data in pulsar astronomy. In the near future, timing noise residual patterns will become densely populated with the added benefit of wideband data, thus the need for machine learning regression algorithms to extract the spin variations from the timing residuals, will become important. Individual timing noise residuals of specific pulsars will also be added

on a daily basis as part of timing array campaigns, which will require a dynamic real-time regression and classification pipeline to ultimately classify the spin-state of the pulsar in real-time (which could improve the stability of the astrophysical clock).

With modern day telescopes enabling us to observe large bandwidth radio signals simultaneously, a future observational campaign for PSR J1326-5859 may include several deep observations (to implement the study of radius to frequency mapping), single pulse observations, an continuation of the long term timing program and a complete high resolution study of the polarization properties of the phase resolved profiles, i.e. plotting the calibrated polarization vector to check for any change/swings in the polarization data of the radio emission and possible orthogonal polarization modes. Long-term single pulse observations of PSRJ1326-5859 with meerKAT could also shed light on profile and polarization mode evolution in accordance with the pulsar's spin-down rate. Given that the profile shape and the spin-down history of PSR J1326-5859 change over several hundred days (see Fig.5.9), it could be helpful to map the polarization vector with a weekly cadence and being absolutely calibrated.

It was showed that PSR J1326-5859 exhibits nearly quasi-periodic timing noise residuals that translate to a spin-down history ($\dot{\nu}$) which is switching between two spin-down modes and could be due to the interaction of the pulsar with a disk. The Parkes 3100 MHz polarization data show a change in the polarization vector as the pulsar transcends from one spin-down mode to another, possibly being evidence of reflected emission of the obscured beam from the disk and the reflection of the primary beam from the dense material in the surrounding disk. The disk can also wobble the primary beam along a fixed line of sight, ultimately changing the total composition of the polarization mode along the line of sight.

The most interesting part of this particular field will be to have enough multi-wavelength observational evidence to classify the pulsar as a disk system by using its timing noise residuals to map the spin-down rate of the pulsar in real-time followed by inferring the disk parameters, thus possibly creating an unique technique to detect fossil disks of moderate mass around normal pulsars. It was illustrated that the polarization vector swings could possibly be used as a diagnostic tool to discover the presence of a disk due to the reflection of pulsed emission from the dense parts of the disk.

With MeerKAT antennas and its state of the art backends being on the brink of deployment and testing, it still remains a key science goal to understand timing

noise and building a trustworthy platform for possible GW studies in the next few decades. The interpretation of polarization data will become key in the field of tracking the dynamics of pulsars and machine learning can easily assist with mining this avenue (particularly phase resolved polarization studies of large collections of data). What needs to be implemented within the next few years particularly for observational campaigns of pulsars that exhibit timing noise residuals, will be to construct a pipeline that can simultaneously track the timing residuals of the pulsar, produce the spin-down state of the pulsar, classify single pulses as usable or anomalies, retrieve the polarization vector, track the polarization vector of the pulsar and, if possible, track the dynamics of the disk that is torquing the star. This scheme can be implemented with relative ease by using both classifiers and regression machines that can be encapsulated within the MeerKAT's pulsar analysis system. The direct detection of pulsar disks with MeerKAT will ultimately depend on the high frequency observation capabilities of the instrument, e.g. current projections for the X-band receiver is based on a RF frequency range of 8 GHz -14.5 GHz which will be down-converted to a 1 GHz processing IF band with system temperature not exceeding 30 K with an estimated sensitivity of 200 m^2/K. The polarization studies performed in this work can be applied to an calibration pipeline of pulsar data associated with the MeerKAT antennas; tracking the projection of the phase preserved polarization vector from one pulse to the next and classifying any change in the state of the polarization vector as either inherent to the pulsar or due to external mechanisms such as the ISM or due to instrumental features.

The polarization properties are already known for archival pulsars and can be used to match the observed Stokes parameters to the known template of the instrumental parameters to build the Jones matrix to automatically calibrate the polarization data. The Poincare spheres can be checked to track the stability of the polarization vector and infer possible pulsar-disk parameters.

With the increased data rates and storage capabilities of modern instruments and telescopes, it is becoming a fundamental strategy to apply machine learning techniques to the massive amounts of valuable astrophysical data. Machine learning in particular will help astronomers to quickly act upon dynamic and interesting astrophysical sources and will enable them to quickly assess the quality of the recorded data to construct an analysis strategy. It was shown in this study that machine learning techniques could also be used to infer new astrophysical models from data that could help improve fundamental models associated with pulsar dynamics and beam polarization. The timing noise phenomena seen in several pulsars could be used as an indirect method for the detection of possible pulsar-disk interactions, otherwise difficult to detect directly. Tracking the attributes (and their errors) of

pulsars in a correlated manner using machine learning techniques, could enable astronomers to deduce useful information from data which if analyzed independently would not have produced useful results. As part of the future prospects of this study we could expand the regression technique of the timing residuals to include Neural Networks (a more robust unsupervised learning technique) and possible classification techniques for the variability of pulsar profiles and polarization vectors from epoch to the next. The Neural Network can specifically be created for the purposes of detecting outlier polarization vector swings among an extensive sequence of polarization vector data spanning the entire phase bin of the pulse. The Neural Network could also search for phase correlations between polarization swings and truly ingest each phase bin's worth of data.

Finally, we perform a crude estimation of the observation time needed to detect PSR J1326-5859 using one MeerKAT antenna. We use the radiometer equation to determine the observation time for the target of 10 mJy and a S/N of 10. The system noise of a MeerKAT antenna is taken to be 30 K with a gain of $G \approx 0.033$ K/Jy and dual polarization. Knowing that the duty cycle of PSR J1326-5859 is 4.82 percent and we observe at the frequency of 1.3 MHz, the total observation time needed is limited to 26 seconds using one 13.5 m MeerKAT antenna. It is clear that PSR J1326-5859 could serve as a prime candidate for follow-up observations using MeerKAT.

Acknowledgements

I hereby acknowledge and express my sincere gratitude to the following parties for their valuable contributions:

- Prof. P.J. Meintjes for his role as supervisor, and for all the encouragement and valuable guidance that I have received from him the past 7 years.
- The Department of Physics at the University at the Free State and in particular the head of department Prof Koos Terblans and the former head of department Prof Swart.

And above all, all honor and praise to our Heavenly Father, who grants us the privilege to explore the wonders of his creation. To my wife, Elizabeth, thank you for everything.

This research has made use of NASA's Astrophysics Data System. Software used in this study include: TEMPO, Psrchive, GaPP and Vgp. Also Scikit-learn and Tensorflow packages were used as secondary testing machine learning codes.

Bibliography

[1] Abdo A. A. et al., 2009, ApJ, 696, 1084

[2] Arzamasskiy L., Philippov A., Tchekhovskoy A., 2015, ArXiv e-prints,1504.06626

[3] Backer D. C., 1970, Nature, 227, 692

[4] Backer D. C., Hellings R. W., 1986, ARAA, 24, 537

[5] Backer D. C., Kulkarni S. R., Heiles C., Davis M. M., Goss W. M., 1982, Nature, 300, 615

[6] Ballantyne D. R., Purvis J. D., Strausbaugh R. G., Hickox R. C., 2012, The Astrophysical Journal, Letters, 747, L35

[7] Beck R., 2015, Astronomy and Astrophysics, 578, A93

[8] Becker W., 2009, Neutron stars and pulsars. Springer, Berlin

[9] Becker W., Truemper J., 1997, Astronomy and Astrophysics, 326, 682

[10] Brook P. R., Karastergiou A., Buchner S., Roberts S. J., Keith M. J., Johnston S., Shannon R. M., 2014, ApJ, 780, L31

[11] Brook P. R., Karastergiou A., Buchner S., Roberts S. J., Keith M. J., Johnston S., Shannon R. M., 2014, ApJL, 780, L31

[12] Brook P. R., Karastergiou A., Johnston S., Kerr M., Shannon R. M., Roberts S. J., 2016, Monthly Notices of the Royal Astronomical Society, 456, 1374

[13] Burgay M. et al., 2003, Nature, 426, 531

[14] Burke B., 2010, An introduction to radio astronomy. Cambridge University Press, Cambridge New York

[15] Camenzind M., 2005, Compact Objects in Astrophysics: White Dwarfs, Neutron Stars and Black Holes (Astronomy and Astrophy. Springer-Verlag Berlin and Hei

[16] Cerutti B., Mortier J., Philippov A. A., 2016, Monthly Notices of the Royal Astronomical Society, 463, L89

[17] Chen J. L., Wang H. G., 2014, The Astrophysical Journal Supplement Series, 215, 11

[18] Cheng K. S., Ho C., Ruderman M., 1986, The Astrophysical Journal, 300, 500

[19] Chukwude A. E., 2007, CJAA, 7, 521

[20] Condon J. J., 2016, Essential radio astronomy. Princeton University Press, Princeton

[21] Cordes J. M., Helfand D. J., 1980, ApJ, 239, 640

[22] D'Alessandro F., Deshpande A. A., McCulloch P. M., 1997, Journal of Astrophysics and Astronomy, 18, 5

[23] D'Alessandro F., McCulloch P. M., King E. A., Hamilton P. A., McConnell D., 1993, Monthly Notices of the Royal Astronomical Society, 261, 883

[24] D'Angelo C. R., Spruit H. C., 2012, Monthly Notices of the Royal Astronomical Society, 420, 416

[25] De K., Gupta Y., 2016, Experimental Astronomy, 41, 67

[26] De K., Gupta Y., 2016, Experimental Astronomy, 41, 67

[27] Dolch T. et al., 2014, ArXiv e-prints

[28] Fender R., 2012, in IAU Symposium, Vol. 285, New Horizons in Time Domain Astronomy, Griffin E., Hanisch R., Seaman R., eds., pp. 11–16

[29] Frank J., King A., Raine D., 2002, Accretion Power in Astrophysics:, 3rd edn. Cambridge University Press, Cambridge

[30] Frescura F., Flanagan C. S., 2003, in Astronomical Society of the Pacific Conference Series, Vol. 302, Radio Pulsars, Bailes M., Nice D. J., Thorsett S. E., eds., p. 237

[31] Frescura F., Flanagan C. S., 2003, 302, 237

[32] Ghisellini G., 2013, Radiative Processes in High Energy Astrophysics (Lecture Notes in Physics). Springer

[33] Gil J., Rudnicki W., 1985, Astronomy and Astrophysics, 147, 184

[34] Goldreich P., Julian W. H., 1969, ApJ, 157, 869

[35] Górski K. M., Hivon E., Banday A. J., Wandelt B. D., Hansen F. K., Reinecke M., Bartelmann M., 2005, ApJ, 622, 759

[36] Hankins T. H., Rickett B. J., 1975, Methods in Computational Physics, 14, 55

[37] Hecht E., Zaj, 1974, Optics, World student series. Addison-Wesley Pub. Co.

[38] Hewish A., Pilkington J. D. H., Bell S. J., Cole T. W., 1968, Nature, 218, 126

[39] Hobbs G. et al., 2004, Monthly Notices of the Royal Astronomical Society, 352, 1439

[40] Hobbs G., Lyne A. G., Kramer M., 2010, MNRAS, 402, 1027

[41] Hulse R. A., Taylor J. H., 1975, ApJ, 195, L51

[42] Ichimaru S., 1978, The Astrophysical Journal, 224, 198

[43] Igoshev A. P., Popov S. B., 2013, Monthly Notices of the Royal Astronomical Society, 434, 2229

[44] Jansky K. G., 1933, Nature, 132, 66

[45] Johnston S., Karastergiou A., Willett K., 2006, Monthly Notices of the Royal Astronomical Society, 369, 1916

[46] Karastergiou A., Johnston S., 2007, Monthly Notices of the Royal Astronomical Society, 380, 1678

[47] Kerr M., Hobbs G., Johnston S., Shannon R. M., 2016, Monthly Notices of the Royal Astronomical Society, 455, 1845

[48] Kerr M., Ray P. S., Johnston S., Shannon R. M., Camilo F., 2015, ApJ, 814, 128

[49] Kraus J. D., 1966, Radio astronomy

[50] Lai D., Chernoff D. F., Cordes J. M., 2001, ApJ, 549, 1111

[51] Lasky P. D., Melatos A., Ravi V., Hobbs G., 2015, Monthly Notices of the Royal Astronomical Society, 449, 3293

[52] Li L., Guo L., Wang G.-L., 2016, Research in Astronomy and Astrophysics, 16, 58

[53] Longair M. S., 2011, High Energy Astrophysics. Cambridge University Press

[54] Lorimer, Kramer, 2005, Handbook of pulsar astronomy. Cambridge University Press, Cambridge, UK New York

[55] Lyne A., Hobbs G., Kramer M., Stairs I., Stappers B., 2010, Science, 329, 408

[56] Lyne A. G., 1971, Monthly Notices of the Royal Astronomical Society, 153, 27P

[57] Lyne A. G., Manchester R. N., 1988, mnras, 234, 477

[58] Lyne A. G., Smith F. G., Pritchard R. S., 1992, Nature, 359, 706

[59] Manchester R. N. et al., 2013, Publications of the Astronomical Society of Australia, 30, e017

[60] Manchester R. N., Hobbs G. B., Teoh A., Hobbs M., 2005, VizieR Online Data Catalog, 7245, 0

[61] Michel F. C., 1994, The Astrophysical Journal, 431, 397

[62] Naidu A., Joshi B. C., Manoharan P. K., Krishnakumar M. A., 2015, Experimental Astronomy, 39, 319

[63] Osłowski S., van Straten W., Bailes M., Jameson A., Hobbs G., 2014, Monthly Notices of the Royal Astronomical Society, 441, 3148

[64] Özsükan G., Ekşi K. Y., Hambaryan V., Neuhäuser R., Hohle M. M., Ginski C., Werner K., 2014, The Astrophysical Journal, 796, 46

[65] Pacholczyk A. G., 1970, Radio astrophysics. Nonthermal processes in galactic and extragalactic sources

[66] Pacini F., 1967, Nature, 216, 567

[67] Palfreyman J. L., Dickey J. M., Ellingsen S. P., Jones I. R., Hotan A. W., 2016, ArXiv e-prints

[68] Patterson J., 1979, Astrophysical Journal, 234, 978

[69] Perera B. B. P., Stappers B. W., Weltevrede P., Lyne A. G., Bassa C. G., 2015, Monthly Notices of the Royal Astronomical Society, 446, 1380

[70] Perera B. B. P., Stappers B. W., Weltevrede P., Lyne A. G., Bassa C. G., 2015, Monthly Notices of the Royal Astronomical Society, 446, 1380

[71] Perera B. B. P., Stappers B. W., Weltevrede P., Lyne A. G., Rankin J. M., 2015, ArXiv e-prints

[72] Pratap P., McIntosh G., 2005, American Journal of Physics, 73, 399

[73] Punsly B., Coroniti F. V., 1990, The Astrophysical Journal, 354, 583

[74] Pétri J., 2011, Monthly Notices of the Royal Astronomical Society, 412, 1870

[75] Pétri J., Dubus G., 2011, Monthly Notices of the Royal Astronomical Society, 417, 532

[76] Radhakrishnan V., Cooke D. J., Komesaroff M. M., Morris D., 1969, Nature, 221, 443

[77] Raithel C. A., Shannon R. M., Johnston S., Kerr M., 2015, ArXiv e-prints

[78] Rankin J. M., 1993, ApJ, 405, 285

[79] Rookyard S. C., Weltevrede P., Johnston S., Kerr M., 2016, ArXiv e-prints

[80] Ruderman M. A., Sutherland P. G., 1975, The Astrophysical Journal, 196, 51

[81] Rybicki, Lightman, 1979, Radiative Processes in Astrophysics. Wiley

[82] Sanchez D. A., Deil C., 2013, ArXiv e-prints

[83] Seikel M., Clarkson C., Smith M., 2012, Journal of Cosmology and Astroparticle Physics, 6, 36

[84] Shannon R. M., Cordes J. M., 2010, The Astrophysical Journal, 725, 1607

[85] Shannon R. M. et al., 2013, The Astrophysical Journal, 766, 5

[86] Takata J., Chang H.-K., 2009, Monthly Notices of the Royal Astronomical Society, 392, 400

[87] Thorsett S. E., Arzoumanian Z., Taylor J. H., 1993, ApJ, 412, L33

[88] Tong H., Wang W., Liu X. W., Xu R. X., 2016, ArXiv e-prints

[89] van Dyk S. D., Weiler K. W., Sramek R. A., Rupen M. P., Panagia N., 1994, ApJ, 432, L115

[90] van Straten W., Bailes M., 2010

[91] van Straten W., Manchester R. N., Johnston S., Reynolds J. E., 2010, Publications of the Astronomical Society of Australia, 27, 104

[92] Vranesevic N. et al., 2004, ApJ, 617, L139

[93] Wang N., Manchester R. N., Johnston S., 2007, Monthly Notices of the Royal Astronomical Society, 377, 1383

[94] Wang X.-L., Li Y., Chen J., Guo C.-S., Ding J., Wang H.-T., 2010, Opt. Express, 18, 10786

[95] Wang Y.-M., 1987, Astronomy and Astrophysics, 183, 257

[96] Wang Z., Chakrabarty D., Kaplan D. L., 2006, Nature, 440, 772

[97] Wolszczan A., Frail D. A., 1992, Nature, 355, 145

Mem. S.A.It. Vol. 75, 282

Memorie della

Multi-wavelength analysis of young pulsars: An overview

JM Maritz[1] , PJ Meintjes[1] , SJ Buchner[2]

[1] Physics Department, University of the Free State, 9300, South Africa. e-mail: maritzjm@ufs.ac.za, e-mail: meintpj@gmail.com
[2] HartRAO/SKA, e-mail: sarah@hartrao.ac.za

Abstract. Young pulsars emit a broad spectrum of radiation that range from radio to gamma ray energies. These pulsars are considered as rotation powered pulsars that spin rapidly and are strongly magnetized. Following the discovery of pulsars nearly four decades ago, the population of known pulsars already reached a number of roughly two thousand. This known population of pulsars includes both millisecond and normal pulsars that were discovered by several telescopes. We analyze both HartRAO radio data and Fermi gamma ray data of the Vela pulsar. We also explore a proposed method of probing the electron column density of the instellar gas through analyzing the gamma ray diffuse data associated with the Fermi two-year observation. This paper serves as an overview of gamma ray and radio timing analysis of bright young pulsars with respect to the use of open source timing analysis tools (Tempo2, Psrchive, Enrico and the Fermi tools). We reason that the multi-wavelength picture of pulsars can help clarify questions regarding the origin of pulsed radiation emission mechanisms in several energy bands, but that radio observations will prove adequate for timing noise analysis, given the accurate and long radio data sets. The process of identifying gravitational waves in timing data, rests on gaining a deeper insight into the timing noise phenomena.

Key words. Multi-wavelength timing–Fermi–Gamma ray pulsars–Vela pulsar–Fermi tools–Enrico–Radio Timing

1. Introduction

Pulsars are rapidly spinning and highly magnetized objects that are borne during supernovae explosions. These objects contribute significantly to the fields of astrophysics and nuclear physics due to its peculiar high core density and fast spin-periods that range from milliseconds to several seconds (Lorimer (2005)). These objects produce pulse trains that can be observed in several bands that includes radio and gamma rays (Schlickeiser (2002)) and can be observed and modeled remarkably accurate. This modeling also aids in the search for small gravitational wave signatures in the times of arrival (TOA) of these pulse trains.

The Vela gamma ray data that are available in the LAT Data set, which was released one year after the Fermi launch, can be analyzed using the Fermi Science Tools. These tools will be used for the analysis of pulsed gamma ray data of the Vela pulsar which can be found in the Fermi two-year catalog (see http://fermi.gsfc.nasa.gov/ssc/data/access/lat/2yr_catalog/). We also

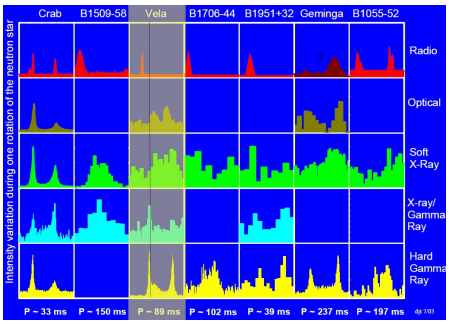

Fig. 1. Multi-wavelength pulses of seven well-known pulsars adapted from Thompson (2004). The pulse-comparison line for the Vela pulsar clearly illustrates the radio lag and the possibility of different emission regions for the observed radiation. This figure represents the true fingerprint of pulsars.

attempt to analyze radio data of the Vela pulsar obtained with the 18cm receiver of the hartRAO 26m radio telescope. The Vela pulsar is radio bright (at Junsky level) (Abdo et al. (2009) (Lorimer, 2005)) and this characteristic simplifies the signal folding procedure (since the signal-to-noise ratio is roughly 1500). These two analyses will produce pulse shapes that are similar to radio and gamma ray pulses highlighted in Fig. 1 (Becker (2009)). However, to understand pulsar emission and characteristics, we need to construct a timing model that is accurate enough to include various contributions to the modeled TOA. These contributions include glitches, giant pulses and timing noise exhibited by both normal and millisecond pulsars (Lorimer (2005)). Timing accuracy of pulsars changes from one energy band to another. Thus, before one can start constraining timing models, one must first be able to perform timing analysis in various energy bands.

2. Modeling the pulse train

Modeling the pulse train (or TOA) of the pulsar as accurately as possible will help (the theorist) to constrain certain fundamental assumptions regarding the pulsar model and the timing model. The barycentric TOA of the pulse could be modelled by including all the effects that cause a delay on the arrival time of the pulse (Lorimer (2005)). This is:

$$TOA = t_{topo} + t_{corr} - \Delta_{DM} + \Delta_{solar\ barycenter} + \Delta_{GW} \quad (1)$$

Where t_{topo}, t_{corr}, Δ_{DM}, $\Delta_{solar\ barycenter}$ and Δ_{GW} represent the time measured on earth, the clock corrections, dispersion measure, barycentric corrections of the solar system and delays in the TOA caused by gravitational wave (GW) stochastic backgrounds produced by merging super massive black holes (Backer and Hellings (1986)). The strain on spacetime induced by GW backgrounds scales as a power law of the frequency of the chosen gravitating source, $h = A_g(\frac{f_g}{yr^{-1}})^{\alpha}$. These backgrounds are very low frequency disturbances in spacetime and are in the nanohertz frequency range (Backer and Hellings (1986)).

Most timing analysis codes include all these effects. Several platforms exist for modeling the GW background influence on the TOA (Hobbs et al. (2006)). Interstellar scattering of the pulse due to cold ionized gas effectively broadens the pulse and increases the error in the TOA prediction. In radio astronomy the measure of dispersion is calculated through the multi-frequency observations of pulsars (knowing the TOA in several bands). The delay caused by pulse dispersion is dependent on the radio band of observation and the dispersion measure.

The density of free electrons between the pulsar and the receiver could also be probed by using the diffuse emission Fermi data. Cosmic rays (or protons) bombard the interstellar gas to produce pions (π^0, π^+ and π^-) that decay into electrons and gamma rays (Schlickeiser (2002)). The amount of integrated free electrons between the pulsar and observer could directly relate to the dispersion measure, this could be cross-correlated with dispersion measure derived from radio timing of the pulsar. The proposed method is as follows: protons (p) bombard the interstellar gas (X) to produce a cascade of particles, this is: $p + X \rightarrow He^3, H^2, p, \pi^0, \pi^+, \pi^-$. Knowing the gamma ray flux that arises from galactic diffuse emis-

sion in the ROI of the source, one could estimate the number of free electrons between the pulsar and the observer. For example, to view the diffuse emission in the data set of the Vela pulsar (whatever the region of interest) the user can create a counts maps of the ROI, see Fig.2 (Abdo et al. (2009)). The total free electron density consists of the electrons contributed by cosmic ray interaction and ionization. This method of probing the dispersion measure through gamma ray diffuse emission maps could be useful for the process of blind pulsar searches in radio/gamma rays. These searches could be simplified if the dispersion measure is known, since the process of coherent dispersion is computationally intensive (Lorimer (2005)).

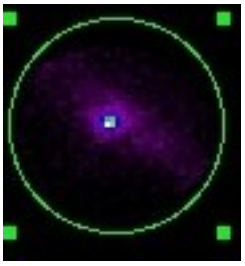

Fig. 2. Counts map of the ROI associated with the Vela pulsar.

3. Gamma ray timing of the Vela Pulsar

Detailed installation instructions for both the Science Tools and Enrico can be found at `http://enrico.readthedocs.org` and `http://fermi.gsfc.nasa.gov/ssc/data/analysis/software/`. There are several methods to install these software packages, but the recommended method involves the installation of the Fermi tools through downloading the source code. Installing Enrico is the simplest part since the user only needs to retrieve the binary distribution from the website (a binary distribution of a software package is a folder that contains the pre-compiled software). To manipulate any `.fits` file one also needs to install HEASOFT from the Fermi site (see `http://heasarc.nasa.gov/lheasoft/`). This software package allows the user to access fits files, view or plot certain columns and concatenate several photon data files, which is possible since the fits files retrieved from the Fermi data server are decomposed into smaller fits files. There are also a number of tutorials on the Fermi site, which include several pulsar gating and likelihood analysis tutorials, see `http://fermi.gsfc.nasa.gov/ssc/data/analysis/scitools/pulsar_gating_tutorial.html` and `http:///data/analysis/scitools/likelihood_tutorial.html` for detailed tutorials and tool commands. Both these tutorials include the process of data retrieval and extraction from the Fermi data server.

For the Fermi analysis of the Vela Pulsar (Abdo et al. (2009)) we used a photon data set from dates MET=239557417 to MET=240105600 between the energy range 300 MeV to 300000 MeV. After the data set had been retrieved from the server, the user will have to perform a selection of photon energies to use in the data set. These steps form part of the pre-processing of data and allow the users to select a subgroup of photon energies that correspond to their source of interest. Assuming that the photon data set is called `Vela_PH00.fits` and that the space craft file is called `Vela_SC00.fits`, one could use the commands:

```
> gselect evclass=2 (this makes a
sub selection)

Input FT1 file[] Vela_PH00.fits
Output FT1 file[] Vela.fits
RA  (degrees) (0:360) [] INDEF
Dec  (degrees) (-90:90) [] INDEF
radius (degrees) (0:180) [] INDEF
start time (MET in s) (0:) [] INDEF
end time (MET in s) (0:) [] INDEF
lower energy (MeV) (0:) [] 100
upper energy (MeV) (0:) [] 300000
maximum zenith angle value
(degrees) (0:180) [] 100
Done.
```

If by this stage the user encounters any problems with the Fermi tools, the following command command can be invoked:

```
> fhelp <fermi tool>
```

The user can also download the emphemeris of the Vela pulsar from `http://fermi.gsfc.nasa.gov/ssc/data/access/lat/ephems/`. This file can be used to assign phases to each photon in the data set. This could be done by using the Fermi-plugin in the Tempo2 code (Ray et al. (2011)).

```
tempo2 -gr fermi
-f Vela.par
-ft1 Vela_PH00.fits
-ft2 Vela_SC00.fits
- options
```

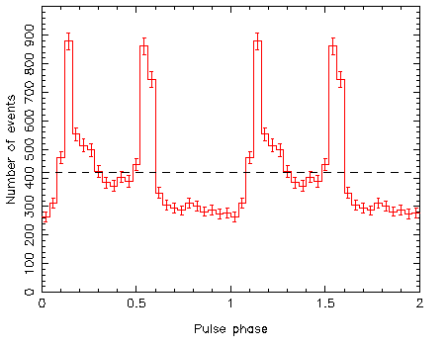

Fig. 3. Folded light curve of the Vela pulsar, clearly showing two peaks (F_1 and F_2) , an off-pulse phase (between F_1 and F_2) and a bridge emission phase after F_2 (Hobbs et al. (2006) Ray et al. (2011)).

The process of classifying the object as a pulsar is simplified if the user knows the ephemeris of the pulsar. If it is not known, then the process becomes more involved. Likelihood analysis can be done via binned or unbinned analysis (the unbinned analysis is the preferred analysis method of Fermi data if one uses large data sets). The user could use an encapsulated Python package (called Enrico) that contains all the steps mentioned above in a somewhat an automated package. This software package is optimized and produces admirable publishable figures (see Fig.4 and Fig.5). The user can consult the site `http://enrico.readthedocs.org` for more information and installation guides. Within the same working folder (that contains all the data files, spacecraft files and diffuse models) the user can initialize the Enrico package by following a few simple commands from Sanchez and Deil (2013); first create a `config`-file that contains all the time-cut and energy range information:

```
>enrico_config Vela.conf
```

The user must answer some simple questions regarding the data files and energy ranges for the pulsar photon data that was downloaded by hand (these data files are located in the user's working folder). The package reads the two-year Fermi catalog and automatically creates a `.xml` file for the chosen point sources in the ROI:

```
>enrico_xml Vela.conf
```

The user can then use Enrico to produce a SED for Vela by using the command:

```
>enrico_sed Vela.conf
```

4. Radio timing of the Vela pulsar

Radio data of the Vela pulsar was analyzed using Psrchive (Hotan et al. (2004)). This software allows the user to produce a standard pulse that can be used to calculate times of arrival (TOA). The software also performs de-dispersion of the pulses by using the fact that each pulse is observed in several frequency bands in the line of sight of the pulsar (Lorimer (2005)). Psrchive links with a pulsar catalog and uses the known parameters to perform the analysis. The time delay between two frequencies due to dispersion (f_1 and f_2) is Δt =

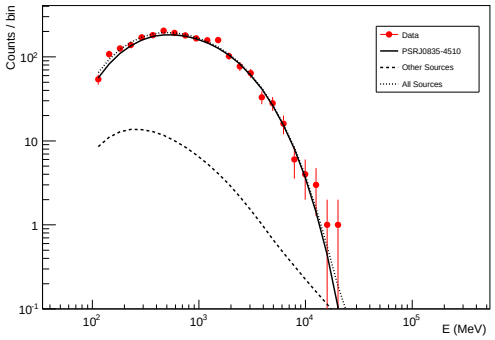

Fig. 4. Fitted SED of the Vela Pulsar fitted with a clear power law with exponential cut-off, $\frac{dN}{dE} = KE^{\alpha}\exp(-(\frac{E}{E_c})^{\beta})$ Becker (2009).

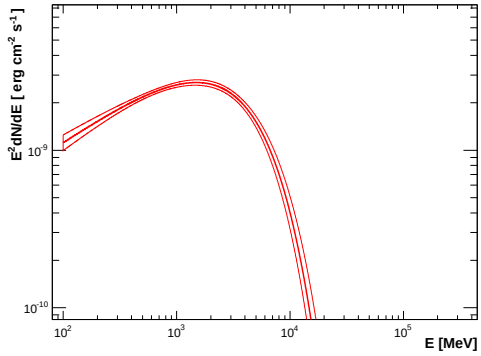

Fig. 5. Just the fitted SED of the Vela Pulsar fitted with a clear power law with exponential cut-off. Also included in the figure is the error band illustrating the goodness of fit. The cut-off for the fit is in the range of 1-10GeV (Backer and Hellings (1986)).

$4.15\times10^{6}\text{ms}\times(f_1^{-1}-f_2^{-1})\times DM$, here DM represents the dispersion measure which is equal to $DM = \int_o^d n_e dl$, with d the distance to the pulsar. The data that was analyzed contained 1024 channels and was centered around the 1700 MHz band. To sample the data we used the `psrplot` command, which produces a figure that shows the pulses in each observational band. The effect of dispersion can also be seen (see Fig. 6). From here all the data files can be filtered (remove all the bad channels), summed (to produce a single pulse per observational file) and de-dispersed using the `pazi`, `pam` and `pas` commands, respectively. At this stage the observational data files are considered cleaned, de-dispersed and considerably smaller in size.

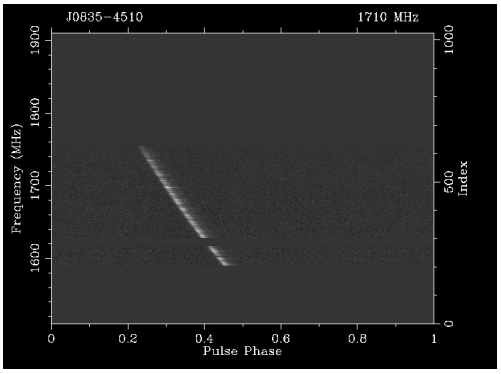

Fig. 6. Frequency cleaned observation data run.

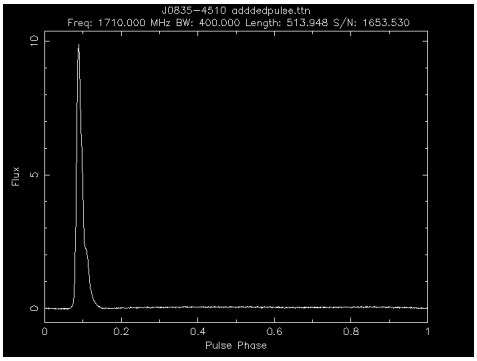

Fig. 7. Standard Vela pulse. This particular pulse was produced by using the observation with the highest SNR and summing the frequency bands to produce one standard pulse that will be used in the calculation of the arrival times of pulses.

The last stage of the analysis involves the production of a standard pulse that can be used

to create a timing file. But first, some statistics (specifically signal-to-noise levels) need to be retrieved for each observation. This is done with the command `psrstats` and the user can now select a pulse that has the highest SNR. This pulse could be used as a standard pulse, but still needs some smoothing and base lining (see Fig. 7). At this stage a file containing the TOA for all the pulses for the observation can be created using `pat`. Lastly the TOA can be modeled using standard `tempo2` software to calculate the residuals of the observed TOA against the modeled TOA (see Fig. 8). Tempo2 models the TOA according to an accurate timing model contained in the software.

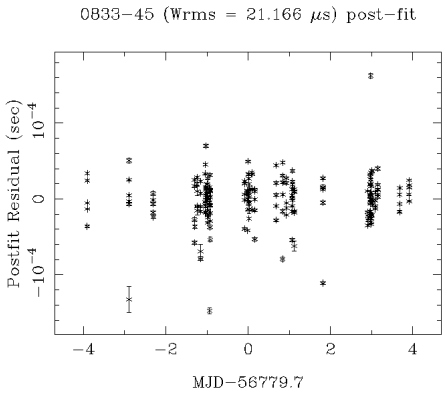

Fig. 8. TOAs residuals as calculated by the Tempo2 code (Hobbs et al. (2006)).

5. Conclusions

Multi-wavelength analysis of pulsars can help to probe the origin of radio, gamma ray and X-ray pulsed emission that are associated with young and old recycled pulsars. However, accurate and lengthy radio observations of pulsars remains the preferred method if one wishes to constrain the search of gravitational wave stochastic signatures in pulsar timings. This is due to error in the TOA (Lorimer (2005)) that scales linearly with the width of the pulse ($\sigma_{TOA} \propto W$).

Timing noise is a leading effect in pulsar timing analysis that threatens the detection of stochastic gravitational wave signatures. This effect can be seen as irregularities in the residuals of the pulsar over a time period of several years and could be linked to effects in the magnetosphere (Lyne et al. (2010)). This work forms part of a campaign for the analysis of timing noise in pulsars frequently observed with the Hartebeesthoek radio telescope over long (decades) time spans.

Acknowledgements. I am grateful the NRF (SKA) program for supporting this work.

References

D. R. Lorimer, *Handbook of pulsar astronomy* (Cambridge University Press, Cambridge, UK New York, 2005), ISBN 978-0-521-82823-9.

R. Schlickeiser, *Cosmic ray astrophysics* (Springer, Berlin London, 2002), ISBN 978-3-540-66465-9.

D. J. Thompson, **304**, 149 (2004), astro-ph/0312272.

A. A. Abdo, M. Ackermann, W. B. Atwood, R. Bagagli, L. Baldini, J. Ballet, D. L. Band, G. Barbiellini, M. G. Baring, J. Bartelt, et al., ApJ **696**, 1084 (2009), 0812.2960.

W. Becker, *Neutron stars and pulsars* (Springer, Berlin, 2009), ISBN 978-3-540-76964-4.

D. C. Backer and R. W. Hellings, ARA&A **24**, 537 (1986).

G. Hobbs, R. Edwards, and R. Manchester, Chinese Journal of Astronomy and Astrophysics Supplement **6**, 020000 (2006).

P. S. Ray, M. Kerr, D. Parent, A. A. Abdo, L. Guillemot, S. M. Ransom, N. Rea, M. T. Wolff, A. Makeev, M. S. E. Roberts, et al., ApJS **194**, 17 (2011), 1011.2468.

D. A. Sanchez and C. Deil, ArXiv e-prints (2013), 1307.4534.

A. W. Hotan, W. van Straten, and R. N. Manchester, **21**, 302 (2004), astro-ph/0404549.

A. Lyne, G. Hobbs, M. Kramer, I. Stairs, and B. Stappers, Science **329**, 408 (2010), 1006.5184.

PROCEEDINGS OF SCIENCE

Constraining GW signatures in pulsar timing: A multi-frequency timing analysis

Jacques Maritz[*†]
Physics Department, University of the Free State, 9300, South Africa
E-mail: maritzjm@ufs.ac.za

Pieter Meintjes
Physics Department, University of the Free State, 9300, South Africa
E-mail: meintpj@gmail.com

Sarah Buchner
SKA, The Park, Park Road, Pinelands, 7405, South Africa
E-mail: sbuchner@ska.ac.za

Pulsars are extremely accurate clocks that allow us to explore certain unanswered questions in the fields of nuclear and gravitational wave astrophysics. Pulsars that form part of a timing array can be used to detect stochastic gravitational wave (GW) backgrounds produced by merging super-massive black holes. However, these backgrounds produce a small amplitude variation in the timing residuals of a pulsar over decades. A number of elements influence the accuracy of the observed times of arrival (TOA); of which "timing noise" contributes to the noise budget due to elements of the pulsar model that we do not understand, as well as the dispersive nature of the ISM through which the pulse propagates. We analyze two decades of data of the pulsar PSR J1326-5859 to observe possible magnetospheric switches that influence the pulsar spin-down which could lead to a deeper understanding of the timing noise phenomena. Here we present the necessary analysis pipeline to investigate the long term stability of the pulsar timing noise, which may lead us to a better understanding of all the contributing factors influencing timing noise. This may then allow possible identification of GW signatures in the pulsar timing noise data.

Frontier Research in Astrophysics,
26-31 May 2014
Mondello (Palermo), Italy

[*]Speaker.
[†]The speaker wishes to acknowledge the SKA for financial support.

PoS(FRAPWS2014)005

1. Introduction

Pulsars are rapidly rotating, highly magnetized objects that are the remnants from supernovae explosions. These objects contribute greatly to the fields of astrophysics and nuclear physics due to its peculiar high core density and fast spin-periods that range from milliseconds to several seconds (e.g. [1]). However, not all pulsars are considered stable clocks. Pulsar timing represents the technique of comparing the observed and computed pulse times of arrival (TOA), this comparison produces a residual that is non-zero and is more commonly known as timing noise. Timing noise varies as a quasi-periodic signature over times-scales of decades.

Together with GW background timing perturbations, these form part of the pulsar red noise reservoir. GW stochastic backgrounds perturb the spacing between the emitted pulses on a scale of $\Delta L/L \approx 10^{-14}$. The timing residual signature of a GW background scales as a power law of the GW frequency, this is $h \approx A_g(\frac{f_g}{yr^{-1}})^{\alpha}$, with A_g, f_g and α being the amplitude of GW background, the frequency of the GW background (in units of years^{-1}) and the spectral index. The size of the residuals induced by GW and timing noise are in the order of microseconds and possibly seconds, respectively. The effect can be simulated on a set of pulsars (with known ephemerides) using the Tempo2 code ([2]).

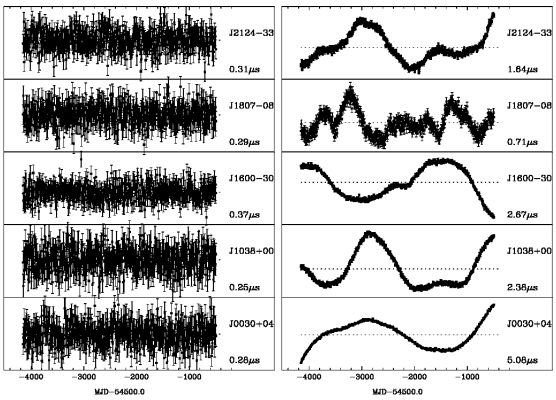

Figure 1: The effect on pulsar timing residuals of GW produced by merging SMBHs(e.g. [1] and [3]).

Detection and characterization of this subtle residual signature depends on deeper insights into other elements that influence the TOA precision. [4] showed the existence of switched magnetospheric regulation of pulsar spin-down. This effect can be seen as a variation between several states in the spin-down ($\dot{\nu}$) and pulse profiles of the pulsar, with time. We propose a similar analysis pipeline on the HartRAO (Hartebeeshoek Radio Astronomical Observatory) observed pulsar PSR J1326-5859, which is a 478 ms pulsar with an effective pulse width of 90 ms. These changes in the pulsar magnetosphere could possibly be linked with timing noise and other pulsar emission phenomena, including pulse-nulling and pulse variations ([4]). Understanding and correcting for timing noise effects in pulsar timing will help us reach the necessary μs-timing accuracy needed for GWs detection. In this paper we present the methodology of the timing noise analysis pipeline by analyzing only a part of the timing data associated with PSR J1326-5859.

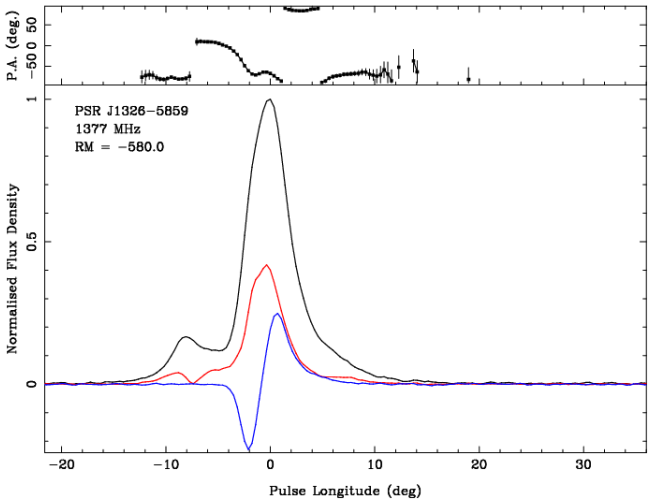

Figure 2: Standard Pulse profile of PSR J1326-5859, from www.atnf.csiro.au ([5]). This includes the Stokes profiles that can also be used in the timing analysis.

2. Timing pulsars

When timing pulsars, the element of interest is the times of arrival (TOA). Pulsars experience a spin-down due to the loss of energy through electromagnetic radiation processes and relativistic particle winds. We describe the pulsar rotation in a reference frame that is co-moving with the pulsar. The barycentric TOA of the pulse can be modeled by including all the effects that cause a delay in the arrival time of the pulse (e.g. [1]). This is

$$TOA = t_{topo} + t_{corr} - \Delta_{DM} + \Delta_{solar\ barycenter} + \Delta_{GW} + \Delta_{timing\ noise}. \tag{2.1}$$

The difference between the modeled and observed TOAs produces non-zero timing residuals that contain signatures that are intrinsic to the pulsar model or the observational instrument. This process is done through a least-squares fit of the pulsar model to the observed TOA. These signatures include: neglected astrometric elements of the pulsar model, glitches, giant pulses and timing noise (e.g. [1]).

There are many factors that determine the timing precision of a pulsar. Using a first approximation, the general timing precision will be $\sigma_{TOA} \propto W/(S/N)$. Here W and S/N represent the pulse width and the signal to noise ratio of the observed pulse.

The signal to noise ratio is

$$S/N = \frac{T_A\sqrt{B\tau}}{T_{sys}}. \tag{2.2}$$

It is evident from the radiometer equation that a longer integration time (τ), large observational bandwidth (B) and minimal system temperature (which could be at least a few tens of Kelvins) will produce the needed signal to noise ratio. Here T_A is the brightness temperature of the source, with $T_{sys} = T_{sky} + T_{receiver}$. Thus millisecond pulsars, in principle, will be the best candidates for timing

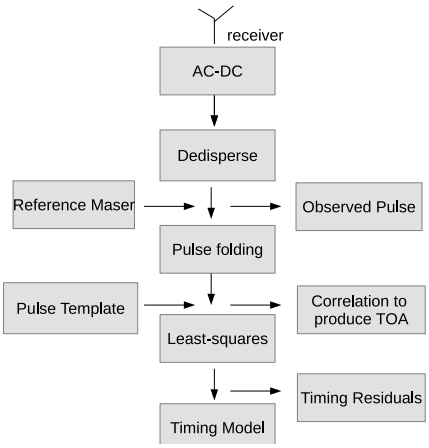

Figure 3: Timing scheme of pulsar observations. The observed signal passes through a filter bank where it is dedispersed and folded (e.g. [1])

precision due to their stable profiles and narrow pulse widths. Timing noise is therefore a fundamental problem, the solution of which will lead to more accurate timing models and techniques to detect stochastic gravitational wave backgrounds.

3. Timing noise: Analysis Pipeline

Recent papers propose methods for correlating timing noise with certain changes in pulsar spin-parameters ([4]). We use this method on PSR J1326-5859 that was observed by the 26m HartRAO radio telescope for several decades with a weekly cadence at 1668 MHz. We analyzed only a part of the data, since further detailed analysis are planned for a future paper.

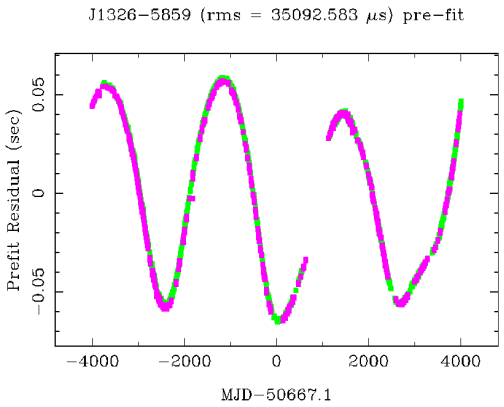

Figure 4: Timing residuals for PSR J1326-5859 produced with the Tempo2 code. The gaps in the data represent time periods when observations ceased ([2]). The non-zero signature in the timing residual represents timing noise.

The spin-down evolution was calculated by dividing the total MJD-span into 300-day sections (δt). We used the Tempo2 glitch-plugin ([2]) to analyze each section and calculate the spin-down evolution ($\dot{\nu}$) with time. In this paper we present only part of the analysis, that is for MJD=48000 to MJD=51000. PSR J1326-5859 has a frequency of 2.092 Hz with a mean spin-down rate of -1.4×10^{-14} Hz/s and a fractional change in the spin-down rate of $\approx 2.5\%$. This switched magnetospheric regulation in the spin-down of PSR J1326-5859 was also observed by [6].

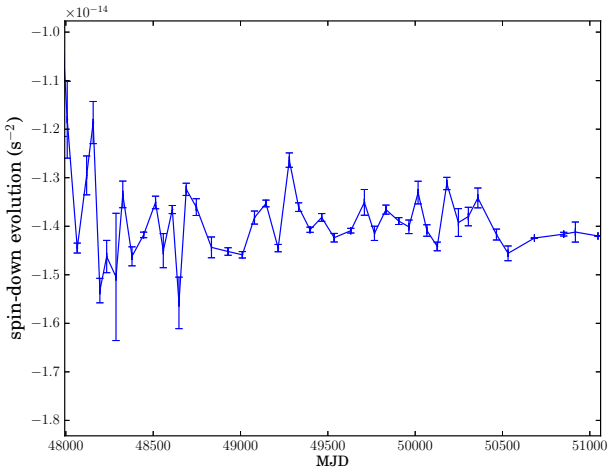

Figure 5: Analysis of the spin parameter $\dot{\nu}$ for a section of the 21 year data set of PSR J1326-5859.

The last part of the timing noise analysis pipeline addresses the Stokes decomposition of the observed single pulses. Unfortunately we did not manage to record the polarization data, since the pulsar timer associated with the 26m HartRAO radio telescope is currently in a testing phase. The vector sum of the electromagnetic waves from the radiating source at the antenna of the telescope has a net polarization that is generally stated in terms of the Stokes parameter I, Q, U and V. These parameters are related, that is $I^2 = Q^2 + V^2 + U^2$. These parameters are generated in the hardware with the use of a polarimeter. The aim of this analysis is to search for changes in the Stokes parameters over the length of the data set. A purely linearly polarized wave has $V = 0$, while $V/Q = 1$ for right-circular polarized and $V/Q = -1$ for left-circular polarized. The relation $\tan(2\Phi) = U/Q$ defines the shape of an ellipse. In addition we will also calculate the ratios V/I and Q/I to search for any changes in the linear or circular polarization of the observed radiation. This part of the analysis will hopefully produce correlations between the Stokes profiles and magnetospheric switches, as well as providing a diagnostic tool to identify temporal GW signatures.

If each part of the pipeline is fully developed and tested, we will eventually analyze all the HartRAO observed pulsars. This will produce a large data set that will be used to cross-correlate timing noise between the HartRAO pulsars and also relate the observed timing noise with any changes in spin-down parameters and the pulse profiles of the pulsars. We are planning to enable the HartRAO pulsar timer to start recording polarization data for future pulsar observations.

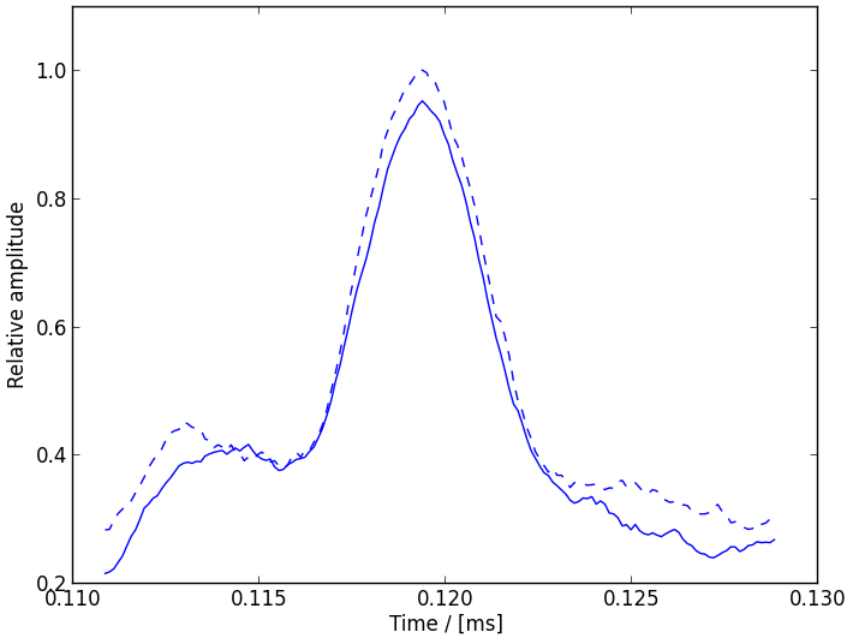

Figure 6: Standard pulses for two observational regions: at MJD = 47750 (line) and MJD = 49000 (dashed line). The standard pulse profiles correspond to the standard archival profiles.

4. Discussion and conclusions

[6] performed similar timing noise statistical analysis on 27 HartRAO pulsars. The observed fluctuations between states in the spin-down evolution are seen in both Parkes ([4]) and HartRAO pulsar long term data and could be linked with pulse shape variations. Evidently, the pulse profiles at the two extreme spin-down states are different.

The observed structures in the timing residuals of PSR J1326-5859 arise from the spin-down rate switching systematically between states. The two distinct spin-down states correspond with the most extreme pulse shapes observed at the two states (this was for MJD = 48000 to MJD = 51000). This could possibly be a relationship between the spin-down evolution and magnetospheric switches.

The accuracy and sensitivity of modern day radio telescopes are being improved at an dramatic rate, however magnetospheric state switching is responsible for limiting the accuracy of the timing accuracy. The aim is to model and remove the timing noise and improve the prospects of producing an essentially stable clock. The future of timing noise analysis will depend on high resolution single pulse data observed with low-noise, sensitive radio telescopes.

References

[1] D. R. Lorimer. *Handbook of pulsar astronomy*. Cambridge University Press, Cambridge, UK New York, 2005. ISBN 978-0-521-82823-9.

[2] G. Hobbs, R. Edwards, and R. Manchester. *TEMPO2: a New Pulsar Timing Package*. *CJAA*, 6(2):020000–192, December 2006.

[3] G. Hobbs, F. Jenet, K. J. Lee, J. P. W. Verbiest, D. Yardley, R. Manchester, A. Lommen, W. Coles, R. Edwards, and C. Shettigara. *TEMPO2: a new pulsar timing package - III. Gravitational wave simulation*. *MNRAS*, 394:1945–1955, April 2009.

[4] A. Lyne, G. Hobbs, M. Kramer, I. Stairs, and B. Stappers. *Switched Magnetospheric Regulation of Pulsar Spin-Down*. *Science*, 329:408–, July 2010.

[5] R. N. Manchester, G. B. Hobbs, A. Teoh, and M. Hobbs. *VizieR Online Data Catalog: ATNF Pulsar Catalog*. *VizieR Online Data Catalog*, 7245:0, August 2005.

[6] A. E. Chukwude. *A Statistical Analysis of Radio Pulsar Timing Noise*. *CJAA*, 7:521–530, August 2007.

PROCEEDINGS OF SCIENCE

Timing Noise analysis of HartRAO pulsars: Possible mode switching in the magnetosphere of PSR J1326-5859

Jacques Maritz[*†]
Physics Department, University of the Free State, 9300, South Africa
E-mail: maritzjm@ufs.ac.za

Pieter Meintjes
Physics Department, University of the Free State, 9300, South Africa
E-mail: meintpj@gmail.com

Sarah Buchner
SKA, The Park, Park Road, Pinelands, 7405, South Africa
E-mail: sbuchner@ska.ac.za

Natalia Lewandowska
Hartebeesthoek Radio Astronomy Observatory,P.O.Box 443, Krugersdorp 1740, South Africa
E-mail: nlewm45@gmail.com

Timing noise in long-term pulsar timing residuals is challenging our understanding of the present pulsar model and forms part of several key science projects, including the detection of GWs and the development of next-generation instruments for pulsar astronomy. We investigate the timing noise phenomena in PSR J1326-5859 that was observed with the 26m HartRAO radio telescope for several decades. One explanation for timing noise is mode switching in the magnetosphere of the pulsar. In this paper we investigate the possible mode switching seen in the spin-down evolution and the pulse shape parameters of PSR J1326-5859. We also search for possible correlations between the parameter data sets.

3rd Annual Conference on High Energy Astrophysics in Southern Africa ,
18-20 June 2015
University of Johannesburg, Auckland Park, South Africa

[*]Speaker.
[†]The speaker wishes to acknowledge the SKA for financial support.

1. Introduction

Pulsars are considered to be stable cosmic clocks [1], however long-term and single pulse observations reveal that our theoretical picture of pulsars is incomplete. Pulsar timing is becoming ever more complex and accurate with modern receivers, backends and processing algorithms. The phenomena of timing noise as seen in some of the long-term pulsar timing residuals are challenging the current pulsar models and some novel ideas are being put forward to challenge the concept of timing noise [2, 3, 4], these include: linking timing noise to activities in the magnetosphere of the pulsar and ultimately to fundamental processes such as precession and the pulsar emission mechanisms. Resolving timing noise as a limiting noise factor can ultimately influence the accuracy of pulsar timings arrays [5]. The process of modeling timing noise can help us to improve the current pulsar model.

Recent observations [6] suggest some pulsars that show quasi-periodical timing noise structures in timing residuals display the phenomena of sharp changes in their spin-down that could also be accompanied by changes in the pulse profiles. It has been pointed out in [3] that some of the pulsars reported in [6] show systematic and recurring switching (e.g. PSRs B1540-06, B1642-03, B1826-17 and B1828-11) and that it could be linked to other dynamical phenomena such as precession and glitching.

In this paper we investigate the possible mode switching seen in long-term timing residuals of PSR J1326-5859 and we try to link the observations to possible models.

2. Calculating the spin-down evolution of PSR J1326-5859

To calculate the spin-down evolution ($\dot{\nu}$) of PSR J1326-5859, we reconstructed the timing noise signature using a Gaussian process made available in the form of the Gaussian Process in Python (GaPP) code [7], similar work was done and initialized by [4]. This type of fitting procedure ensures that the second derivative of the reconstructed signature is calculated in a natural way without the dependence of assumptions such as step length, see Fig. 1. A list of residuals and times of arrival (TOA) errors was produced for the total data set using the TEMPO2 code [8]. These residuals and TOA errors serve as input for the GaPP code. It must be noted that the reconstructed Gaussian signature retains the attribute of being n-times differentiable.

One important part of the Gaussian process is the optimization of the step length (l). The parameters for the Gaussian process were optimized to be $l = 232$ days and $Var(x) = 2.8 \times 10^{-2}$. The calculation of these parameters were done by keeping in mind the TOA errors associated with the data. The errors associated with the data influence the optimization process of the step length in the kernel:

$$k(x,x') = \sigma^2 \exp\left(-\frac{(x-x')^2}{2\ell^2}\right). \tag{2.1}$$

Here (x,x'), σ^2 and l represent two neighboring points, the variance and the step length of the Gaussian kernel.

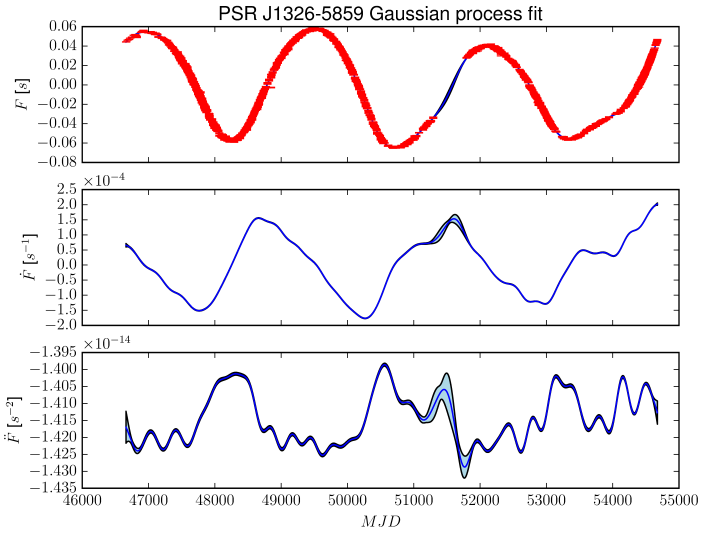

Figure 1: Timing residuals of PSR J1326-5859 showing a timing noise signature that is quasi-periodic, together with the first and second derivatives. The break in the residuals (MJD 51300-51700) was due to telescope maintenance. The light tinted band represents the error band. The scaling of $\dot{\nu}$ arises through the process of partial derivatives with time, see [4].

3. Interpreting the spin-down evolution of PSR J1326-5859

The timing noise signature seen in PSR J1326-5859 is unlike the near perfect periodical timing residuals that are predicted by models of precession or binary companions. However, it remains a premature assumption that precession [3] does not participate in the observed mode switching of pulsars [6].

The second derivative of the Gaussian reconstructed quasi-periodical timing residuals leads to abrupt mode switching that can be seen in the spin-down evolution of PSR J1326-5859, see Fig.1. There exists a clear change in the spin-down evolution after MJD $= 51000$. To better understand the variations seen in the spin-down evolution ($\ddot{\nu}$) of PSR J1326-5859, we performed a Ricker wavelet (Mexican hat wavelet) analysis on the data, see Fig.2. Using the wavelet spectra, we see a dominant variation present in most of the data set that is seen as the red, yellow and light blue contours. Wavelet analysis decomposes a time series (the data) into time/frequency space simultaneously. One gets information on both the amplitude of any periodic signals within the data, and how this amplitude varies with time. The wavelet analysis algorithm will typically produce contours that span the whole data set if any periodical variations are hidden in the data set.

Mode switching in the magnetosphere of the pulsar can also be linked to changes in the average pulse profile due to changes in the emission mechanisms (see PSRs J2043+2740, B2035+36, B1828-11, B0740-28, B1540-06 and B1822-09 in [6]). Unfortunately, no high resolution temporal stacking of the pulses could be achieved due to the low signal to noise ratio of the integrated pulses (PSR J1326-5859 is a 10 mJy source). To achieve the desired temporal stacking resolution, we will need average pulse profiles from more sensitive radio telescopes. Furthermore, extra timing

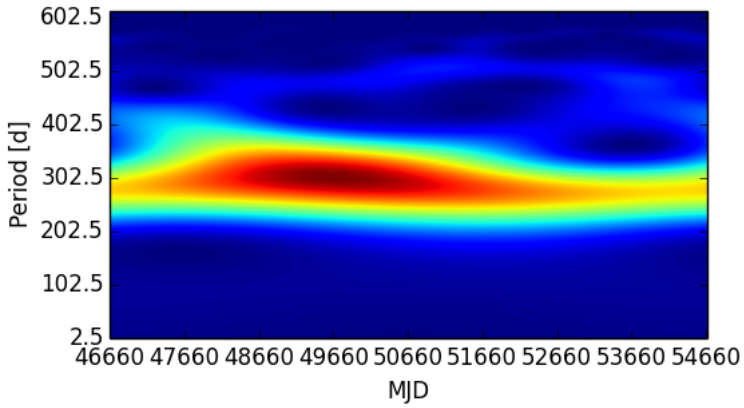

Figure 2: Ricker wavelet analysis of the spin-down evolution of PSR J1326-5859. Pure periodic variations in the data cannot be assumed and therefore wavelet analysis can be considered to be a better period finding method than Lomb-Scargle analysis (in this case, see [6] for more detail).

residuals and high signal-to-noise ratio (SNR) pulses (with polarization profiles) will enable the search for correlations between the magnetospheric activity and any changes in the pulse profiles.

At this point we can introduce some novel models that were suggested recently [3] as a possible explanation for the mode switching seen in a number of millisecond pulsars [6]. These models are based on two fundamental attributes of the pulsar itself: firstly, there exists some deformation of the star (this is beneficial to both models of precession and gravitational wave detection) and secondly, the observed mode switching retains memory of the previous state. Both the latter arguments support some underlying precession driven mechanism acting as a clock that smoothly and repetitively induces a wobble angle that could change the conditions of the magnetosphere, hence the precession and mode switching of the pulsar could be phase-locked.

4. Conclusions and future work

It is suggested that the timing noise observed in millisecond pulsars can be modeled as mode switching in the magnetosphere of the pulsar [6]. Furthermore, the observed mode switching could also possibly be linked to the processes of precession and glitching [3].

It will be an intensive observational campaign to link pulsar moding with precession, but it will be beneficial to understand timing noise and to improve the sensitivity of the pulsar timing arrays. It also remains a premature statement that the model for timing noise consists of only mode switching, since we know that there could be several other factors that influence the spin-down or emission mechanisms of the pulsar. Timing noise signatures are normally seen in some pulsars with data spanning several decades. The population of glitchers and pulsars that exhibit timing noise, is interwoven (see Fig.3).

A possible way forward for timing noise analysis could be to construct models that include both the appropriate mode switching and some degree of precession (this was done to some extent in [6]). The precession component of the model does not need to be detectable in amplitude but

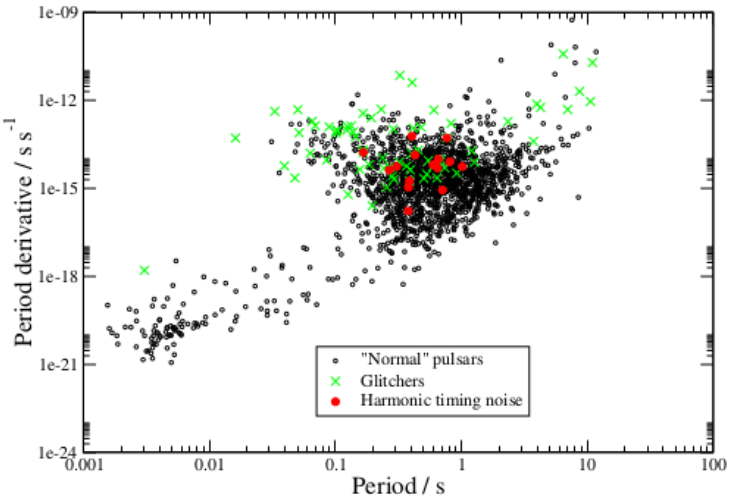

Figure 3: *P-$\dot{P}$* diagram for the pulsar population. The diagram also contains pulsars that show glitch and timing noise activity. Adopted from [3].

could just switch the magnetosphere from one state to the other [3] (assuming that the magnetosphere is delicately balanced between two magnetospheric states). From the observational point of view, if timing noise is seen in pulsar timing residuals then a long baseline data set exists. To compliment this extended data set we suggest high quality Stokes profiles for different temporal regions that can be used to track polarization changes throughout the different observed modes. Tracking the correctly calibrated polarization swing of Stokes profiles across different temporal regions of the spin-down evolution of the pulsar could allow for a better campaign to correlate events in the spin-down and magnetosphere of the pulsars.

References

[1] A. Hewish, S. J. Bell, J. D. H. Pilkington, P. F. Scott, and R. A. Collins, *Observation of a rapidly pulsating radio source*, *Nature* **217** (1968) 709–713.

[2] D. I. Jones and N. Andersson, *Freely precessing neutron stars: model and observations*, *MNRAS* **324** (2001) 811–824, [astro-ph/0011063].

[3] D. I. Jones, *Pulsar state switching, timing noise and free precession*, *MNRAS* **420** (2012) 2325–2338, [arXiv:1107.3503].

[4] P. R. Brook, A. Karastergiou, S. Johnston, M. Kerr, R. M. Shannon, and S. J. Roberts, *Emission-rotation correlation in pulsars: new discoveries with optimal techniques*, *ArXiv e-prints* (Nov., 2015) [arXiv:1511.0548].

[5] S. Osłowski, W. van Straten, G. B. Hobbs, M. Bailes, and P. Demorest, *High signal-to-noise ratio observations and the ultimate limits of precision pulsar timing*, *MNRAS* **418** (2011) 1258–1271, [arXiv:1108.0812].

[6] A. Lyne, G. Hobbs, M. Kramer, I. Stairs, and B. Stappers, *Switched magnetospheric regulation of pulsar spin-down*, *Science* **329** (2010) 408–412, [arXiv:1006.5184].

[7] M. Seikel, C. Clarkson, and M. Smith, *Reconstruction of dark energy and expansion dynamics using gaussian processes*, *JRASC* **6** (2012) 36, [arXiv:1204.2832].

[8] G. Hobbs, R. Edwards, and R. Manchester, *Tempo2: a new pulsar timing package*, *CJAA* **6** (2006), no. 2 189.

A Timing Noise Analysis Pipeline for HartRAO pulsars applied to PSR J1326-5859

Jacques Maritz[1*], Pieter Meintjes[1], Sarah Buchner[2], Natalia Lewandowska[3]

[1]Physics Department, University of the Free State, 9300, South Africa
[2]SKA, The Park, Park Road, Pinelands, South Africa
[3]Hartebeesthoek Radio Astronomy Observatory, P.O.Box 443, Krugersdorp 1740, South Africa

E-mail: *maritzjm@ufs.ac.za

Abstract. Timing noise in long-term pulsar timing residuals is a challenge to our understanding of present pulsar models. The quest to understand on the emission mechanisms of radio pulsars has led to various key science projects ranging from the search for gravitational waves to the development of next-generation instruments for pulsar astronomy. Timing noise studies present an essential cornerstone in these projects. One possible explanation for the existence of timing noise is mode switching in the magnetosphere of the pulsar. In a long-term study we have investigated the timing noise phenomena seen in PSR J1326-5859. It was observed with the 26 m radio telescope of the Hartebeesthoek Radio Astronomical observatory (HartRAO) for several decades and exhibits a large variety of timing noise characteristics. In this paper we review the preliminary timing noise analysis pipeline used for PSR J1326-5859 which can be also used for other southern hemisphere pulsars observed with HartRAO.

1. Introduction

Pulsars can be considered as stable cosmic clocks that serve the purpose of testing fundamental theories and advancing computing technology [1]. Integrated pulses of pulsars can be used for timing purposes. However, careful inspection of the single pulses reveal a rather unstable picture regarding their emission modes [2]. Inspecting the integrated pulses and the timing residuals over a long time span (months to years) allow us to see possible signatures of mode switching [3], nulling [4], glitching [5], precession [6], timing noise [7] and the phenomenon of intermittent pulsars [1]. Anomalous pulse emission modes have unique longitudinal positions that require sophisticated observational hardware [8] and algorithms [9].

Most of these emission modes (or signatures in the residuals of the pulsar) can be linked to changes in the magnetosphere, plasma conditions and/or the pulse profile of the pulsar itself [3]. Theoretically, any changes in the magnetosphere of the pulsar also influence the spin-down ($\dot{\nu}$). Therefore, if the spin-down of the pulsar can be computed accurately over the total time span of the observed data, it will reveal the history of the spin-down and the magnetospheric conditions of the pulsar. One can then fit different models to the spin-down of the pulsar with the hope of linking the conditions of the magnetosphere (emission history) to changes in the pulse profiles. Lyne et al. [3] observed a correlation between the spin-down and pulse profile changes in several pulsars. These correlations are in the form of mode switching in the pulsar

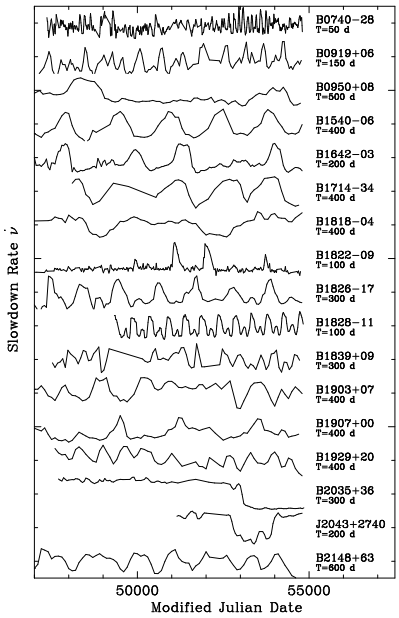

Figure 1. The spin-down history of 17 pulsars adopted from [3]. Clear mode switching between several states can be seen in the spin-down evolution of the pulsars. [3] also linked the mode switching seen in the spin-down evolution of the pulsars to pulse profile changes.

magnetosphere and could be a possible explanation for the observed timing noise signature seen in the timing residuals of several pulsars (Fig. 1).

In this paper we investigate the possible methods to link the observed timing noise signatures with possible changes in the magnetosphere and pulse profiles of the Hartebeeshoek Radio Astronomy Observatory (HartRAO) long term pulsar data sets. Timing noise analysis proves important for gravitational wave (GW) detection through the use of pulsar timing arrays, since both timing noise and GW signatures are considered to be red noise [10]. This paper is structured as follows: HartRAO Pulsar Data (Section 2), General Analysis Method (Section 3), Computing Algorithms (Section 4), Preliminary Results of spin-down Evolution of PSR J1326-5859 (Section 5) and an Discussion (Section 6).

2. HartRAO pulsar data

We investigate the timing noise signature seen in the 21 year long data set of PSR J1326-5859. This is a 478 ms [11] pulsar with a dispersion measure of $DM = 287\,\mathrm{pc\,cm^{-3}}$ [12] and an average spin-down of $-1.415 \times 10^{-14}\ \mathrm{s^{-2}}$ [13]. The data contains both 18cm and 13cm observations that were performed with the 26m HartRAO radio telescope. Timing of PSR J1326-5859 was done with the help of the packages TEMPO2 and PSRCHIVE [10,14]. Each time of arrival (and subsequently every residual) was produced via single polarization observations with an integration time of 20 minutes (Fig. 2).

3. General method of analysis

Timing residuals are produced by comparing the observed times of arrival (TOA) to the predicted ones, this process can be done with a combination of software: DSPSR (folding of raw data) [15], PSRCHIVE (manipulating of folded data) and TEMPO2 (timing analysis). Raw data are folded according to a pulsar ephemeris and the integrated pulse is used as a standard pulse to determine the TOA. A timing model is then fitted to the list of TOA and factors that are not

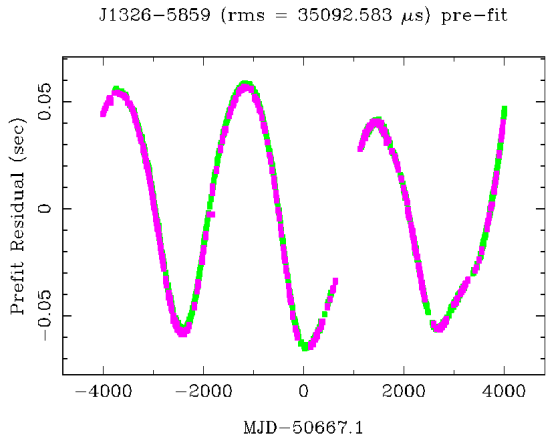

Figure 2. Timing residuals of J1326-5859 showing a timing noise signature that is quasi-periodic. The break in the residuals was due to telescope maintenance. Purple and green points represent observations at 13cm and 18cm.

predicted in the model will produce a unique signature in the residuals. In PSR J1326-5859 the signature is in the form of long time scale quasi-periodic timing noise.

When trying to connect the observed timing noise signature (or residuals) to the spin-down evolution of the pulsar, the immediate complexity that arises is that of computing the second derivative of the signature. This is done by reconstructing a function (F) that fits the residual signature. If the function F is not fitted in an accurate way, then the second derivative ($\ddot{F}$) will resemble false history of the spin-down of the pulsar. Any behaviour that is not considered as normal mode of emission, will be reflected in the spin-down history, like for example: glitches, mode switching, encounters with secondary masses and nulling. In the next section we investigate the possible methods to reconstruct the function F.

[16] developed novel methods and techniques to correlate the short term variability seen in both the pulsar spin-down and pulse profile variations by implementing Gaussian processes. We closely follow their recipe for determining the spin-down evolution using Gaussian process reconstructions of the residuals.

4. Algorithms

There are several methods to compute the spin-down evolution by using the timing residuals of a pulsar. One such method is to use the glitch plugin provided with the TEMPO2 code [10]. This plugin accepts hand-selected regions of residuals and computes the spin-down for each of these regions. However, the second derivative ($\ddot{F}$) is sensitive to the size of the chosen regions. Consequently, this method is restricted by the prerequisites of knowing what type of emission history to look for in the spin-down history (such as mode switching).

Another popular method to reconstruct the function F is the use of Gaussian fits. The main benefit of this fitting process is that the sizes of regions are optimized and the error in the reconstructed function decreases if the residuals are locally predictable. The Gaussian fitting process requires no assumptions of whether F is related to a specific model. The value of F when evaluated at any point x is a Gaussian random variable with mean $\mu(x)$ and variance $Var(x)$. The function values at a point x and some other point x' are related by the covariant function, $k(x, x')$. Thus, the latter indirectly implies that fitting a semi-predictable signature will produce a good fit to the residuals. The GaPP (Gaussian process in python) code [17] is

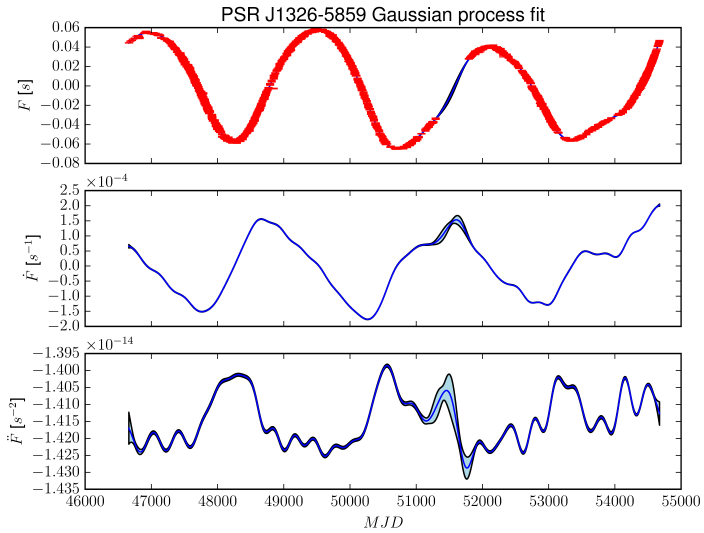

Figure 3. Spin-down evolution of PSR J1326-5859. Upper panel: Fitted timing noise residual. Middle Panel: Spin-down ($\dot{F}$). Lower Panel: Spin-down evolution ($\ddot{F}$). Errors of the fit are indicated by the shaded regions. The scaling of $\ddot{F}$ arises through the process of partial derivatives with time, see [16].

used to perform the Guassian process regression on the residuals. The GaPP is used for the reconstruction of dark energy data.

After computing the spin-down history of the pulsar, one can look at the history to identify certain signatures worth investigating and link that to any pulse profile changes. This can be done by a self developed python code that loads, fits and cleans the integrated pulses that were produced for each observation. One can afterwards plot, manipulate or stack pulses in certain regions of time. The only limitation of this process is the quality of the pulse profile itself.

5. Preliminary spin-down evolution of PSR J1326-5859

A list of residuals and TOA errors can be produced for the total data set using the TEMPO2 code. These residuals and TOA errors serve as input for the GaPP code. The GaPP code initializes the Gaussian process with initial parameters for the mean and the variance according a kernel:

$$k(x, x') = \sigma_f^2 \exp\left(-\frac{(x - x')^2}{2\ell^2}\right). \tag{1}$$

One important part of the process is the optimization of the step length (l). Lastly follow the training of the hyper-parameters, reconstruction of the function F and its second derivative $\ddot{F}$ (Fig. 3). The parameters for the Gaussian process were optimized to be $l = 232$ days and $\sigma_f = 2.8 \times 10^{-2}$.

We used the pipeline to stack pulses in two temporal regions (48000 − 48500 MJD and 49000 − 49500 MJD) of different spin-down values (Fig. 4). A constant number of pulses were added in both regions to ensure a consistent S/N. In this paper the stacking was done for only the first part of the data set. The investigation of the second half will be left for future work.

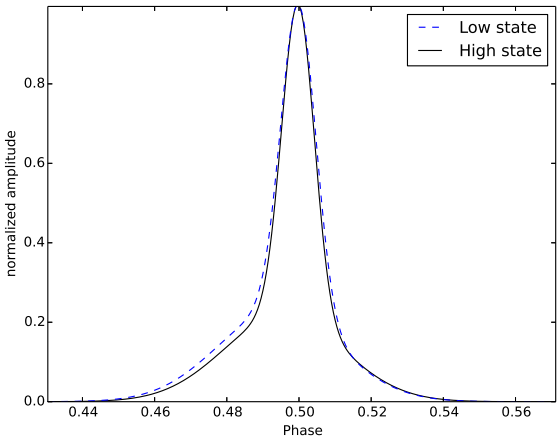

Figure 4. Stacking of 1644 MHz integrated pulses of PSR J1326-5859 in two different regions. The high and low state correspond to the largest and lowest spin-down observed in PSR J1326-5859.

6. Discussion

Switching in the spin-down evolution of PSR J1326-5859 is clearly visible (Fig. 3). The observed switching reveals itself as changing between two extreme states in the first half of the data set and becomes less predictable in second half. The stacking of pulses (of equal stacking length) in different states of the spin-down evolution proves to be insufficient for correlation searches. Thus, correlating the observed spin-down evolution to the pulse profiles, will require more sophisticated techniques that will be done in future work. In addition to the switching, we also observe an increase in the mean of the spin-down from MJD = 53000. Spin-down activity in the second half of the data becomes less clear. Similar results can be seen in the spin-down evolution of several pulsars reported in [3] (see Fig. 1-3 in their paper) and [16]. Recently a numerical model was developed for the evolution of non-spherical pulsar parameters (period and inclination angle) with plasma filled magnetospheres [18]. This MHD model was used to fit the observed residuals of PSR B1828-11 and the Crab pulsar according to a precession model. As future work we will be fitting different models to the spin-down evolution of PSR J1326-5859 (especially the second part of the data set) to test possible signatures such as MHD precession or encounters with massive objects.

7. Acknowledgments

We would like to acknowledge the SKA project for the financial support of this work.

References

[1] Lorimer D R 2005 *Handbook of pulsar astronomy* (Cambridge, UK New York: Cambridge University Press) ISBN 978-0-521-82823-9

[2] Osłowski S, van Straten W, Hobbs G B, Bailes M and Demorest P 2011 *Monthly Notices of the Royal Astronomical Society* **418** 1258–1271 (*Preprint* 1108.0812)

[3] Lyne A, Hobbs G, Kramer M, Stairs I and Stappers B 2010 *Science* **329** 408–412 (*Preprint* 1006.5184)

[4] Backer D C 1970 *Nature* **228** 42–43

[5] Lyne A G, Smith F G and Pritchard R S 1992 *Nature* **359** 706–707

[6] Frescura F and Flanagan C S 2003 *Radio Pulsars* (*Astronomical Society of the Pacific Conference Series* vol 302) ed Bailes M, Nice D J and Thorsett S E p 237

[7] Chukwude A E 2007 *Chinese Journal of Astronomy and Astrophysics* **7** 521–530

[8] Karuppusamy R, Stappers B and van Straten W 2008 *Publications of the Astronomical Society of the Pacific* **120** 191–202

[9] Jones D I 2012 *Monthly Notices of the Royal Astronomical Society* **420** 2325–2338 (*Preprint* `http://mnras.oxfordjournals.org/content/420/3/2325.full.pdf+html`) URL `http://mnras.oxfordjournals.org/content/420/3/2325.abstract`

[10] Hobbs G, Edwards R and Manchester R 2006 *Chinese Journal of Astronomy and Astrophysics Supplement* **6** 020000–192

[11] D'Alessandro F, McCulloch P M, King E A, Hamilton P A and McConnell D 1993 *Monthly Notices of the Royal Astronomical Society* **261** 883–894

[12] Hobbs G, Faulkner A, Stairs I H, Camilo F, Manchester R N, Lyne A G, Kramer M, D'Amico N, Kaspi V M, Possenti A, McLaughlin M A, Lorimer D R, Burgay M, Joshi B C and Crawford F 2004 *Monthly Notices of the Royal Astronomical Society* **352** 1439–1472 (*Preprint* `astro-ph/0405364`)

[13] Manchester R N, Hobbs G B, Teoh A and Hobbs M 2005 *VizieR Online Data Catalog* **7245**

[14] Hotan A W, van Straten W and Manchester R N 2004 *Publications of the Astronomical Society of Australia* **21** 302–309 (*Preprint* `astro-ph/0404549`)

[15] van Straten W and Bailes M 2010 (*Preprint* `1010.006`)

[16] Brook P R, Karastergiou A, Johnston S, Kerr M, Shannon R M and Roberts S J 2016 *Monthly Notices of the Royal Astronomical Society* **456** 1374–1393 (*Preprint* `1511.05481`)

[17] Seikel M, Clarkson C and Smith M 2012 *Journal of Cosmology and Astroparticle Physics* **6** 36 (*Preprint* `1204.2832`)

[18] Arzamasskiy L, Philippov A and Tchekhovskoy A 2015 *ArXiv e-prints,1504.06626*